DESIGN OF THE CHRISP ADAPTIVE OPTICS SYSTEM

By

Gregory Stephen Burley

B. Eng. (Engineering Physics) McMaster University

M. Sc. (Electrical Engineering) Queens University

A THESIS SUBMITTED IN PARTIAL FULFILLMENT OF

THE REQUIREMENTS FOR THE DEGREE OF

DOCTOR OF PHILOSOPHY

in

THE FACULTY OF GRADUATE STUDIES

PHYSICS AND ASTRONOMY

We accept this thesis as conforming

to the required standard

THE UNIVERSITY OF BRITISH COLUMBIA

April 1997

In presenting this thesis in partial fulfilment of the requirements for an advanced degree at the University of British Columbia, I agree that the Library shall make it freely available for reference and study. I further agree that permission for extensive copying of this thesis for scholarly purposes may be granted by the head of my department or by his or her representatives. It is understood that copying or publication of this thesis for financial gain shall not be allowed without my written permission.

Physics and Astronomy

The University of British Columbia

2219 Main Mall

Vancouver, Canada

V6T 1Z4

Date:

30 APRIL 1997

Abstract

Adaptive optics increases the angular resolution of large, ground-based telescopes by compensating for the effects of atmospheric turbulence. CHRISP is a prototype adaptive optics system based on curvature sensing I have designed and built for the DAO 1.2 meter telescope. To simplify the optical design, the CHRISP wavefront sensor detects curvature deviations in a single defocused image. The prototype wavefront sensor uses a low noise frame transfer 64×64 CCD with a custom DSP56002 controller. Low order wavefront correction (including tip-tilt) is provided by a deformable membrane mirror with a few dozen electrostatically driven actuators. The control system maps sensor zones to the corresponding mirror actuators.

Ultimately, I expect to use CHRISP to study faint companions to nearby stars, using the primary as a natural guide star. The details of many binary systems are hidden, since the secondary spectrum is hard to detect against the glare from the primary star. Improving the image sharpness and diverting the primary light should greatly enhance the contrast of the faint companion.

The CHRISP prototype is a testbed for the single image curvature sensing technique, and for the prototype wavefront sensor and membrane mirror.

Table of Contents

List of Tables

List of Figures

Acknowledgements

For her encouragement and support, I am truly grateful to Janet Mumford. Throughout my years at UBC, she was understanding and patient as my time was taken up with dewars, detectors, mirrors, and code.

Special thanks to Gordon Walker and Ron Johnson for generous amounts of guidance and time, and to my collaborators and sponsors at UBC, DAO and ASA.

For making grad school an enjoyable experience and for enriching my days here, I am happy to have crossed paths with Dave^2, Ted, Phil, Brad, Sally, Yiman, Andrew, James, Steve, Remi, Jaymie, Stephenson, Eiji, Rodrigo, Scott, Sandra, Chris, Alex, Georgi, and Nick. Special thanks to Mike and Tasha.

Finally, many thanks to my family who have always encouraged me to follow my interests.

Chapter 1

Introduction

1.1 Introduction and Background.

With adaptive optics (AO), the angular resolution of large telescopes can be improved by compensating for the distortions introduced by atmospheric turbulence. Turbulence, by mixing air masses of different temperature and refractive index, causes variations in the path length of starlight traveling through the atmosphere, resulting in phase variations across the wavefronts arriving at the telescope. At the telescope focal plane, these phase variations result in image motion and distortion that smear out fine detail during long time exposures. Even at the best sites, the angular resolution achieved with a modern ground-based telescope is only in the range of 0.5 to 1.0 arcseconds. Excellent introductions to the subject have appeared in Scientific American [1] and in Annual Reviews of Astronomy and Astrophysics [2].

With an adaptive optics system, wavefront variations are sensed, then corrections are applied (in real time) by a deformable mirror in the optical path. Starlight passes through the atmosphere and into the telescope, where it is reflected from a deformable mirror to the scientific instrument (as shown in Figure 1.1). A fraction of the light is diverted to the wavefront sensor, which analyses it in a number of subapertures, and determines the wavefront errors. A control system provides feedback from the wavefront sensor to the actuators of the deformable mirror as the system seeks to change the shape of the mirror to null out any errors seen by the wavefront sensor. As the atmosphere changes, the deformable mirror tracks out any new variations measured by the wavefront

sensor, which samples the atmosphere several hundred times per second. As an added bonus, some of the static optical errors and wind shake of the telescope are automatically compensated. Adaptive optics systems require a guide star to probe the atmosphere. Since bright stars are not distributed evenly on the sky, systems must work with faint guide stars to ensure good sky coverage.

Originally proposed by Babcock [3] in 1953, rapid progress in adaptive optics has been made in the last decade. Prototype systems based on both lenslet array sensors with piezoelectric-stack actuator mirrors, and on curvature sensors with bimorph mirror technology have been demonstrated. The resolution improvements from these prototype systems have been impressive [4, 5, 6], with "diffraction-limited" results in the infrared achieved by both approaches as the technology matures. Systems with artificial laser guide stars are now being prepared for astronomy.

One general approach to adaptive optics uses a Shack-Hartmann wavefront sensor combined with a piezoelectric stack mirror. The sensor involves a lenslet array placed at an image of the telescope pupil, with a charge-coupled device (CCD) detector in the focal plane of the lenslets. Each lenslet defines a subaperture, and forms an image of the guide star on the CCD. The shift in the (x,y) position of the centroid in each subaperture with respect to its nominal position gives the direction and amount of the local wavefront tilt. A thin glass mirror bonded to an array of piezoelectric actuators makes up the deformable mirror. By applying control voltages to the array of actuators, the mirror surface can be deformed. The complexity of the control system and the computational power required is large as the wavefront slopes are not independent, and a least squares reconstruction of the wavefront from the $2n$ slope measurements is typically required to determine the wavefront error before each update of the n actuators. The COME-ON+ adaptive optics system operating at the European Southern Observatory is an example of this type of system [6].
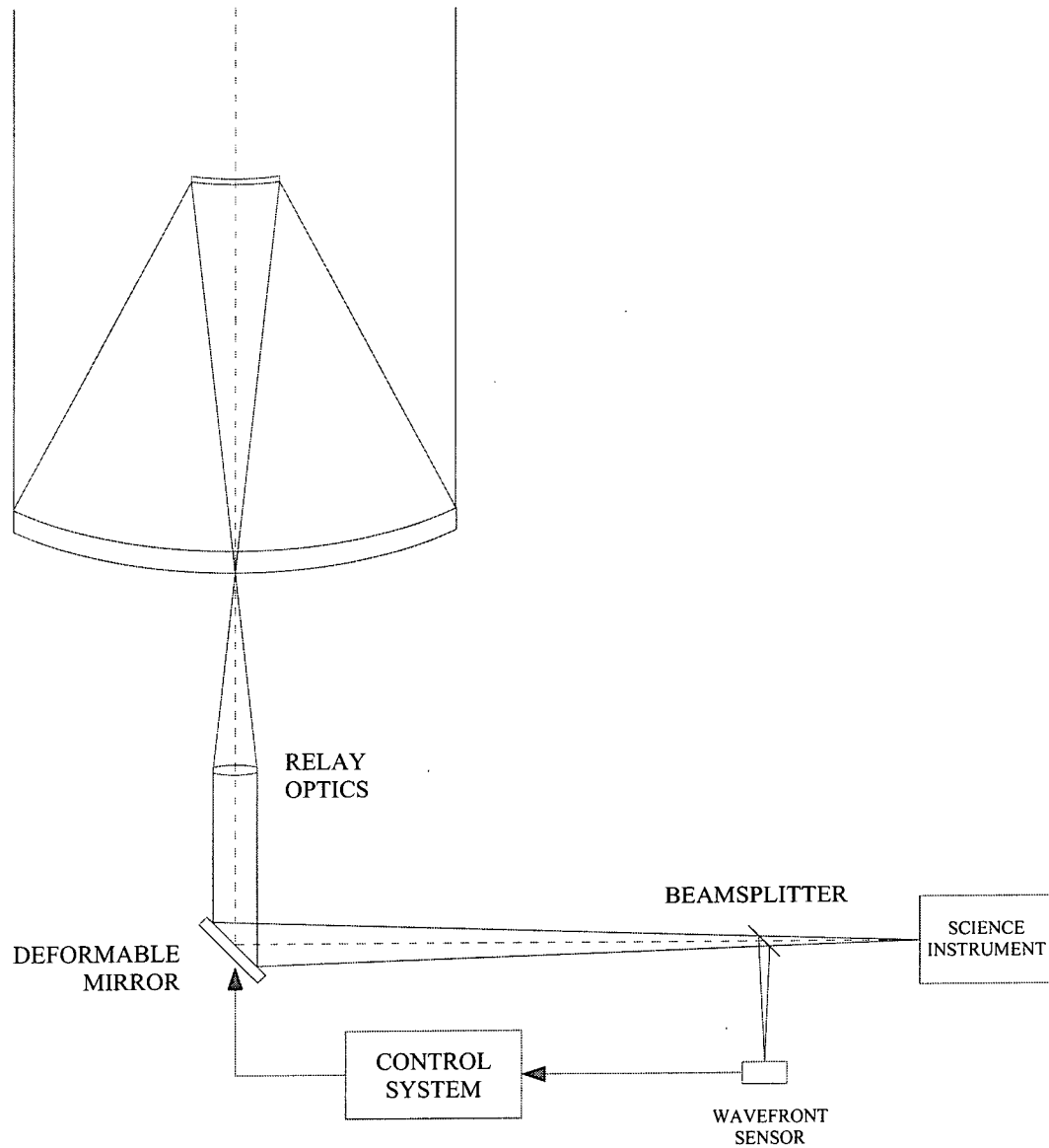
Figure 1.1: A typical adaptive optics system.
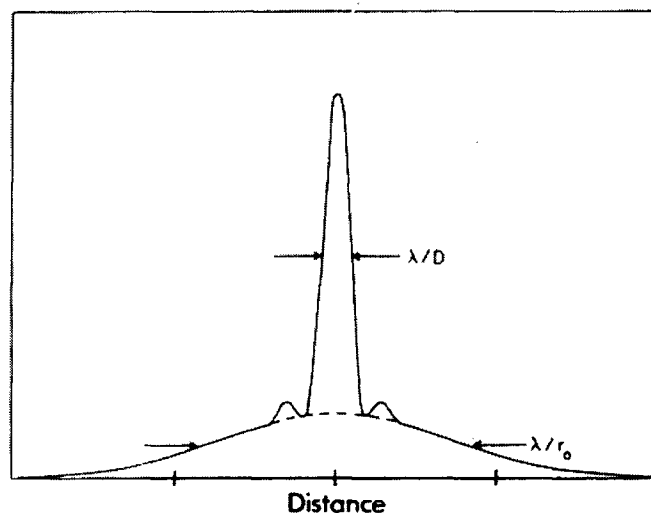
Figure 1.2: The adaptive optics point-spread function consists of a diffraction limited spike on top of a seeing limited halo. Reprinted from [2].

A more recent development involves a curvature wavefront sensor combined with a bimorph mirror, as suggested by Roddier [7]. The sensor measures the difference of oppositely defocused images of the guide star to directly determine the wavefront curvature. The bimorph mirror involves two piezoelectric disks bonded together, with the front surface polished and finished to form the reflective mirror, and an electrode array created on the back surface. The compelling feature of the bimorph is that an applied voltage changes the local curvature of the mirror surface. The wavefront curvatures of adjacent subapertures are nearly uncorrelated [7] which makes it possible to construct a much simpler control system in which each sensor subaperture is mapped to a corresponding mirror actuator. Examples of this type of system are the University of Hawaii adaptive optics system and the Canada-France-Hawaii telescope (CFHT) adaptive optics bonnette [8, 9].

The point-spread function of an adaptive optics system [2] can be expected to resemble

Figure 1.2, in which the intensity is shared between a diffraction limited spike, and a seeing limited halo. Two measures of performance related to the point-spread function are used to evaluate adaptive optics systems. The angular resolution measures the full-width at half maximum intensity of the point source images produced by the telescope. And, the Strehl ratio relates the maximum intensity in the point source image to the maximum intensity of a diffraction limited image. For an uncompensated telescope, the expected Strehl ratio is about 1% with angular resolution near 1 arcsec. With adaptive optics, a Strehl ratio of greater than 30% and angular resolution better than 100 milli-arcsec might be expected.

Adaptive optics performance is often parameterized in terms of the ratio D/r_0, where the correlation length r_0 is the scale size of atmospheric turbulence and D is the telescope diameter. In practical terms, r_0 is the diameter of the largest aperture that can be used before turbulence starts to degrade the image quality. That is, $\theta = \lambda_0/r_0$ represents the limiting angular resolution. As the turbulence increases, r_0 gets smaller. For the CFHT, the typical size of $r_0 = 20$ cm at 0.5 μm corresponds to $\theta = 0.5$ arcsec (FWHM) image quality. The natural seeing improves at longer wavelengths, so that $r_\lambda = r_0(\lambda/\lambda_0)^{6/5}$. In the I-band $r_{0.9\mu m} = 2r_0$ and in the K-band $r_{2.2\mu m} = 5.9r_0$ making the near infrared an attractive option for adaptive optics systems.

Theoretical models of the atmosphere exist [10, 11] which can be used to predict the performance of low-order adaptive optics systems. The turbulence phase disturbances are represented as a linear combination of the so-called Zernike polynomials. These are often used with circular optical apertures since they form an orthonormal basis, and are closely related to the classical aberrations such as tilt, defocus, astigmatism and so on. In this context, an adaptive optics system can be described by the radial order of Zernike terms it is able to compensate. For instance, a rapid guiding system of order n=1 would correct tip and tilt, the first two Zernike terms. An order n=2 system would correct
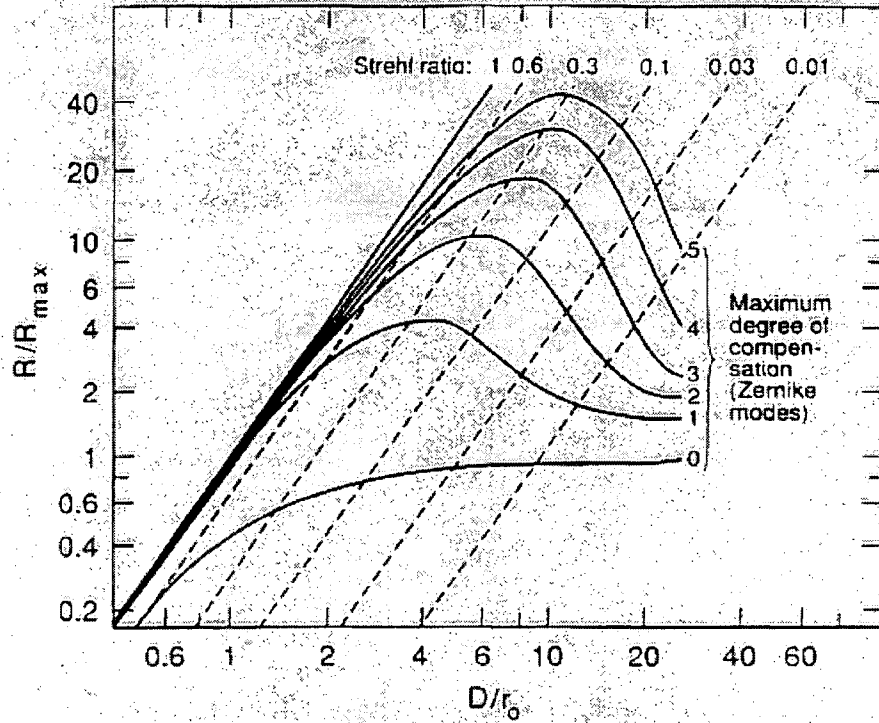
Figure 1.3: Simulations of atmospheric turbulence demonstrate the performance expected from an adaptive optics system as the order of correction is increased. Reprinted from [13].

the first five Zernike terms, including astigmatism and defocus. A more complex system of order n=4 would correct fifteen terms, including spherical aberration. The low order Zernike terms have been well described by Noll [12] and are shown in Appendix A for reference.

Figure 1.3 shows the expected performance and gains possible with low order adaptive optics systems for a range of D/r_0 values. Each curve represents the performance of an adaptive optics system in which the Zernike terms to order n have been compensated. On the vertical axis, the normalized Strehl ratio R/R_{max} measures the possible improvement relative to an infinitely large, uncompensated telescope (R_{max}). On the inset scale, the

Strehl ratio is displayed. N.Roddier generated this figure [14] by numerically expressing the atmosphere as a combination of the first several hundred Zernike polynomials, and calculating the phase variance of the resulting wavefront to arrive at the Strehl ratio. For each curve, the coefficients of the Zernike terms to order n were set to zero in the calculation to simulate the effect of the adaptive optics system.

Recently, Racine [15] has given an excellent approximation for the Strehl ratio

$$S = \frac{1 - e^{-k\sigma^{2n}}}{1 + (\frac{D}{r_0})^2} + e^{-\sigma^2} \tag{1.1}$$

where $k = 1/6$ and $n = 5/3$ give good agreement to the curves of Figure 1.3. Tables of the wavefront phase variance, σ^2, for partially corrected wavefronts [12] permit the Strehl ratio and normalized Strehl ratio to be calculated without extensive numerical simulations.

Depending on the site, low order adaptive optic systems can achieve impressive performance gains. Referring to Figure 1.3, Strehl ratios near 30% and large improvements in central intensity are possible for a wide range of D/r_0 values. For $D/r_0 < 4$, simple tip-tilt systems (n=1) can give a four-fold improvement in central intensity in the point-spread function. For $D/r_0 < 6$, a 7-actuator system (n=2) can give almost ten-fold improvement in central intensity. For $D/r_0 < 10$, a 19-actuator system (n=4) will give a factor greater than twenty improvement in Strehl ratio. Since the correlation length r_0 varies with atmospheric conditions and with the wavelength of observation, optimum operation of the adaptive optics system would require a flexible order of compensation.

It is worth noting that for a given D/r_0, compensation to Strehl ratios approaching 100% requires a much higher order of correction. And, as the number of subapertures sharing the light from the guide star increases, the relative scarcity of bright guide stars limits the useful sky coverage of these systems. In practice, the curvature sensing systems are more efficient, requiring fewer subapertures than slope sensing systems for a given

order of correction and enabling them to work with fainter guide stars.

The Coudé High Resolution Infrared Spectrograph (CHRISP) described in this thesis is a prototype adaptive optics system designed for high spatial resolution spectroscopy at near infrared wavelengths. In a collaboration between DAO and UBC, I have developed prototypes of a CCD curvature wavefront sensor and deformable membrane mirror which form the basis of the adaptive optics system. To simplify the optical design, the sensor operates in a novel manner, measuring the curvature of the wavefront from a single slightly out-of-focus image. The CHRISP prototype serves as a testbed for the single image curvature sensing technique, the prototype CCD wavefront sensor, and the deformable membrane mirror. With it, I ultimately intend to study white dwarf and other faint companions of nearby stars with the DAO 1.2-m coudé spectrograph.

1.2 Scientific rationale.

At least half of the visible stars are double or multiple and many of these have intrinsically faint companions, either white or red or brown dwarf stars for which there is very limited spectroscopic information. The secondary spectrum is hard to detect against the glare from the primary, so the details of many interesting binary systems have been hidden. Both the classification and radial velocities of the secondaries would be of considerable interest in mass determinations and knowledge of the initial mass function. For instance, current ideas of star formation rely on knowledge of the masses of stars largely obtained by the study of binary systems.

Since the ability to detect a faint companion in the glare from the primary star varies strongly with image sharpness [16], the goal of this thesis was to design and build a prototype adaptive optics system to compensate for the effects of atmospheric turbulence. Light from the primary star is diverted with a dichroic mirror to the wavefront sensor,
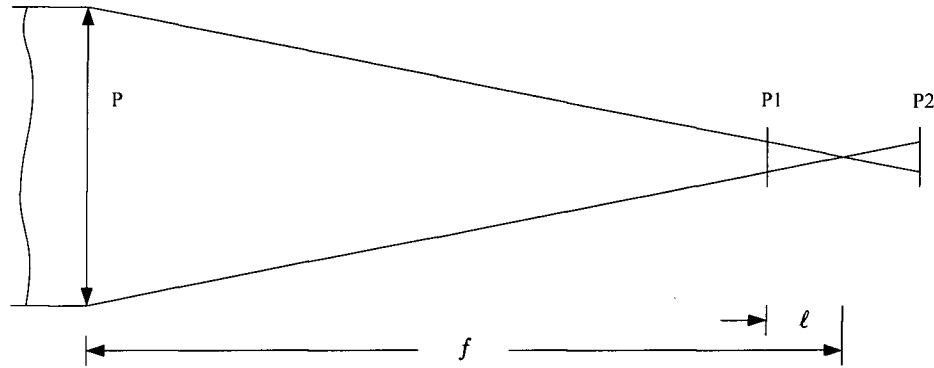
Figure 1.4: For the differential curvature sensor, two extra focal images are sampled, one on each side of the telescope focus. For the single image curvature sensor, only the image in plane $P1$ or $P2$ is required.

which provides an instantaneous measure of atmospheric wavefront distortion. That is, the primary star serves as a natural guide star. A deformable mirror is used to introduce a wavefront correction to sharpen the images of both stars. The improved concentration of light in the primary and secondary star images and the diversion of the primary light should greatly enhance the contrast of the faint companion against the background of scattered light from the primary.

1.3 Curvature sensing.

F.Roddier and collaborators [17, 18] have developed an elegant sensor which directly measures the curvature of the wavefront (and its radial slope) from the difference between oppositely defocused images of the guide star. A description of the curvature sensing principle is given in Appendix B. A variation on this scheme derives the curvature signal from a single defocused image and the mean intensity over the aperture [19, 20].

With the intensity $I(\vec{r})$ measured in plane P1 (as shown in Figure 1.4), at the geometric optics approximation it can be shown that

$$\frac{\Delta I}{I_0} = \frac{I(\vec{r}) - I_0}{I_0} = \frac{f(f - \ell)}{\ell} \left[P \cdot \nabla^2 z(\vec{u}) - \delta(u - R) \cdot \frac{\partial}{\partial u} z(\vec{u}) \right]_{\vec{u} = f\vec{r}/\ell} \tag{1.2}$$

where the $\nabla^2 z$ term represents the two dimensional Laplacian of the wavefront surface, and the circular $\delta(u - R)$ term represents the derivative at the edge of the telescope entrance pupil, P. The parameters are the focal length f, and the distance ℓ of the detector from the focal plane. The mean intensity for a uniformly illuminated circular image is I_0. Essentially, the sensor operates by comparing the instantaneous image $I(\vec{r})$ to the uniform reference model, I_0.

In a practical wavefront sensor, the defocused image of the guide star is divided into a number of subapertures. Within each, the local intensity is integrated. The curvature is then the normalized difference between each subaperture signal and a suitable constant. The constants are the expected signals within each subaperture for a uniformly illuminated circular image. These can be obtained by dividing the total signal by the fractional area of each subaperture. Wavefront tilts are sensed by an excess or lack of illumination in the boundary subapertures.

Compared to the differential technique, single image curvature sensing requires the computation of the mean signal inside the pupil area of the sensor, but allows a much simpler optical arrangement. Since the incoming starlight is not split between two detectors, it has the potential to work with fainter guide stars.

A single image sensor cannot cancel noise due to atmospheric scintillation. However, for practical astronomical systems, Hickson [19] has shown that the scintillation noise is small compared to the curvature signal.

1.4 CCD wavefront sensor.

The rationale for investigating CCD wavefront sensors involves detector performance, simplicity of design, and flexibility in the operation of the adaptive optics system. Small format, high quantum efficiency, low noise, rapid readout devices have become an attractive alternative to avalanche photodiode (APD) based sensors. Frame transfer capability allows the guide star to be (almost) continuously monitored and provides shutterless operation.

As a standard to compare against, the CFHT adaptive optics bonnette uses a sensor composed of 19 avalanche photodiodes which alternately detect the before and after focus images [9]. A complex, fixed arrangement of prisms defines the subapertures and directs the guide star light to the detectors via optical fibers. To avoid the expense and difficulty of assembly and alignment, a simpler CCD arrangement is an attractive alternative.

The higher quantum efficiency of CCD detectors can give an advantage over APD detectors, even though the APD is virtually noiseless, as detailed in Appendix D and shown in Figure 1.5. For reasonable device parameters, a single image CCD sensor can outperform the APD sensor for a read-noise of less than $2.5e^-$.

Versatility in the CCD wavefront sensor (and deformable mirror) allows the adaptive optics system to be optimized for particular observations, which depend on the available guide stars, the wavelength range, and the atmospheric conditions. Compared to the APD-prism sensor which is restricted to sampling a fixed subaperture pattern, the CCD allows different patterns of subapertures through software control of the CCD readout. That is, the guide star image can be read into 7, 13 or 19 subaperture patterns, allowing a variable order AO system.

For the CHRISP system, the prototype wavefront sensor is constructed from a low-noise frame transfer 64×64 CCD with a DSP56002 based CCD controller. The wavefront
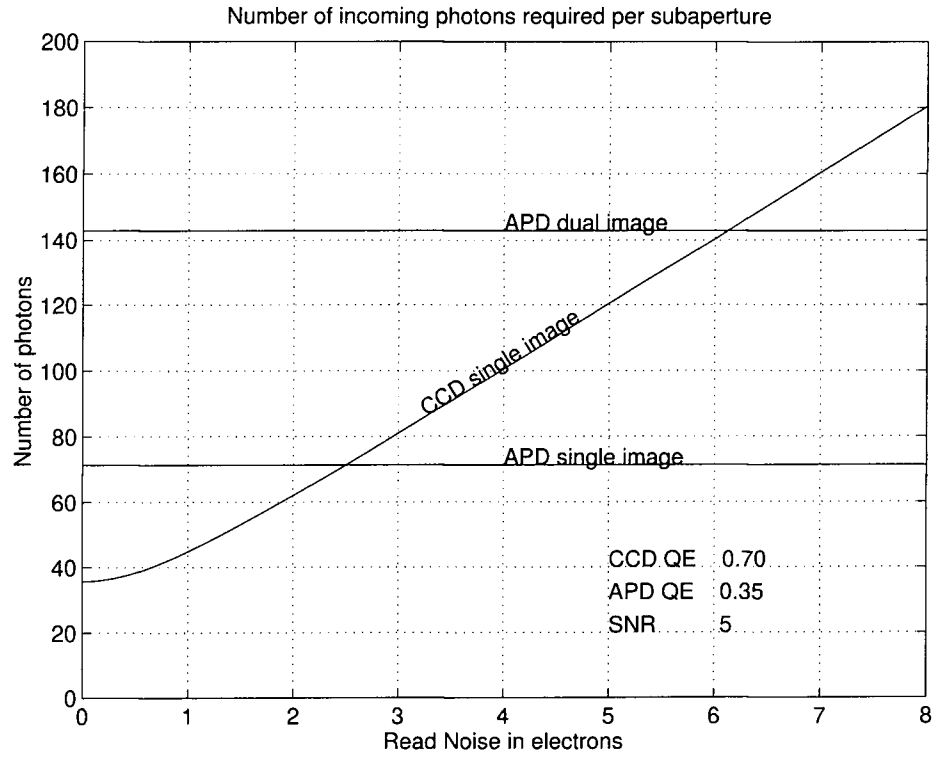
Figure 1.5: Performance comparison of dual and single image APD and CCD sensors. The CCD quantum efficiency is 0.7, the APD quantum efficiency is 0.35, and the SNR per subaperture is 5.

sensor is versatile in the sense that the serial binning pattern and the number of subapertures are software controlled. The wavefront sensor is described in a later chapter.

1.5 Wavefront correction.

For an electrostatically deformable membrane mirror, the steady state behavior of the membrane surface is described by the Poisson equation [21]

$$\nabla^2 z = \frac{P}{T} \qquad \text{and} \qquad P = \frac{\epsilon_0 V^2}{\ell_0^2} \qquad (1.3)$$

with membrane deflection z (m), electrostatic pressure P (Nm^{-2}), membrane tension T (Nm^{-1}), applied actuator voltage V, membrane to electrode spacing ℓ_0 (m), and $\epsilon_0 = 8.85 \times 10^{-12}$ in MKSA units.

With the appropriate bias configuration the curvature of the membrane surface varies with the applied actuator signal voltage. This property makes it nearly ideal for low order wavefront curvature correction. Intriguing features of the membrane mirror are its lack of hysteresis, single moving part, and initial optical surface quality which can be as good as 0.03λ rms [22]. The simple structure with no complex solid moving actuators suggests reliable operation is possible.

For the CHRISP system, we have designed and built a prototype unit with simple bias and driver electronics. The prototype features a 100 mm diameter aluminized nitrocellulose membrane, and 31 actuators arranged concentrically. The actuators can be grouped to provide 7, 13 or 19 element patterns. With the proper bias configuration, the unit can provide low order (including tip-tilt) wavefront correction. Details of the device and design rationale are presented in a later chapter.

The adaptive optics control system exploits the fact that the wavefront sensor provides a curvature signal, while the membrane mirror surface curvature varies with applied voltage. The deformable mirror electrode array is designed to match the wavefront sensor array, so that a simple zonal control system is possible.

The CCD controller digital signal processor processes the wavefront sensor signal to extract the curvature signal and provide feedback signals to the membrane mirror in real time. The DSP uses the idle time between CCD readouts to perform control system tasks.

1.6 Site characteristics and performance estimates.

Anecdotal evidence suggests that the seeing at DAO 1.2-m telescope is routinely in the 2.0 to 4.0 arcsec range, and on occasion can be close to an arcsecond. On several nights, we used the CCD wavefront sensor to directly observe several stars near the zenith, and were able to confirm that the seeing at the DAO can be in the 1.0 to 2.0 arcsec range. At least some of the time, we expect that the seeing will be about one arcsecond, corresponding to an r_0 in the I-band of 20 cm so that $(D/r_0) \simeq 6$. From Figure 1.3, the order of correction should be n=2 or better to produce "diffraction limited" images with Strehl ratios near 30%, and a gain in central intensity close to 10.

Figure 1.6 shows a sample of the seeing conditions at DAO. These frames are typical of the results seen in longer series of exposures. There are moments of exceptional seeing, where the image FWHM is less than 0.5 arcsec. There are moments when the image breaks up into individual speckles, within a 1.5 arcsec diameter envelope. And, there are moments of blooming when the image is smeared out over the entire wavefront sensor. On this particular night, a 1.0 second exposure shows the natural seeing to be about 1.5 arcsec (with a bit of coma in the image). Additional seeing related measurements are described in later chapters.

The curvature sensing criteria specifically require that the image blur scale and the demagnified atmospheric distortions be related by

$$\frac{\lambda f}{r_0} < \frac{r_0 \ell}{f} \qquad \text{or} \qquad (\frac{D}{r_0})^2 < \frac{a}{\lambda F} \tag{1.4}$$

where the f-ratio is $F = f/D$, the defocused guide star image diameter on the CCD sensor is a, and the other parameters have their usual meanings. For the design value of f/30, and an image size a =(48 pixels)(15μm)= 720 μm, the corresponding value is $D/r_0 < 7$. Again, this is a practical regime for low-order correction at the DAO 1.2-m telescope (at least some of the time).
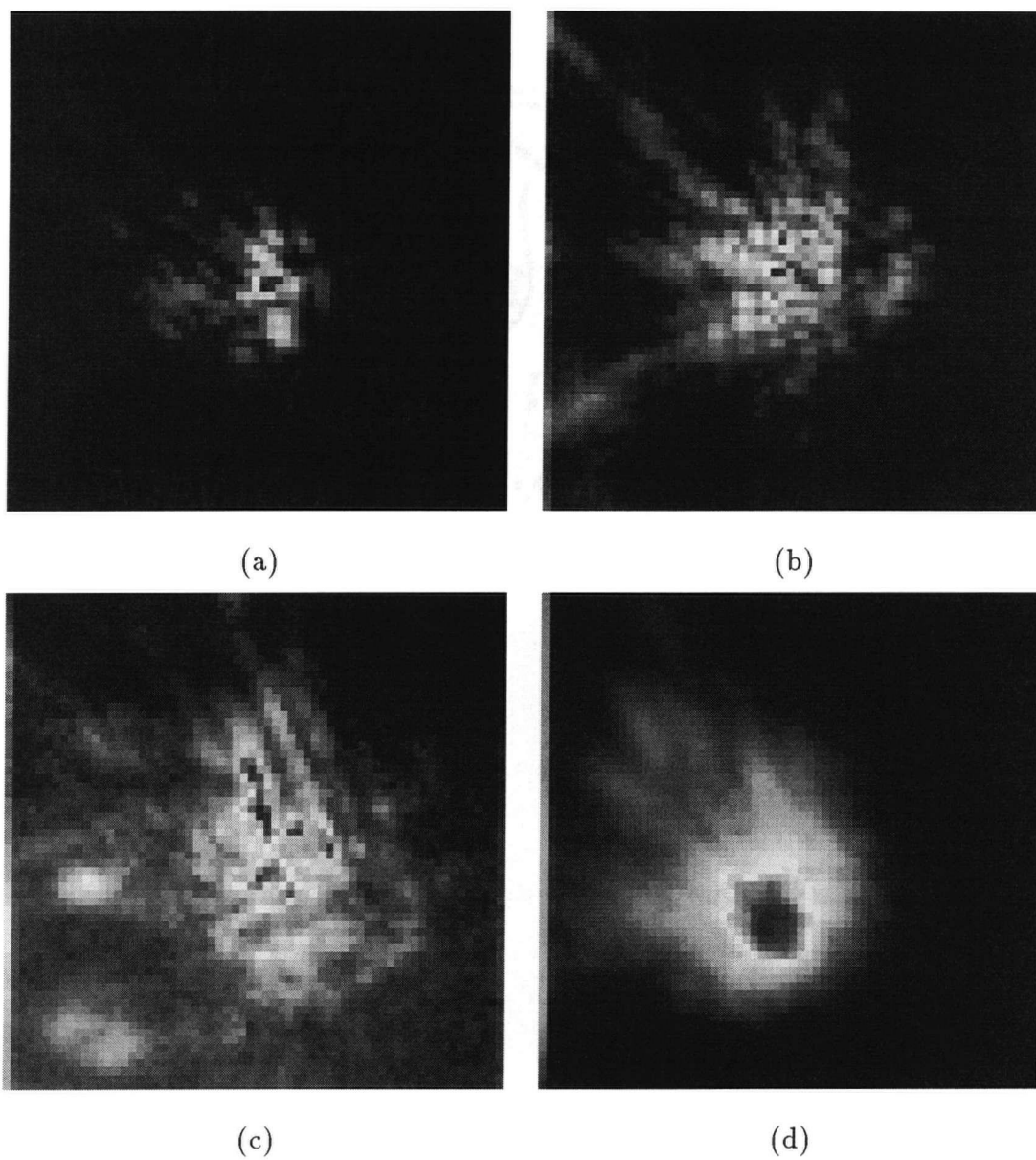
Figure 1.6: Star image samples recorded at the DAO 1.2 meter telescope with the proto-type wavefront sensor. Each V-filter image is 64×64 pixels or 5×5 arcsec^2. (a) Excellent seeing 0.5 arcsec, 20 ms exposure, (b) Speckles within a 1.5 arcsec envelope, 20 ms exposure (c) Poor seeing, 20 ms exposure (d) 1.5 arcsec seeing, 1000 ms exposure.

The timescale for atmospheric turbulence can be estimated as $\tau_0 = r_0/\langle v \rangle$, assuming that the turbulence is "frozen-in" and blown by the telescope at effective wind speed $\langle v \rangle$. For $r_0 = 20$ cm and $\langle v \rangle = 10$ ms^{-1}, then $\tau_0 = 20$ ms. The wavefront sensor integration time must be several times smaller to effectively oversample the turbulence and allow the control loop to operate reliably. Using this estimate, a wavefront sensor sampling rate of several hundred frames per second could be required.

The magnitude of the guide star required by the adaptive optics system is largely determined by the telescope diameter, number of subapertures, and the sampling time. With faint guide stars, the limited flux of photons available requires a trade-off to minimize the sampling time, and optimize the number of subapertures. The balance between these two will depend on the observing conditions (D/r_0). For an optimized CCD sensor, the expected natural guide star magnitudes are shown in Figure 1.7, for order of correction $n = 1 \ldots 4$. Details of these calculations are given in Appendix C. For larger telescopes, these curves simply translate upwards. For instance, for the CFHT with $D = 3.6$ m, the curves are shifted by 2.4 magnitudes. Increases in telescope diameter are partially offset by an increased D/r_0 which requires a higher order of correction and a larger number of subapertures.

At the 1.2-m telescope, the adaptive optics system will be limited by the relatively small aperture to guide stars brighter than 14th magnitude for n=2 and a sampling time of 5 ms. Since this is a testbed system optimised for the task of searching for faint companions around nearby stars, the restriction is minimal.

1.7 Goals for the thesis.

The primary goals for this thesis were to design and build a proof-of-concept adaptive optics system to illustrate a simplified approach to adaptive optics, and to demonstrate
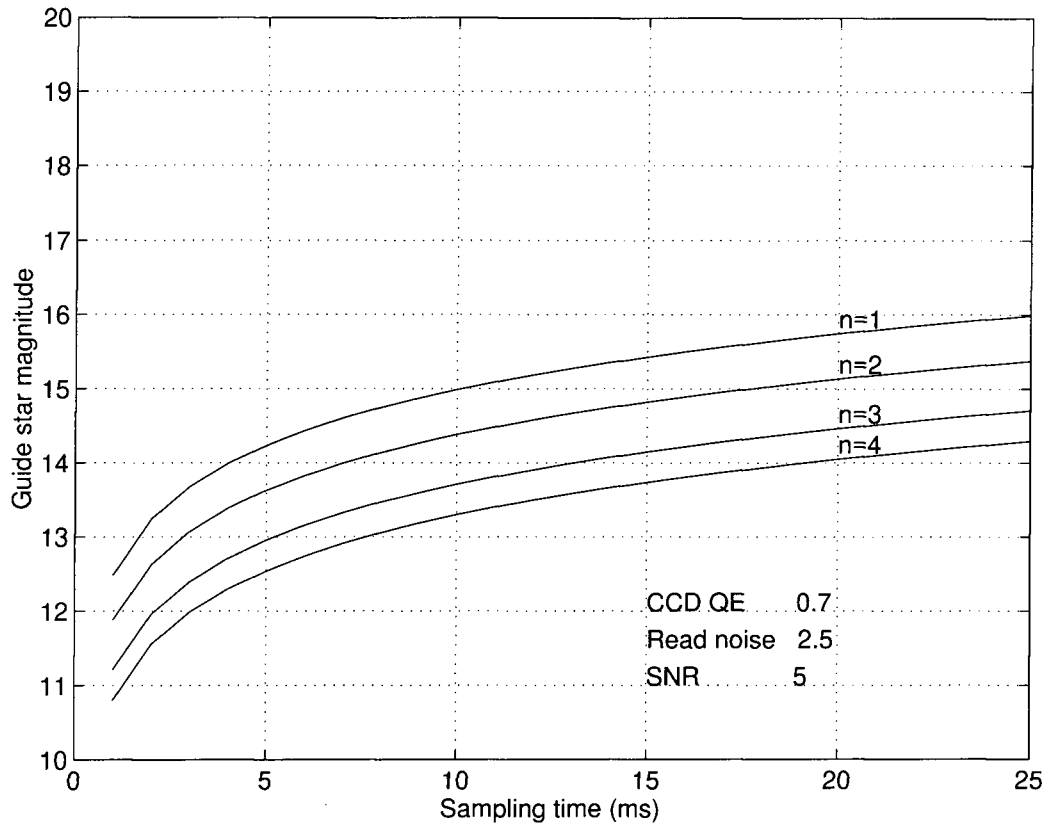
Figure 1.7: Guide star magnitudes for the DAO 1.2-m telescope. The calculation assumes a CCD quantum efficiency of 0.7, read noise of $2.5e^-$, a SNR per subaperture of 5, and the number of superpixels per subaperture of 8.

the properties of the components used to implement it. The CCD wavefront sensor used as a single image curvature sensor drastically reduces the complexity of the wavefront sensor and the relay optics compared to an APD or lenslet array sensor. A membrane mirror is used in place of expensive, difficult to fabricate piezostack or bimorph mirrors. The membrane mirror performs both tip-tilt and low order Zernike mode corrections, eliminating a separate tip-tilt mirror found in almost all other systems. The overall optical system was constructed from simple flat mirrors, a single off-the-shelf lens, and a dichroic. This is in contrast to other systems which often involve custom, off-axis

parabolic or elliptic optics. These three simplifications make the CHRISP system distinct from other existing adaptive optics systems, and provide the rationale for developing it.

Original contributions made in the thesis include the development and demonstration of a prototype CCD curvature sensor and membrane mirror, and the demonstration of single image curvature sensing. The CCD curvature wavefront sensor, with a new CCD controller architecture, permits a software programmable readout scheme for fast frame rates with low-noise readout. A wide variety of subaperture patterns can be implemented, with the possibility of changing them on-the-fly. The design of the membrane mirror, including improvements to the existing designs, with simplified bias and driver electronics was reviewed for patentability [23]. The tip-tilt capability of the membrane mirror was simulated and measured, and a dynamic tip-tilt test was introduced to measure the membrane mirror step response. Single image curvature sensing was demonstrated both by detecting a spherical aberration introduced into an optical system, and in the closed-loop zonal control of the testbed adaptive optics system. All of these contributions are described in the following chapters.

Chapter 2

Versatile CCD curvature wavefront sensor

2.1 Introduction and Background.

Curvature sensing is one technique for deriving the variations in wavefronts distorted by thermal turbulence in the atmosphere [7]. The rationale for developing a versatile CCD wavefront sensor involves detector performance, simplicity of design, and flexibility in the operation of the adaptive optics system.

The requirements for a wavefront sensor are fairly straightforward. High quantum efficiency, wide dynamic range, and low noise properties are essential to operate with faint guide stars. Fast frame rates and shutterless operation are preferred to adequately sample the turbulence bandwidth. The detector should provide good spatial sampling of the subaperture patterns. Ease of calibration and integration of the device into the adaptive optics system must also be considered.

Small format CCD detectors appear to be well suited for wavefront sensing applications. Current technology allows high quantum efficiency devices with rapid readout and frame transfer. Serial register binning reduces the number of pixels for low noise operation at rapid frame rates. A frame transfer architecture allows the source to be almost continuously monitored and provides shutterless operation. In terms of fabrication and alignment in an optical system, the simplicity of a CCD is appealing. And, in some instances, a smart CCD controller can double as the adaptive optics servo-control processor.

The prototype wavefront sensor is constructed from a low-noise frame transfer 64×64
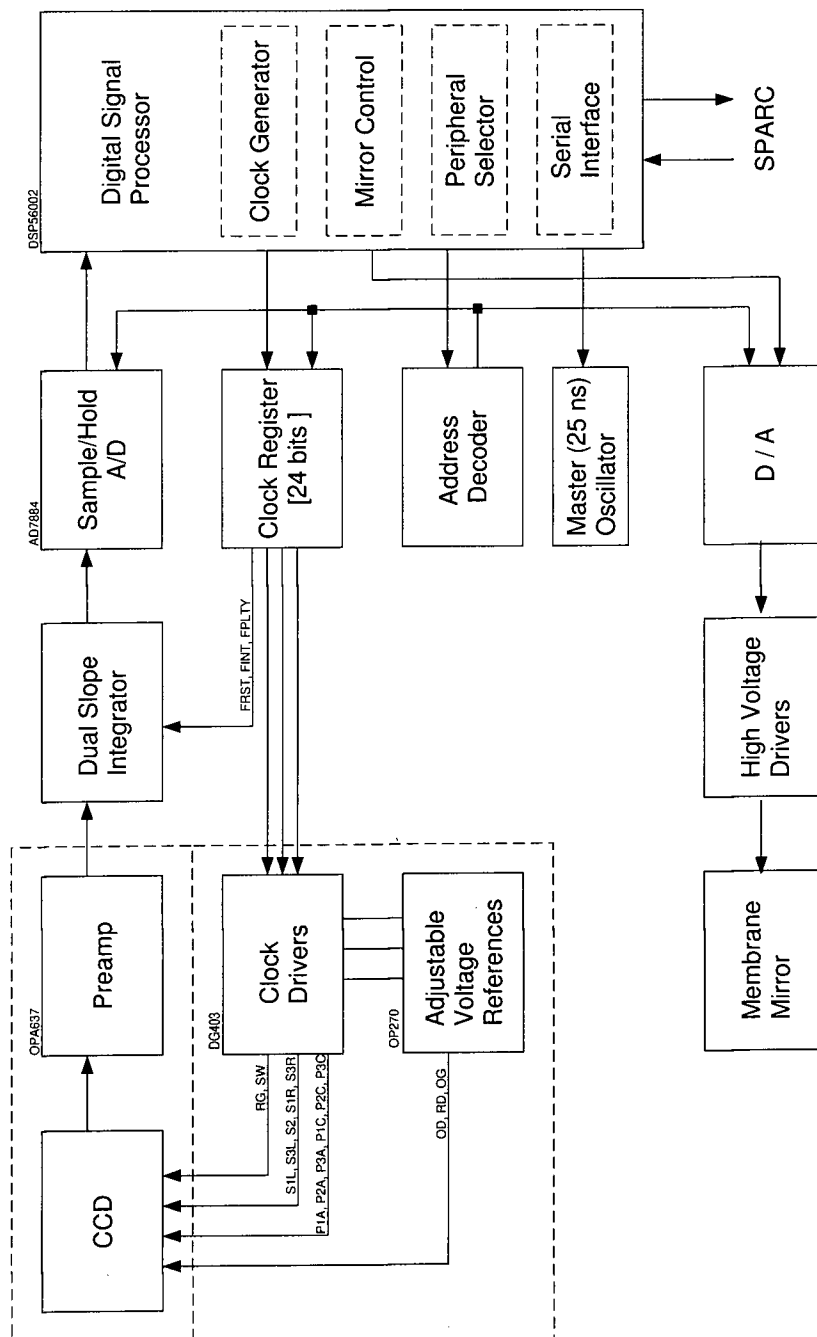
Figure 2.1: Block diagram of the AO system. The digital signal processor acts as the CCD controller as well as the overall adaptive optics control system.

CCD with a digital signal processor (DSP) based CCD controller [24]. Figure 2.1 is a block diagram which illustrates the various parts of the sensor. The controller provides bias voltages, three phase clock signals to the parallel and serial registers, signal processing to extract and digitize the CCD output signal, and a serial interface to a host computer.

On the CCD, the out-of-focus image of the guide star is divided into a number of subapertures, as shown in Figure 2.2 for example. The key to a practical sensor is to read the array by binning the serial register on a line by line basis according to the subaperture pattern, so that the number of "superpixels" read is a minimum. Following this approach permits low noise readout with fast frame rates. Initial 2×2 binning of the 64×64 device reduces the number of pixels to be read to 1024. Further superpixel binning in the serial register during readout reduces the number of read operations to about 200. The number of pixels per superpixel depends on the line of the CCD being read, and on the pattern being sampled. For example, in Figure 2.2(c), each subaperture has about 25 elements of the 32×32 grid which are read as approximately 8 superpixels.

While there are many existing CCD controller designs, not all would be suitable for operating a small frame transfer CCD as a wavefront sensor. Some of these demonstrate useful features such as software programmability, numerous clock signals, fast clock rates, multiple amplifier gain settings, and operating point voltages controllable over a very wide range [25, 26]. Others are optimized for low-noise performance at slow scan rates [27] or bare simplicity [28, 29]. The prototype which I have designed and built for this project is an attempt to synthesize the key elements into one design. A high level of integration is achieved by the extensive use of a DSP and its peripherals, eliminating external sequencers and state machines, wait state generators, clocks and counters found in other designs. Some features of the various designs such as dual-speed readout, operation of multiple devices, expansion beyond four amplifiers, fiber optic data links, and VME
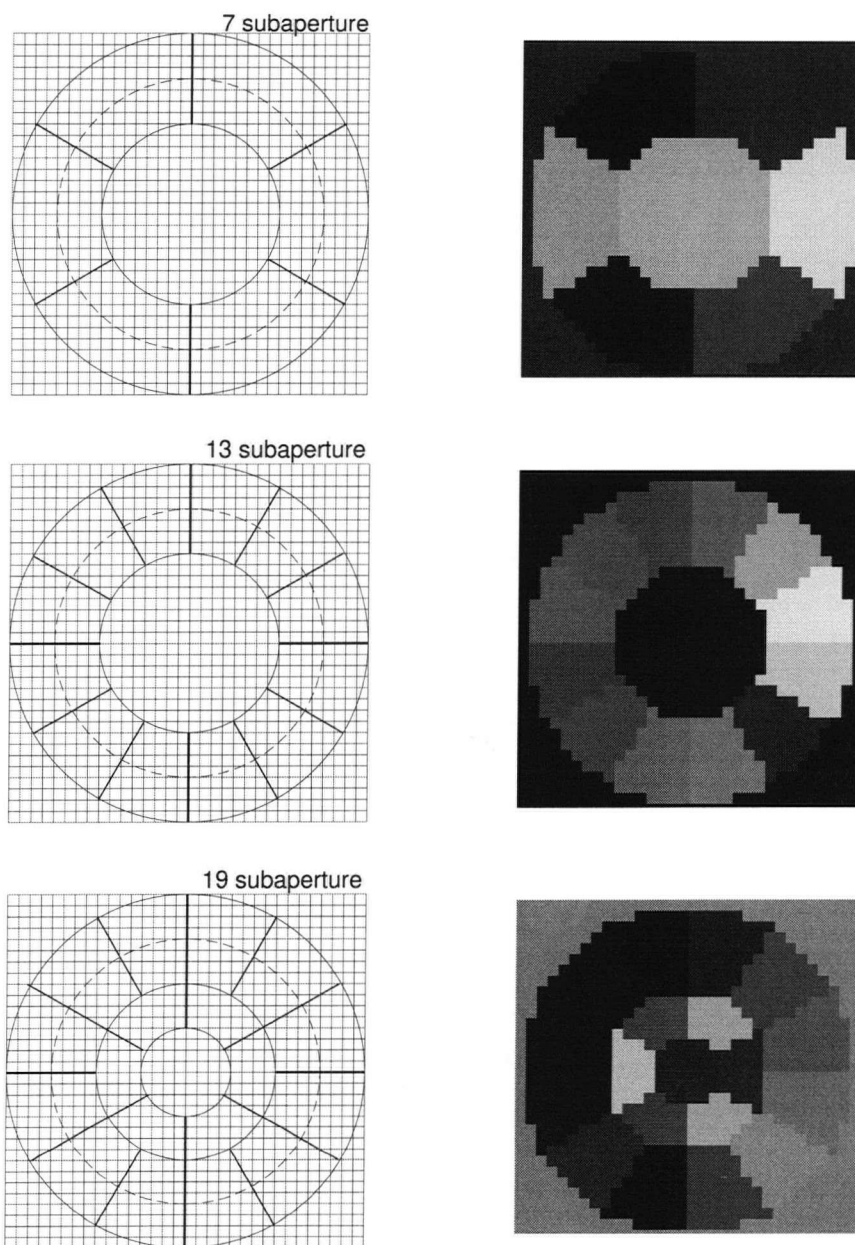
Figure 2.2: Sample readout patterns. The defocused guide star image can be sampled with various subaperture patterns through software configuration of the CCD readout. The dotted line represents the outline of the spot produced by the defocused beam. Wavefront sensor images (on the right) are 10 ms exposures taken in the lab showing the programmed subaperture patterns.

based data interfaces are not included to simplify the hardware design. Some timing and software complications are avoided by excluding features such as directly writing the clock waveforms to high speed digital-to-analog converters [30] for each clock transition.

For the prototype sensor, a digital signal processor based controller delivers the flexibility and computational power required to perform the serial register binning, to adapt to different subaperture patterns through software control, and to extract the curvature signal from the sensor image. Versatile and programmable clock sequencing, and low noise operation were the main design requirements. The DSP directly generates the sequences used to clock the serial and parallel charge transfers on the CCD. Extra clock lines are provided for frame transfer and split serial register operation. The DSP also controls the dual slope integrator, and accepts the filtered and digitized output from the A/D converters. The design of the dual-slope integrator and clock drivers borrows some details from previous UBC efforts [27].

2.2 Frame transfer CCD.

The prototype CCD curvature wavefront sensor uses a 64×64 frame transfer device designed by J.Geary and fabricated by Loral on a joint UBC-SAO wafer run. The 64×128 array is made up of four sections of 64×32 pixels, each independently clocked (as shown in Figure 2.3). Each end of the device has a split serial register with two output amplifiers. The specifications for the device are given in Table 2.1.

The frame transfer architecture allows fast frame rates, while providing a readout rate consistent with low read noise performance. At the end of each integration time, the recorded image charge is rapidly shifted from the illuminated area to the readout area of the device. Provided this transfer is fast compared to the integration time, a reasonable extinction ratio is maintained and a shutter is not required. The device is
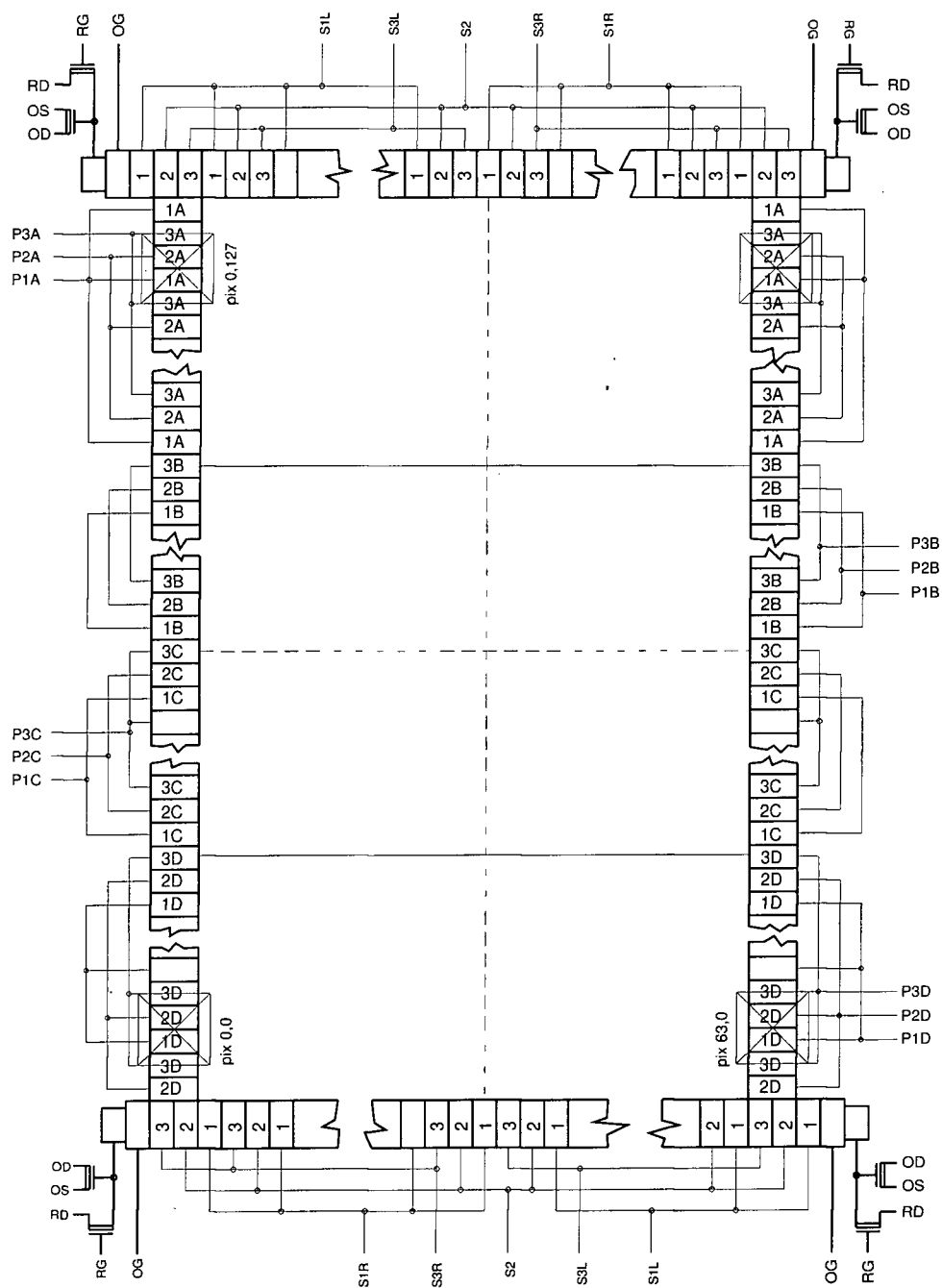
Figure 2.3: Frame transfer 64×64 CCD. The device is constructed as four independently clocked sections of 64×32 pixels to permit frame transfer. Each serial register has two output amplifiers. The CCD is thermoelectrically cooled to reduce the dark current.

Table 2.1: Wavefront sensor CCD specifications.

Parameter	Value	Units
Image area	64×128	pixels
Quantum efficiency	~40	%
Read noise	10	e^-
Readout rate	20	μs per pixel
Dark current (300 K)	120	pAcm^{-2}
Pixel size	15	μm
Output registers	2	
Output amplifiers	4	
Amplifier gain	1.5	μV per e^-
Package size	68	pin LCC

illuminated on one side (64×64) with frame transfer to the other side, although it could be illuminated on the central 64×64 pixels with frame transfer to the 64×32 areas at each end for readout using all four output amplifiers.

In order to reduce the dark current and to allow the CCD amplifiers to operate with lower thermal noise, the CCD is thermoelectrically (TE) cooled. At room temperature, the measured dark current of 120 pAcm^{-2} is noticeable even in short (10 ms) exposures. At a target operating temperature of -40°C, the dark current is reduced [31] to 0.8 pAcm^{-2}, which would result in less than one-tenth electron per 10 ms exposure per pixel.

Putting the CCD in a vacuum housing allows efficient cooling and avoids condensation onto the CCD. Two low noise preamplifiers are located inside the dewar close to the CCD to avoid noise pickup. The CCD is clamped into a socket on the header circuit board in contact with the TE cooler cold side. The CCD header board is supported by stainless steel standoffs. Low thermal conductivity constantan wires connect the CCD inputs and preamplifier outputs to the electrical connectors. Figures 2.4(a) and 2.4(b)

Figure 2.4: Photographs of the wavefront sensor CCD and vacuum housing. (a) Visible details include the 68-pin CCD package, the circuit board and socket, numerous signal traces, and the o-ring seal for the housing. (b) Visible details include the support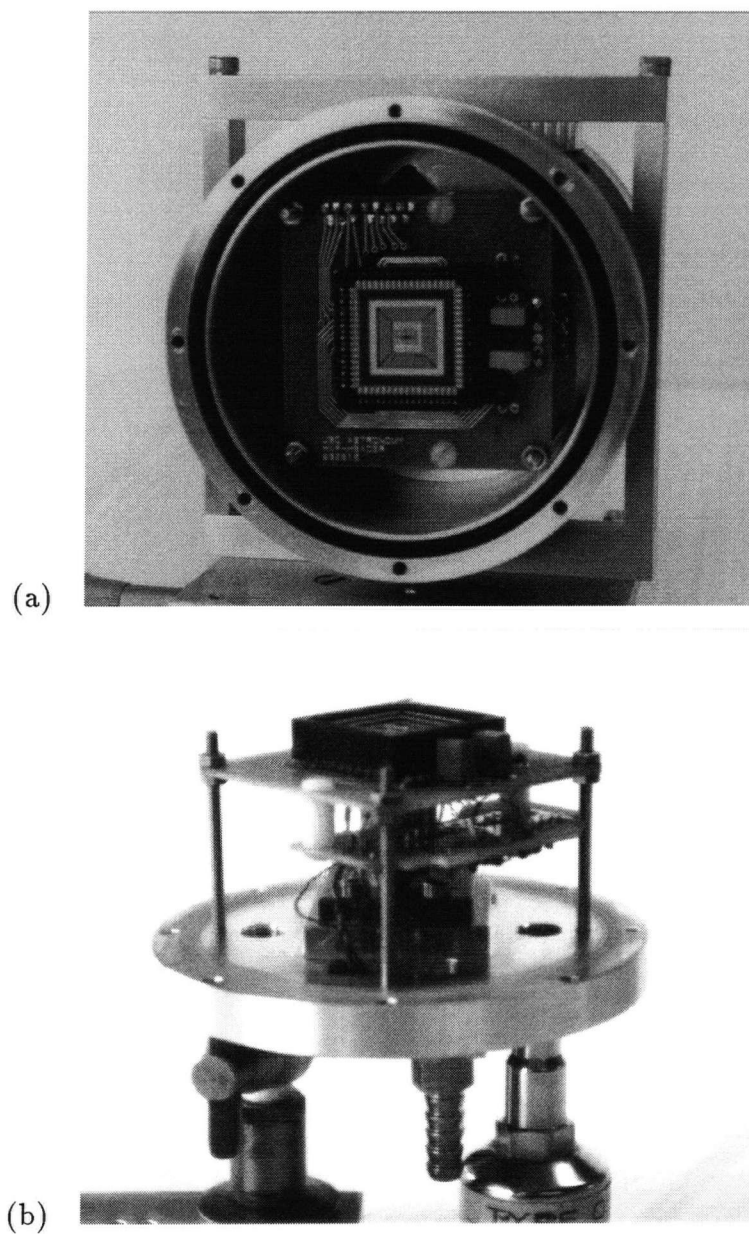 system for the CCD and preamplifier circuit boards and the heat sink arrangement for the TE cooler directly under the CCD. The mounting arrangement permits the housing to be rotated.

are photographs of the wavefront sensor showing these features.

The TE cooler is rated for a ΔT of 77°C under ideal no-load conditions with a current of 1.2 amps [32]. With an estimated convective and conductive heat load [33] of 500 mW, a ΔT of 50°C was expected in operation. An adjustable current source provides the current driven through the TE cooler. A platinum resistive sensor in contact with the TE cooler cold side monitors the temperature of the CCD.

A water cooled heat sink bolted to the housing baseplate proved very effective at removing the heat from the TE cooler hot side. Even at low flow rates, the CCD vacuum housing, mounting bracket and translation stages were rapidly chilled to the water temperature (nominally 10°C at the telescope).

In its original housing, it proved impractical to keep a vacuum for more than a few hours. The convective load on the thermoelectric cooler limited the CCD temperature to about -20°C. Even with a leak detector, we could not identify the source of the problem and were resigned to operate the wavefront sensor with a partially evacuated housing and degraded TE cooler performance. As suggested by J.Stilburn [34], we filled the housing with xenon gas at atmospheric pressure. Not only did this remedy the leak problem, the effectiveness of the cooler was improved so that a CCD temperature near -30°C was achieved at the telescope.

2.3 DSP description and clock generation.

The versatility of the controller stems from the use of a Motorola 24-bit DSP56002 digital signal processor [35]. On-chip resources permit the DSP to run code from an internal program memory, and to use two internal data memories for storage. External 32K SRAM memory is available as necessary. The DSP runs at a clock frequency of 40 MHz and has a 50 ns instruction cycle. DSP instructions are typically executed in

one cycle. The speed of the processor allows the CCD clocking sequences to be directly generated by the DSP under program control, ensuring versatility of the sequencing. Communication with a host Sparcstation is available via both a fast SBUS serial link and a slower RS-232 monitor channel, using on-chip DSP peripherals.

In order to perform the serial and parallel charge transfers on the CCD, the clock signals are generated from sequences stored in the on–chip DSP data memory. Each bit of the 24 bit DSP word represents one of the control signals. With 24 bits, there are control signals for the two sets of parallel clocks necessary for frame transfer [P1A-P2A-P3A, P1C-P2C-P3C] and the two sets of serial clocks necessary to use amplifiers at each end of the serial register [S1R-S3R-S2-S1L-S3L-RG]. Other signals control the pixel conversion functions such as the dual slope integrator on/off and polarity, integrator capacitor reset, and A/D converter start [$\overline{\text{FINT}}$, FPLTY, $\overline{\text{FRST}}$, $\overline{\text{CONVST}}$]. Spare bits allow additional signals for a summing well, transfer gate, or a shutter to be added.

The clocking sequences generated by the DSP are assembled from sequence fragments loaded from the host computer and stored in the on-chip memory. To perform an operation such as a serial or parallel shift, the DSP steps through and writes the sequence of data words into an external register via the DSP external bus. Each sequence fragment is held in the external register for a preset number of clock cycles, as coded into the DSP control software. The number of clock cycles (hold time) determines the timing of the clocks to the CCD. A typical timing diagram and the sequence fragments used to produce it are shown in Figures 2.5 and 2.6. As illustrated, each sequence occupies only a few data words.

Normally, for parallel transfers or frame transfer, the serial clocks and dual slope integrator control lines are held in a pre-specified state dictated by the CCD architecture. Similarly, the serial transfers require that the parallel clock lines be held in a specified state, possibly an MPP mode as illustrated here. This allows all control lines to be
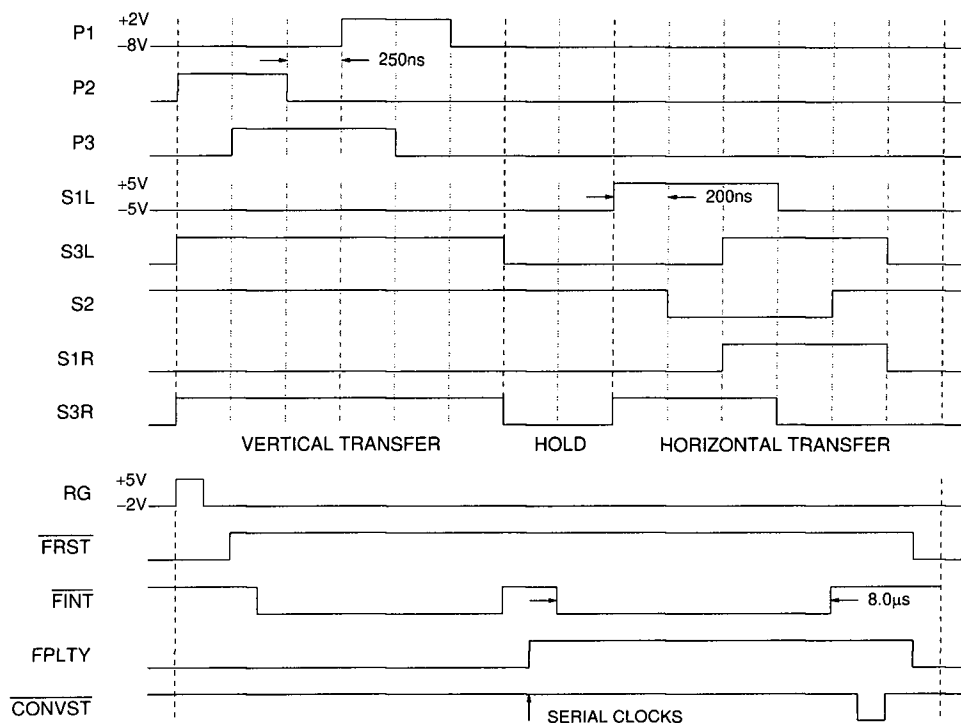
Figure 2.5: Sequencing diagram. The sequence of signals applied to the CCD for charge transfers and correlated double sampling is detailed here. The sequences are applied to the parallel clocks, serial clocks, reset transistors, and the control lines for the dual slope integrator.

generated simultaneously as one 24-bit word. The assignment of control signals to the 24-bit DSP word is given in Figure 2.6.

An external 24-bit register is used to retime the CCD sequence data. Each data word is held in the register until it is overwritten by the next sequence fragment. The external register appears as a memory mapped zero wait state peripheral in the DSP address space, allowing a timing resolution of 50 ns. From the external register the clock sequences are transmitted by line drivers in differential form to the clock drivers located near the CCD housing.

Bit	Signal	Frame transfer	Parallel readout	Parallel flush	INT+	INT	Serial transfer	Serial flush
D23	P1A	000110	000110	000110	00000	00000	000000	000000
D22	P2A	110000	110000	110000	00000	00000	000000	000000
D21	P3A	011100	011100	011100	00000	00000	000000	000000
D20	P1C	000110	000000	000110	00000	00000	000000	000000
D19	P2C	110000	000000	110000	00000	00000	000000	000000
D18	P3C	011100	000000	011100	00000	00000	000000	000000
D17	TG							
D16	SPARE							
D15	S1L	000000	000000	111111	00000	00000	111000	111000
D14	S3L	111110	111110	111111	00000	00000	001110	001110
D13	S2	111111	111111	111111	11111	11111	100011	100011
D12	S1R	000000	000000	111111	00000	00000	001110	001110
D11	S3R	111110	111110	111111	00000	00000	111000	111000
D10	RG	000000	000000	111111	10000	00000	000000	111111
D9	SW							
D8	SPARE							
D7	*FRST	000000	000000	000000	01111	11110	111111	000000
D6	*FINT	111111	111111	111111	11011	01111	111111	111111
D5	FPLTY	000000	000000	000000	00001	11110	111111	000000
D4	*CONVST	111111	111111	111111	11111	11011	111111	111111
D3	SPARE							
D2	SPARE							
D1	SPARE							
D0	*BUSY	000001	000001	000001	00001	00001	000001	000001

Figure 2.6: Sequence fragments. The clock and control signals are generated by stepping through a series of sequence fragments and writing each to the output register.

2.4 Circuit descriptions.

Clock drivers are necessary to convert the logic level signals from the clock generator to the voltage levels required by the CCD. As shown in Figure 2.7, the circuit topology is based upon a fast analog switch. Prototypes of this circuit indicate that switching times are approximately 100 ns. The rise/fall time of the output is about 50 ns, with propagation delay through the switch accounting for the rest. The analog switch output is either V_H or V_L depending on the input control sequence. Clock drivers are provided for each of the control signals to the CCD, plus a few spares for future use.

The output voltage levels produced by the clock drivers are derived from op-amp voltage buffers. Separate voltage regulators are used for the reset driver, the parallel
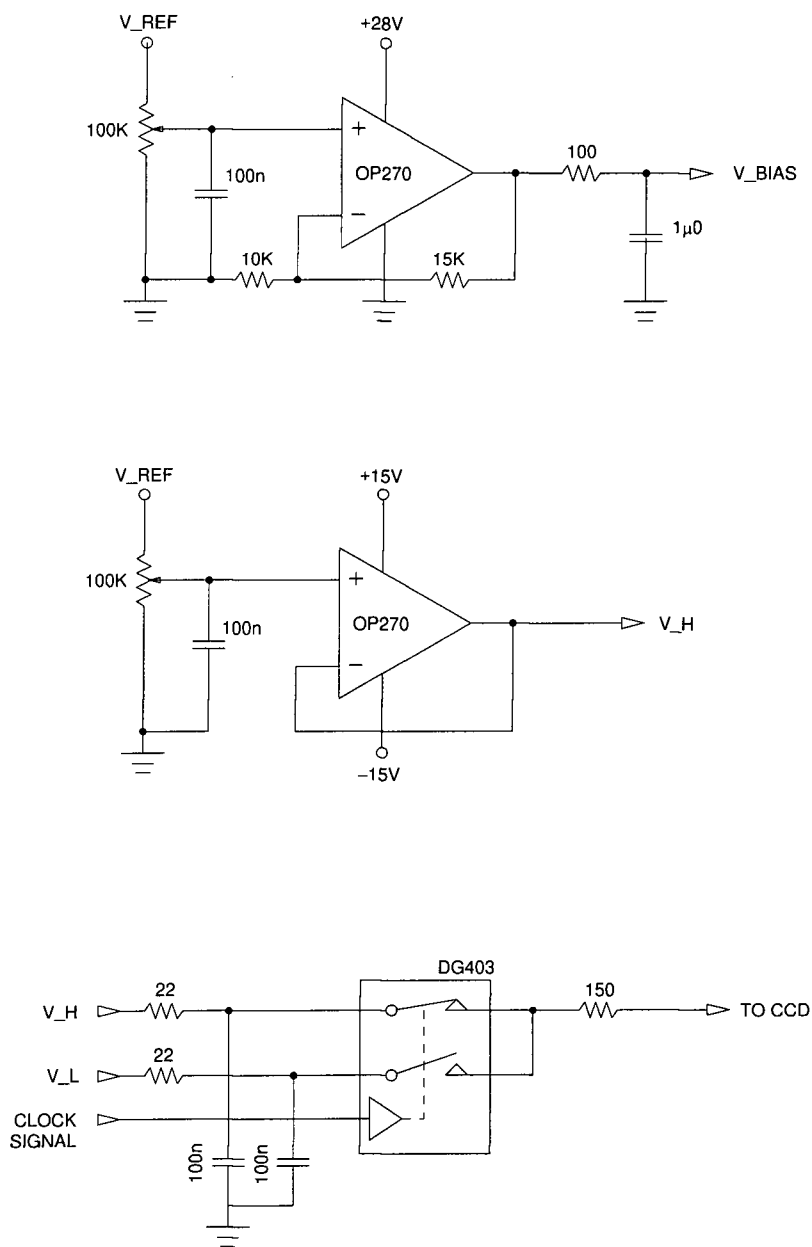
Figure 2.7: Clock driver and voltage reference circuit topology. The clock driver is based upon an analog switch. The voltage references are derived from op-amp buffers. The input signal is at CMOS logic levels. The output voltage swings between V_H and V_L, with a typical switching time of less than 150 ns. Each voltage reference can supply 50 mA with less than 20 mV peak-peak noise.

clock drivers, and the serial clock drivers to avoid crosstalk through the power supply lines. The input to each unity gain buffer amp is an adjustable voltage divider derived from a stable reference. Separate positive and negative references are provided. Similar voltage reference circuits are use to produce the bias levels [RD, OD, OW] required by the CCD.

Two preamplifiers provide voltage gain and buffer the signal to be sent to the dual slope integrators. The circuit topology of each preamplifier is shown in Figure 2.8. The CCD serial register output FET drives a 15 kΩ resistor which is capacitively coupled to a low noise, wide bandwidth OPA627 op-amp. Each signal is amplified by a factor of 25 and sent out of the dewar with an associated ground reference.

For the preamplifiers, the input voltage noise density is less than 4.5 nV/$\sqrt{\text{Hz}}$, while the input current noise density is less than 2.5 fA/$\sqrt{\text{Hz}}$, as listed in the Burr-Brown data book [36]. Since the current noise density is negligible when combined with a 15 kΩ source resistance, a buffer FET to lower the source impedance is unnecessary. With a signal bandwidth of 50 kHz, the preamplifier noise contribution will be 1μV. In comparison, even for a low CCD read noise of 2.5e$^-$, a CCD FET output with a gain of 1.5 μV/e$^-$ will produce thermal noise of 4 μV.

Each preamplifier output and associated ground reference signal are sent differentially into a dual slope integrator which performs the correlated double sampling (CDS) operation. As shown in Figure 2.8, the circuit configuration is that of a differential amplifier with offset adjustment and switchable input polarity, followed by an op-amp integrator. Analog switches configure the input differential signal. The integrator RC time constant is set by a 5 kΩ resistor and 1.5 nF capacitor to match the 8 μs integration times. The integrator storage capacitor is a low leakage polystyrene type. At the output of the integrator, a buffer op-amp introduces a variable voltage offset and provides a low-impedance source for the analog to digital converter. The A/D digital outputs are

buffered by four 8-bit registers so that any DSP data bus noise does not corrupt the conversion process.

The op-amps of the dual slope integrator signal chain (also OPA627) were chosen for their low noise and fast settling times. These are essential in order to obtain true 16 bit data from the A/D converter. The A/D converter chosen is a monolithic chip, calibrated for 16 bit linearity, with an internal sample-and-hold circuit [37]. The sample and hold tracks the buffer op-amp output during the dual-slope integration and samples the stable signal at the end of the process. The data conversion is pipelined – that is, the A/D conversion is started at the end of each pixel period with result becoming available during the next pixel period. Using a two-pass flash technique, the conversion time is 5.6 μs, which is more than adequate for the 50 kpix/s readout rate (20 μs per pixel) planned for the controller and allows some future flexibility for speeding up the controller by doubling the pixel rate.

Physically, the preamplifiers are located inside the CCD vacuum housing. The clock drivers and voltage references are located on two identical boards only inches away. Two channels of analog signal processing occupy one VME sized board, and are located a few feet away. The digital signal processor, address decoder circuitry, differential line drivers and serial interface make up a second VME sized board in the card cage.

Power for the entire wavefront sensor is supplied by linear power supplies at $+28$ volts, ± 15 volts, and $+5$ volts.

2.5 Timing and Operation.

Software downloaded from the host computer configures the DSP controller to do many standard CCD functions such as (a) frame transfer of the image pixels to the storage array, (b) parallel shift forward or backward, (c) multiple parallel shifts for vertical

Figure 2.8: Signal processing circuit topology. The preamplifier is based on a low-noise OPA627 op-amp and provides a gain of 25. The dual slope integrator circuit acts as a bandpass filter to suppress the 1/f noise of the CCD output MOSFET transistor amplifier, and the reset noise of the CCD.

binning, (d) serial shift and read, (e) multiple serial shifts and read for serial register binning, (f) flush pixel, (g) multiple flushes for line or array clearing. Readout of the CCD array is accomplished with an ensemble of these building block functions.

The operation of the CCD controller is set up by the host computer, which downloads the basic program and sequence fragments into the DSP. Additional data loaded into the DSP specify the size of the array, the horizontal and vertical binning and the sequence of operations. For each operation, the DSP accesses the sequence fragment and steps though it using the associated timing information. Elementary operations such as a single pixel read or a parallel shift are repeated to read an entire line or to perform a frame transfer. The DSP executes the specified operations on a frame by frame basis, and can return data to the host computer via a fast SBUS serial interface at up to 10 Mbps. No external memory buffer is required, as the device driver software writes the data directly to the kernel memory of the Sparcstation.

By specifying the appropriate sequence fragments, the CCD can be read out through one or both output amplifiers at either end of the serial register. The CCD can be read out as 64×64 (with frame transfer) or as 64×128 pixels. By specifying the hold time for each data word, the host software configures the parallel and serial clock rates, and the overall frame rate. The versatility of the controller allows the CCD to be read in many different ways, with programmable binning, clock rates, frame transfer, and multiple output amplifiers.

For the small frame transfer CCD, the elementary sequencing operations are shown in Figure 2.5. The timing is set so that the serial transfers occur in between the integration periods of the dual slope integrator. This is necessary since there is no on-chip summing well. The advantage of sequencing the CCD in this way is that it allows a large number of pixels to be binned before read out while minimizing the danger of saturation on-chip. For the proposed variable binning technique, this is essential.

For operation as a curvature sensor, an additional list detailing the sequence of operations to read the array into subapertures is downloaded into the DSP. The superpixel list details the parallel transfers, the serial register binning per superpixel, and the subaperture to which the superpixel data is added. Each image from the sensor involves processing the list one time. For the 13-element sensor pattern of Figure 2.2, the list has 96 elements.

Normal operation of the CCD involves a readout rate of 20 μs per pixel, with dual-slope integration times of 8 μs. A single three-phase parallel transfer requires 2.5 μs, while a single serial transfer takes 1.2 μs. Readout involves both output amplifiers from the serial register on the storage side of the array. For a 16×16 image, the readout time is approximately 2.5 ms. For a 19 subaperture image, the readout time is 2.0 ms. With frame transfer, the device can be read out at a rate approaching 500 frames per second. If necessary, the readout could be configured for 10 μs per pixel, effectively doubling the frame rate.

The fastest clock sequencing is required during frame transfer. Note that this is a very repetitive operation, generated by stepping through a few sequence fragments in a do–loop. The limitation on clock rate is the clock driver propagation delay and rise/fall time. On the CCD, the rate of parallel transfer clocking is limited by the capacitance per pixel and the number of pixels per row. Since the array is only 64×64 pixels, fast transfer with parallel clock phases of 250 ns is feasible (frame transfer in less than 100 μs).

With a typical integration time of 5 ms, and frame transfer time of 100 μs, the resulting on-target duty cycle is about 98%. Streaking during frame transfer (with no shutter) is kept to a minimum. Without frame transfer, a fast readout of the CCD at 5 Mpix/s would be required to maintain the same integration time and duty cycle, which would compromise low noise performance.

From bias and flat frames, the properties of the CCD were determined by plotting
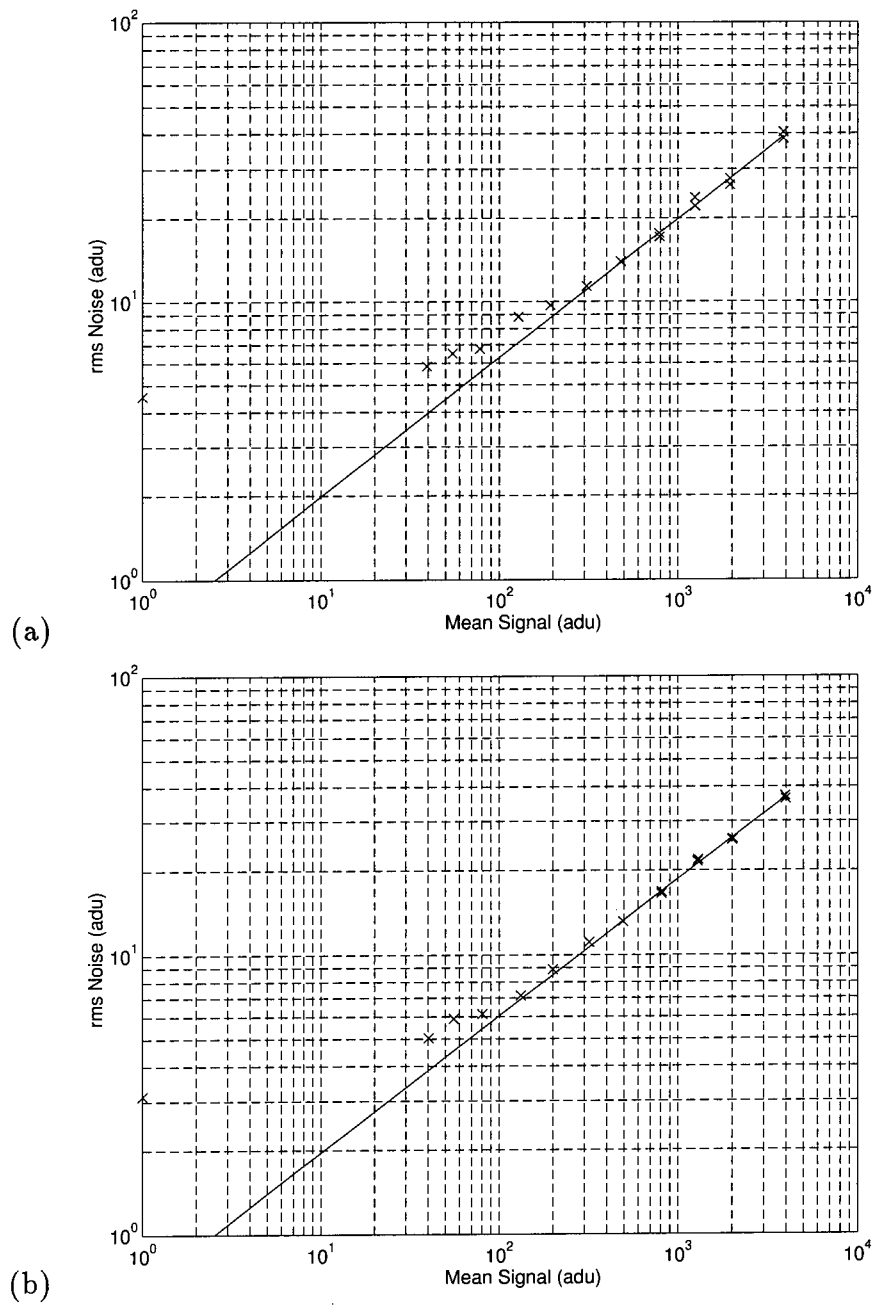
(a)

(b)

Figure 2.9: Photon transfer curves for the two CCD output amplifiers. At low signal levels, the plot shows the CCD output amplifier read noise. The intercept of the solid line shows the signal processing gain is 2.5 e⁻ per adu.

the photon transfer curve, using the method described by Janesick [38]. With a series of exposures of a uniformly illuminated CCD over a wide range of signal levels, the CCD read noise and signal processing gain can be determined by plotting the standard deviation of the signal versus the average signal (per pixel). The photon transfer curves for the wavefront sensor are shown in Figure 2.9. At high signal levels, shot noise dominates to give a slope of 0.5. At low signal levels, the minimum device read noise is revealed. The intercept of a slope 0.5 line with the signal axis gives the gain in e^-/adu. At each illumination level, the signal level per pixel is determined after the offset and dark current are subtracted from the raw data. The standard deviation is determined from the difference of two images (to account for the pixel to pixel non-uniformities) and then divided by $\sqrt{2}$. For these tests, the CCD was cooled and read out as a 64×64 array. The two output amplifiers show slightly different read noise levels of $8e^-$ and $10e^-$, with $2.5e^-$ per adu gain.

2.6 Extracting the curvature signal.

The CCD curvature sensor operates by sampling the defocused guide star image into an annular pattern of subapertures. Sample patterns are shown in Figure 2.2 for a 32×32 grid. The dotted line represents the outline of the spot produced by the defocused beam. The illuminated area of each subaperture is roughly equal to minimize the variation in signal-to-noise ratio over the pattern. Note that the center spot of the pattern will be partially covered by the shadow of the telescope secondary mirror.

Since the annular patterns of the subapertures do not fit exactly onto the grid of the CCD, some spatial quantization error will result. Comparing the area of the summed pixels to the area of each subaperture, a first order estimate of the spatial quantization error on a 32×32 grid is approximately 3%. Sampling on a coarser grid introduces several

times larger error, while a finer grid involves many more pixels which would compromise the sensor frame rate.

After the image is acquired, the DSP is required to process the subaperture data to extract the curvature signal. The subapertures have different responsivity, bias level, and dark current according to the number of pixels in each, which must be compensated before the curvature signal is computed.

Flat fielding involves only a deterministic scale factor to compensate for the different subaperture areas, and the different gains of the two output amplifiers. With the large number of pixels of the 64×64 array making up each subaperture, the individual pixel to pixel variations are effectively averaged out as these are summed to form the subapertures. Trials show that the rms variation between subapertures of the same area which share the same output amplifier is less than 1%.

To minimize the number of divide operations, which consume many processor cycles, each subaperture signal is scaled so that all the curvature calculations use the same normalization factor. The scaling factor is based on the geometric area (and output amplifier gain) and gives the equivalent signal for the full aperture. For example, a subaperture with 1/20th of the total area would be scaled by a factor of 20. This approach avoids calculating a different normalization factor for each subaperture.

To compensate for the differing bias levels and dark counts, a dark frame is acquired at the beginning of the session using the subaperture readout technique. When required, the dark frame can be reacquired to account for temperature changes or drift in the CCD or signal processing gain.

For each subaperture, the curvature signal is derived from the following formula

$$\frac{\Delta I}{I} = \frac{G \cdot (I - I_B) - I_S}{I_S} \tag{2.1}$$

where I is the subaperture data, I_B is the subaperture dark signal, $I_S = \Sigma(I - I_B)$ is

the bias corrected sum of the subapertures from the bias and image frames, and G is the geometric scaling factor.

After each integration, readout of the CCD gives the raw subaperture data. The bias signal is subtracted off, and the subaperture signal is scaled by the geometric factor G. The subaperture sum I_S and the normalization factor I_S^{-1} are computed. Finally, the curvature signal per subaperture is calculated as per Equation 2.1. Once the CCD readout is complete, the processor takes less than 20 μs to derive curvatures for all subapertures.

Chapter 3

Membrane mirror and driver electronics

3.1 Introduction and Background.

The adaptive mirror for the CHRISP system is an electrostatically deformable membrane mirror. It has the potential for low order wavefront correction, with a simple structure, few moving parts, and low actuator voltages.

At least two different approaches to the design of a membrane mirror have been researched. Grosso and Yellin [39] pioneered a design with a titanium membrane suspended between an actuator array, and a transparent electrode on the inside surface of the entrance window. The unit operated at low pressure, with high membrane tension giving a mechanical bandwidth of better than 1 kHz for a 50 mm membrane. Precise machining and assembly capabilities were necessary to build one of these mirrors, as the spacing between the membrane and electrodes was less than 100 μm. Centamore and Wirth [21] investigated a simplified alterative with no entrance window. A high voltage asymmetric bias allowed machining tolerances to relax, and simplified the design. The high bias membrane mirror used a 50 mm MYLAR membrane, with lower membrane tension, and operated at atmospheric pressure. A novel aspect of this design was the parabolic static shape given to the membrane by the bias arrangement.

For this project, I have designed and built a prototype unit [23] which attempts to improve on the design of Centamore and Wirth by adding an entrance window to reduce the sensitivity to vibration, by simplifying the high voltage and actuator electronics, and by using a higher surface quality 100 mm nitrocellulose membrane. One further goal

was to pursue the membrane mirror concept as an alternative to solid actuator mirrors such as bimorphs [40] for curvature sensing adaptive optics. The prototype is shown in Figure 3.1.

The simplest membrane mirror configuration involves a reflecting membrane stretched onto a tension ring, and suspended above an actuator electrode array. The membrane is biased to a high voltage, with respect to the electrode array. At each actuator, an applied signal voltage sets up a local electrostatic pressure which causes the membrane to deform. Increasing the local membrane-actuator potential causes the membrane to deflect toward the actuator array. Membrane tension provides the restoring force.

Deformation of the membrane surface is described by the Poisson equation [39]. For the condition in which the membrane is biased to voltage V_0 with an applied small signal voltage ΔV, (ie $V = V_0 + \Delta V$) the curvature of the surface is approximated by

$$\nabla^2 z = \frac{\epsilon_0}{T \ell_0^2} \cdot (V_0^2 + 2V_0 \Delta V) \tag{3.1}$$

where T is the tension per unit length $(\mathrm{Nm^{-1}})$, and ℓ_0 is the membrane to electrode spacing (m). Note that there is a static bias voltage component and a dynamic signal dependent component to the curvature relation. In the adaptive optics system, the static component must be accounted for in the optical design, while the dynamic component is exploited for curvature correction.

3.2 Prototype deformable membrane mirror.

Figure 3.2 shows the structure of the prototype membrane mirror I have designed and built. Overall specifications are listed in Table 3.1. The reflecting surface is an aluminized nitrocellulose membrane, 100 mm in diameter by 2.5 μm thick, stretched flat and bonded to an aluminum tension ring. Spacers arranged in a three point support system suspend the membrane approximately 400 μm above the electrode array.
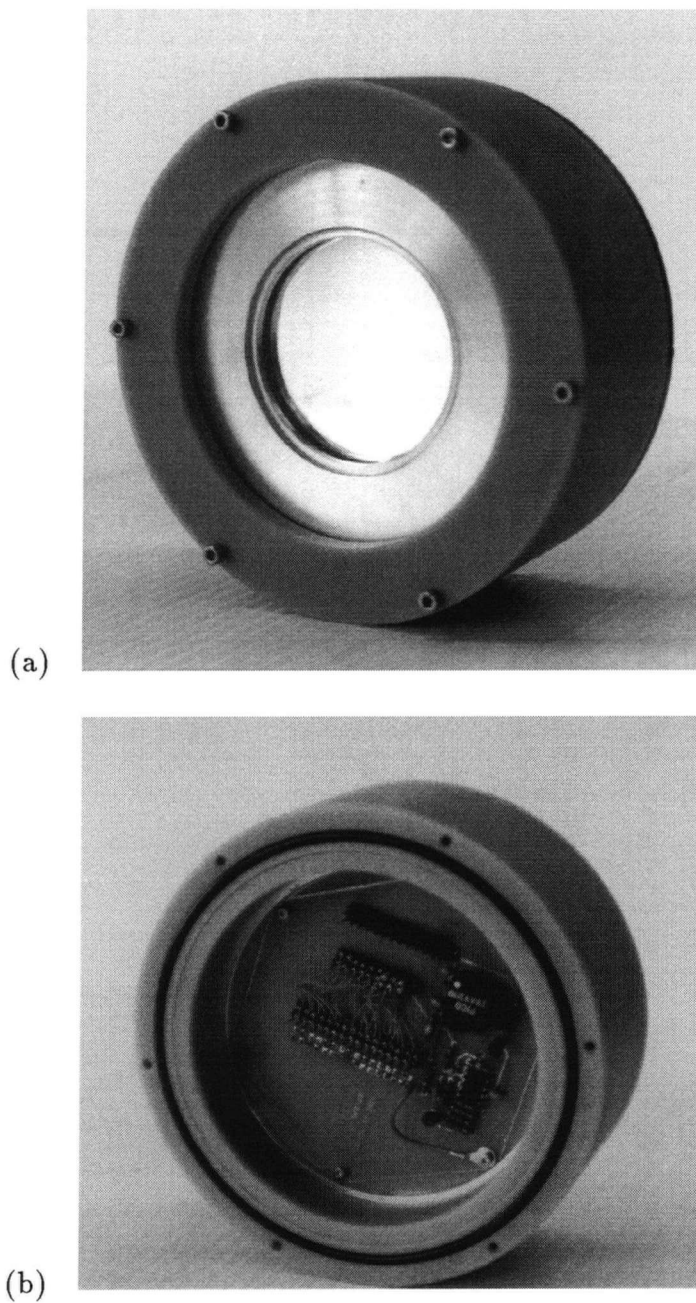
(a)

(b)

Figure 3.1: Photographs of the membrane mirror show the simple structure of the device. (a) the reflecting surface is visible through the entrance window (b) the bias electronics (which generate up to 300 volts) are contained within the mirror housing to minimize any hazard.
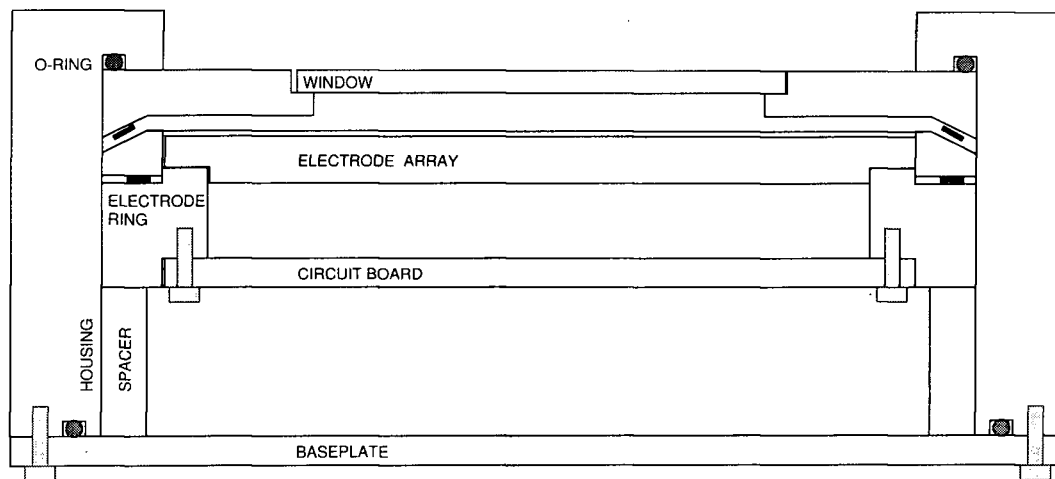
Figure 3.2: Membrane mirror structure. The 100 mm diameter membrane is suspended 390 μm above the electrode array by a three point spacer arrangement. A second set of spacers supports the entrance window. Overall the mirror is 14 cm diameter by 6cm deep.

The electrode array consists of 31 actuators, arranged concentrically on a machined MACOR ceramic substrate. Connecting wires are bonded with conductive epoxy into holes drilled in the ceramic, which is then polished flat. The electrode pattern is formed by evaporating aluminum onto the front surface through a mask. The actuator pattern, shown in Figure 3.3 is designed to closely correspond to the wavefront sensor zonal pattern.

The high voltage bias and driver amplifiers share a simple, low parts count circuit topology, as shown in Figure 3.4. The op-amp provides the high open loop voltage gain necessary for a linear transfer function, low voltage offset and low output ripple, while the bipolar transistor generates the level-shifted high voltage output. Specifications for the electronics are listed in Table 3.2.

Each amplifier input is designed to be driven directly from an 8-bit D/A converter
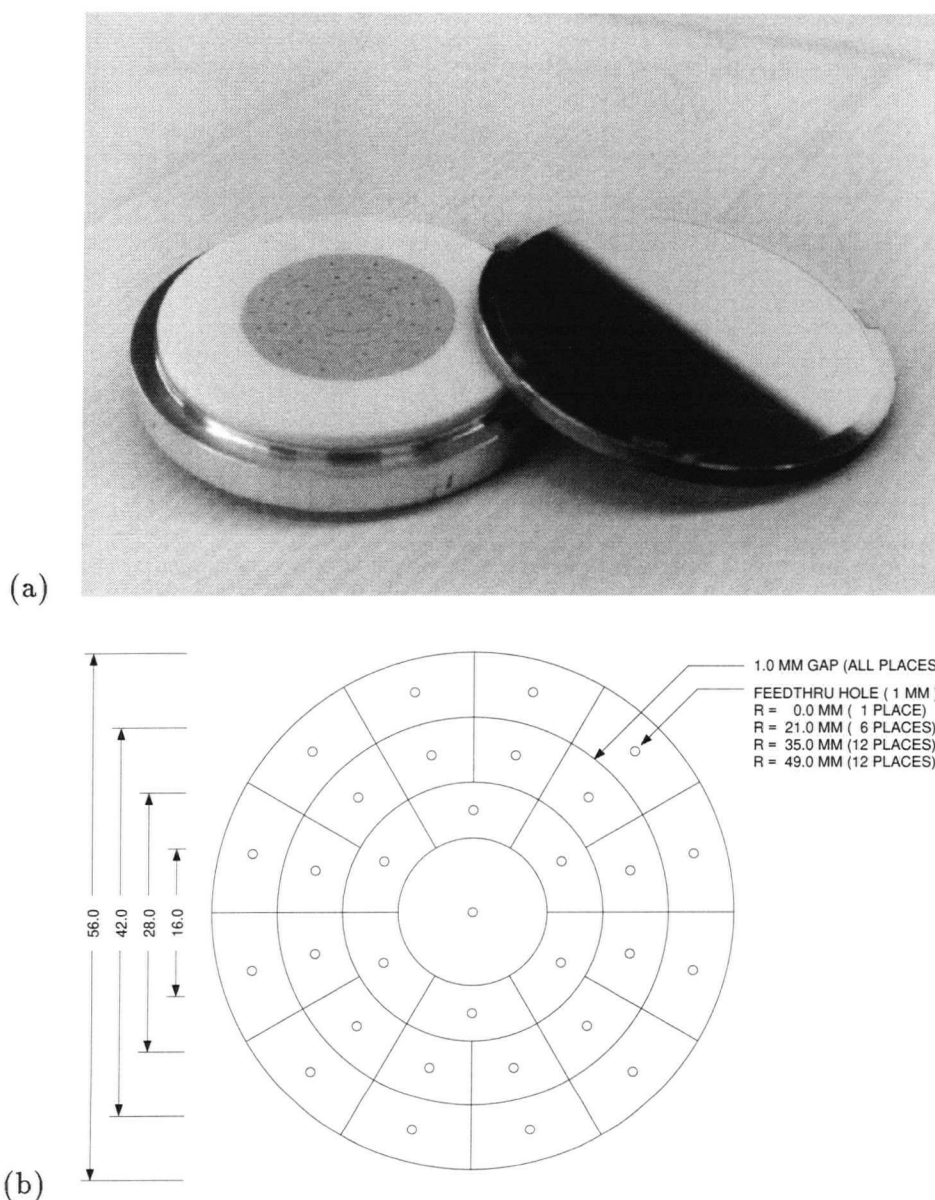
(a)

(b)

1.0 MM GAP (ALL PLACES)

FEEDTHRU HOLE (1 MM)
R =   0.0 MM (1 PLACE)
R = 21.0 MM (6 PLACES)
R = 35.0 MM (12 PLACES)
R = 49.0 MM (12 PLACES)

56.0 42.0 28.0 16.0

Figure 3.3: (a)Photo and (b) schematic of the electrode array. The electrode array consists of 31 actuators, arranged concentrically on a machined MACOR ceramic substrate. The beam diameter on the mirror is 42 mm. The reflecting surface is an aluminized nitrocellulose membrane, 100 mm in diameter by 2.5 μm thick, stretched flat and bonded to an aluminum tension ring.
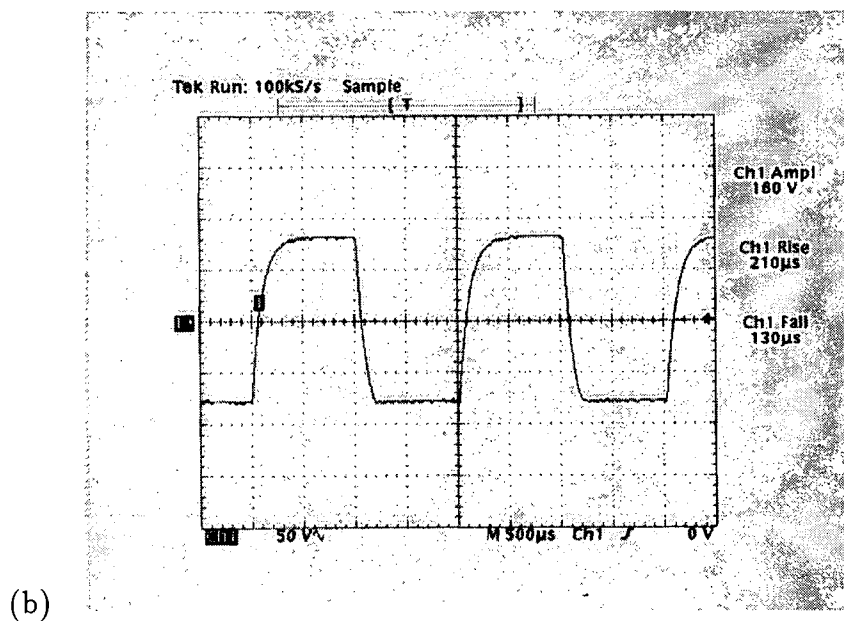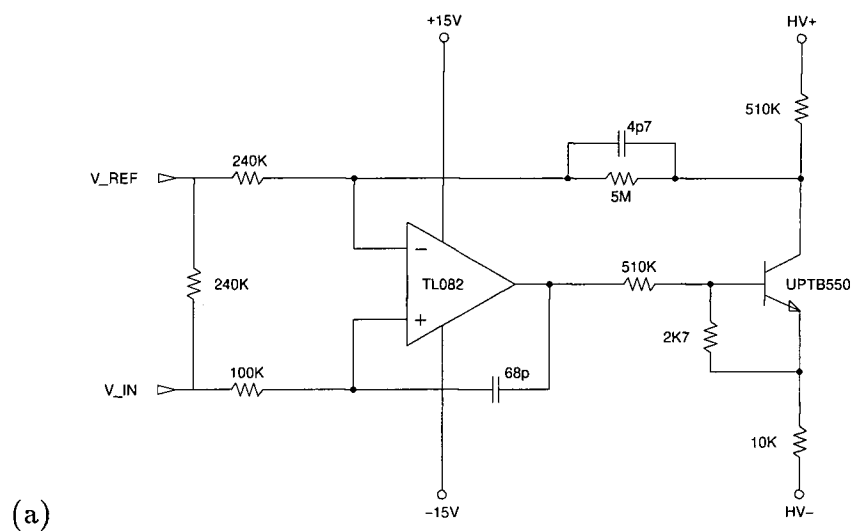
(a)

(b)

Figure 3.4: (a) Circuit schematic and (b) large signal pulse response for the high voltage bias amplifier and actuator driver amplifier. The slew rate of the amplifiers is about $0.8\ \mathrm{V}\mu\mathrm{s}^{-1}$.

Table 3.1: Membrane mirror specifications.

Membrane mirror specifications		
Membrane diameter	100	mm
Actuated area diameter	56	mm
Beam diameter	42	mm
Membrane tension	50	Nm^{-1}
Spacing	250	μm
Thickness	2.5	μm
Number of actuators	31	
Nominal bias voltage	250	volts
Actuator signal voltage	± 80	volts
Nominal actuator capacitance	20	pF
Operating pressure	1	atm
Tip/tilt dynamic range	± 30	arcsec
Local deflection range	± 3.0	μm
Tip/tilt step response [a]	10	ms
Equivalent mechanical bandwidth	35	Hz

a. measured 10% to 90% with ± 20arcsec step

with a 0 to 10 volt output signal. The complementary V_{REF} input selects the unipolar/bipolar voltage range of the amplifier. The op-amp drives a high voltage transistor which generates the output. The $R_F C_F$ feedback network configures the amplifier as a low-pass filter, with an overall voltage gain of approximately 20 and small-signal bandwidth of DC to 5 kHz.

Power is supplied from miniature switching voltage converters. With a nominal transistor bias current of 200 μA, each amplifier consumes 50 mW. The circuit is designed to have a high output impedance (500 kΩ) for short-circuit protection of the membrane. The high voltage bias electronics (which generate up to 300 volts) are contained within the mirror housing to minimize any hazard.

An entrance window seals the housing to isolate the reflecting surface from air-coupled

Table 3.2: Electronics specifications.

Electronics specifications		
Input voltage	0 to 10	volts
Output voltage (HV bias amp)	50 to 280	volts
Output voltage (actuator driver)	-80 to +80	volts
Gain (HV bias amp)	40	V/V
Gain (actuator driver)	20	V/V
Output voltage ripple	35	mV rms
Offset voltage	100	mV
Linearity	.5	%
Power consumption	50	mW
Nominal bias voltage	250	volts
Actuator signal voltage	±80	volts
Bandwidth (small signal)	5	kHz
Rise time (large signal)	200	μs
Slew rate	0.8	$V\mu s^{-1}$
Output impedance	500	kΩ
Input impedance	10	kΩ

vibration, as well as to protect the membrane, and to prevent humidity related changes in the membrane tension. The unit itself operates at atmospheric pressure. The window should be anti-reflection coated to minimize any optical losses.

Although I did not attempt this, it would be possible to modify the design slightly to accommodate a window with a transparent indium-tin-oxide electrode so that the membrane is symmetrically biased, as described by Grosso & Yellin [39]. With the bias voltage applied to the membrane and the window electrode grounded, the electrode array and actuator amplifiers remain unchanged. In the symmetrically biased window design, the membrane static shape is flat while the asymmetric bias arrangement gives the membrane a parabolic shape. Deflection of the mirror from its static shape for any given applied voltage is the same as before. But, the window electrode would compromise

the design by adding optical loss and reducing the useful wavelength range of the unit.

3.3 Performance estimates.

For a circularly symmetric membrane, the Poisson equation can be directly integrated with the appropriate boundary conditions. The resulting design equations for the mirror describe the static deflection $z_s(r)$, the focal length f within the actuated area, the curvature voltage sensitivity $\nabla^2 z/\Delta V$, and the deflection voltage sensitivity $\Delta z_p/\Delta V$

$$z_s(r) = \begin{cases} \frac{\epsilon_0 V_0^2}{4T\ell_0^2}\left\{ r^2 - r_a^2\left[1 - 2\ln\left(\frac{r_a}{r_f}\right)\right]\right\} & 0 < r < r_a \\[2ex] \frac{\epsilon_0 V_0^2}{2T\ell_0^2}r_a^2\ln\left(\frac{r}{r_f}\right) & r_a < r < r_f \end{cases} \tag{3.2}$$

$$f = \frac{T\ell_0^2}{\epsilon_0 V_0^2} \tag{3.3}$$

$$\frac{\nabla^2 z}{\Delta V} = \frac{2\epsilon_0 V_0}{T\ell_0^2} \tag{3.4}$$

$$\frac{\Delta z_p}{\Delta V} = \frac{\epsilon_0 V_0}{2T\ell_0^2}r_p^2\left[1 - 2\ln\left(\frac{r_p}{r_f}\right)\right] \tag{3.5}$$

with support ring radius r_f, actuated area radius r_a, and central actuator radius r_p. Note that for small ΔV, both the curvature and deflection are linear with bias voltage V_0 and inversely proportional to tension T and spacing ℓ_0. Within the actuated area, the static component of the curvature gives the membrane a weakly parabolic figure. These equations are derived in Appendix E.

With these equations, it is possible to explore the basic design requirements and tradeoffs involving membrane diameter, tension, membrane–electrode spacing, actuator size and bias voltage. To ensure the maximum dynamic range for the mirror deflection, a high voltage bias, low tension and minimal spacing are preferred to increase the curvature and deflection sensitivity. However, the membrane tension must be high enough to ensure

a reasonable mechanical bandwidth. The membrane to electrode gap must be at least a few hundred microns to avoid assembly and machining difficulties. In addition, the static deflection of the membrane must be a small fraction of the gap so that each actuator has the same voltage sensitivity. High bias voltage and large signal voltages increase the mirror dynamic range, but at the expense of more complex electronics.

Figure 3.5 illustrates a range of reasonable parameters for the prototype unit. The membrane size is 100 mm with an estimated tension (fixed by the manufacturer) of 50 Nm^{-1}. The actuated area is roughly half the membrane diameter, with 19 central electrodes and 12 boundary electrodes arranged concentrically. For a spacing of $\ell_0 =$ 390 μm and a bias voltage of $V_0 = 250$ volts, the curvature sensitivity is 0.58 V^{-1}mm^{-1}, and the deflection sensitivity is 45 nmV^{-1}.

The prototype unit has a predicted focal length of 13.5 meters, and a static deflection of 30 μm at the center. The static deflection is less than 10% of the membrane to electrode spacing, ensuring that all actuators will have essentially the same voltage sensitivity.

One can explore the deflection capability of the membrane mirror for arbitrary actuator voltage distributions by numerical solution of a system of difference equations. As described by Carnahan et al. [41], the Laplacian can be approximated as a finite difference $\nabla^2 z = h^{-2}[z_{i,j+1} + z_{i,j-1} + z_{i+1,j} + z_{i-1,j} - 4z_{i,j}]$ on an (i,j) grid with spacing h. With an equation for each interior point, and boundary value z=0 at the membrane edge, the system of simultaneous difference equations can be written as a sparse matrix and solved efficiently using Matlab. For the cases where the analytical and simulated solutions are both known, the solutions are virtually identical.

Figure 3.6 shows the expected membrane surface as the boundary actuators are configured to produce tilt. The contours are at 0.25 μm intervals, demonstrating a simulated tilt of ± 20 arcsec over the 42 mm diameter beam. With only a dozen boundary actuators, the simulation predicts that the membrane can be effectively configured to produce or
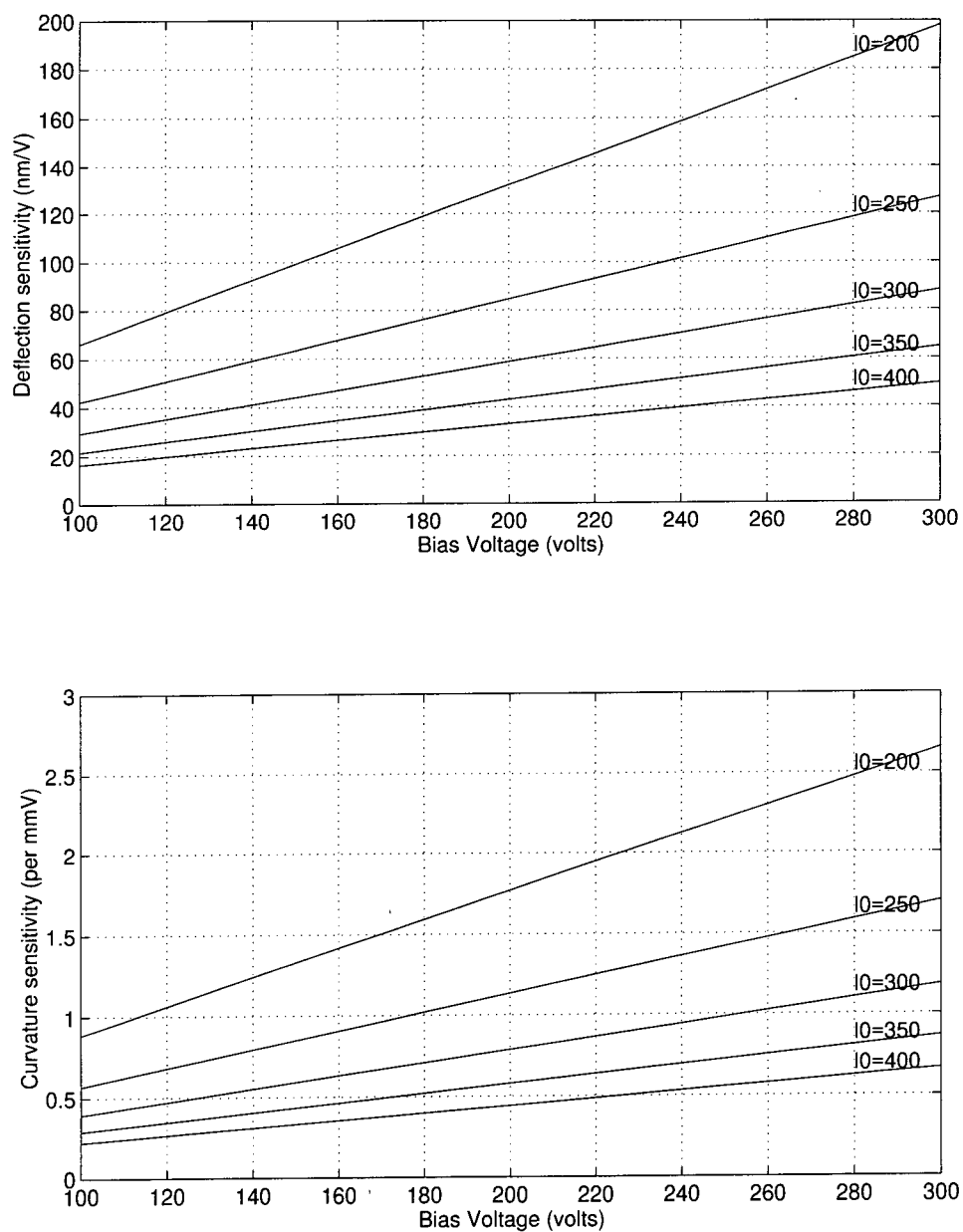
Figure 3.5: Curvature and deflection sensitivity for a range of bias voltage and membrane spacing values.

compensate for tip-tilt.

In a similar fashion, compensation of various higher order Zernike terms by the membrane mirror can be explored. In these cases, the applied voltage is computed from the Laplacian of the Zernike function within each mirror zone. The response of the mirror to a single off-axis actuator is illustrated in Figure 3.7.

3.4   Prototype test results.

Manufacture and assembly of the membrane mirror was relatively straightforward. Most of the elements were fabricated on a standard lathe to normal machining tolerances. The most difficult assembly step involved measuring and spacing the membrane to electrode gap correctly. A micrometer caliper proved to be a useful tool for this step. Except for the membrane, all of the mirror components were robust and required no special handling.

Initial optical testing of the assembly was performed with a Zygo interferometer. From static measurements at bias voltages of $V_0 = 0$, 100, and 200 volts, I was able to derive an estimate for the membrane mirror tension, using equation 3.2. Figure 3.8 shows the central region of the mirror as biased to 200 volts. For comparison purposes, the contour plot shows the parabolic shape of a numerically simulated membrane mirror with the same parameters. The interferogram shows a reflection from the entrance window, as well as a slight imperfection in the window. In later testing, we discovered that any slight irregular bending of the tension ring immediately showed up as an optical aberration.

Due to membrane microphonics, it proved impossible to obtain a separate optical measurement of the membrane outside the housing to assess the initial optical quality of the membrane.
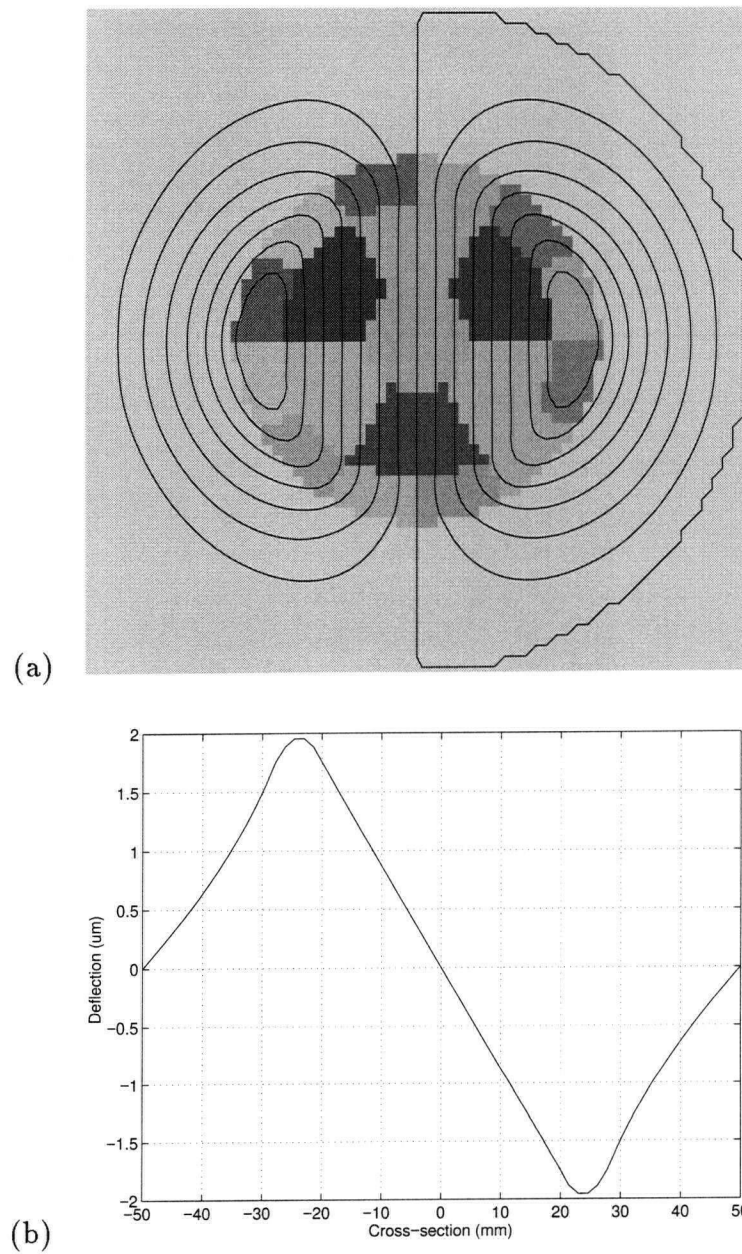
(a)

(b)

Figure 3.6: Tilt simulation. Contours are at 0.25 μm. The static parabolic shape of the membrane has been removed. The actuator pattern has been superimposed for reference. Tilt actuator voltages are applied to the outer electrode ring only.
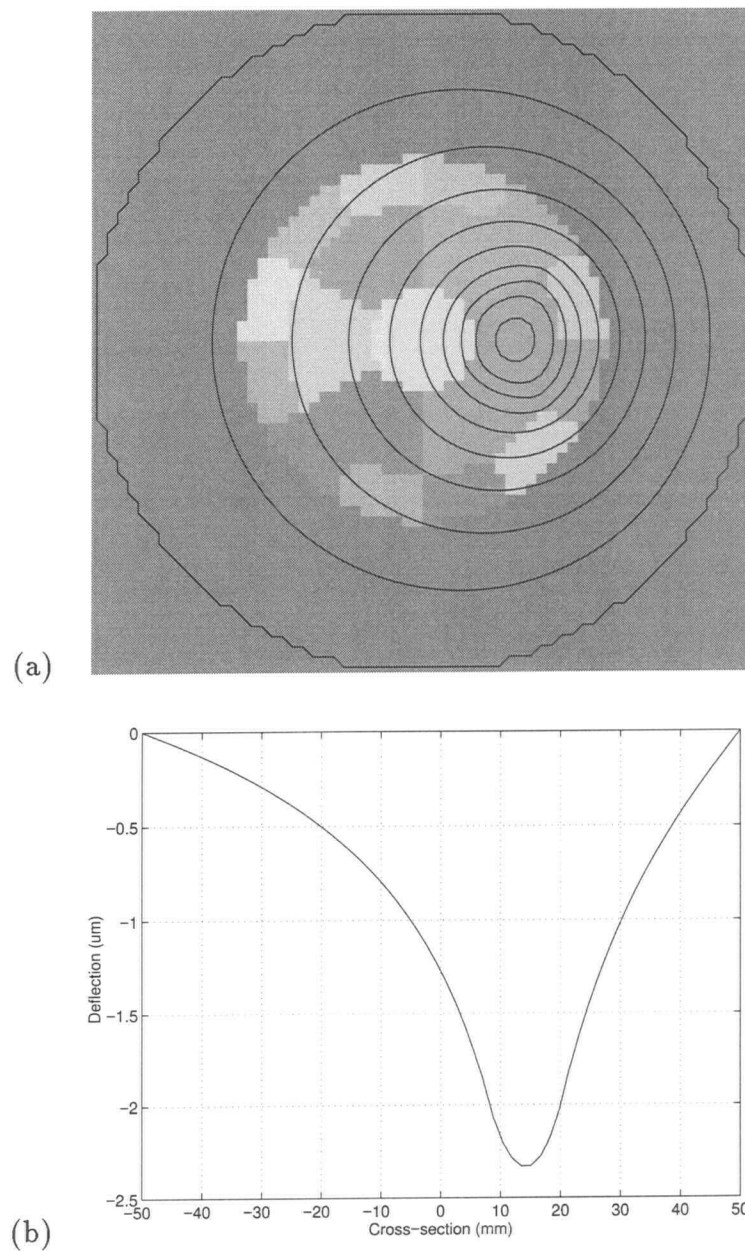
(a)

(b)

Figure 3.7: Off-axis actuator response. The image and profile for an off-axis actuator voltage of 50 V. The contour lines are 0.25 μm apart. The electrode array pattern is shown for reference.
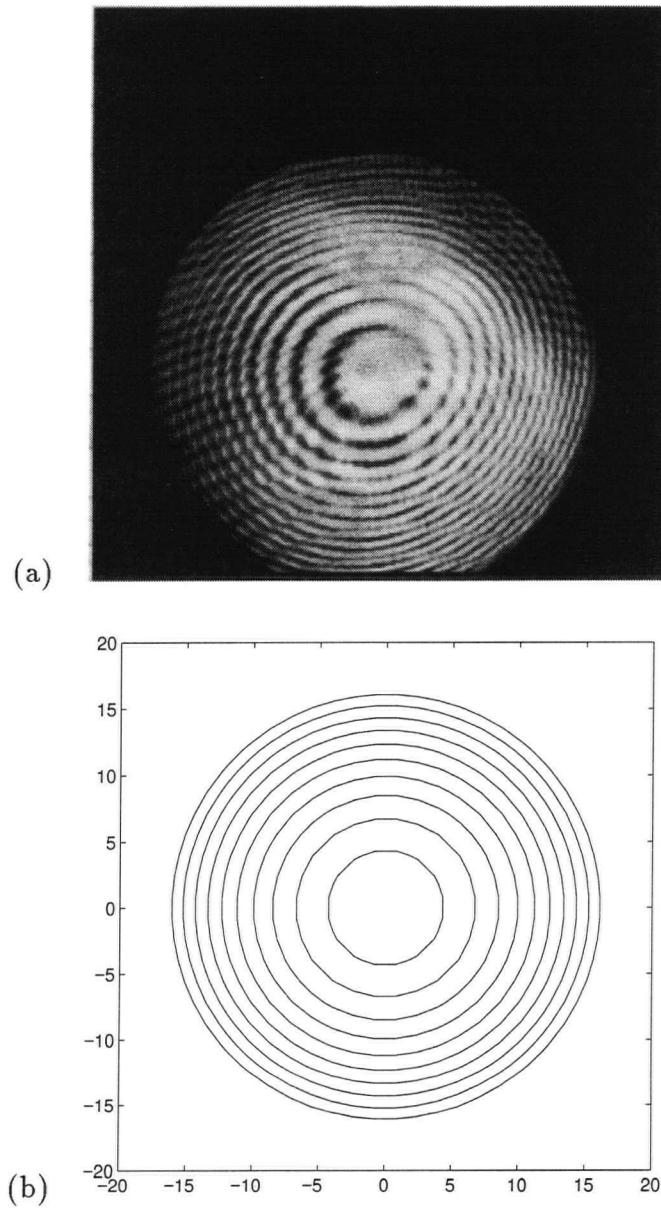
Figure 3.8: (a) the membrane surface as measured with a Zygo interferometer at bias voltage $V_0 = 200$ volts. The slight asymmetry and reflection are due to the entrance window. (b) numerically simulated contour plot of the membrane surface for $\ell_0 = 250$ μm, $T = 120$ Nm^{-1}, and $V_0 = 200$ volts.

Over the course of the experiment, we discovered that the initial membrane had apparently aged – that is, the nitrocellulose had stretched, reducing the membrane tension. The required bias voltage dropped from 200 volts to about 150 volts to accommodate the reduced tension. Worse still, the mirror surface had acquired a permanent defect, so that the images produced by the optical system with the mirror in place showed a pronounced astigmatism. It is possible this was due to being stored with some uneven stress on the membrane tension ring.

Despite numerous attempts over a period of several months, I was not able to equalize the membrane tension and reduce the aberration. None of the strategies I tried were reliable, including (1) adjusting the relative heights of the three membrane spacers, (2) adding a fourth membrane spacer to put differential stress on the tension ring, or (3)offsetting the positions of the three window spacers with respect to the membrane spacers. Eventually, the membrane had to be replaced.

Dynamic testing of the mirror was performed with the replacement membrane. But, even with the replacement membrane, the design of the membrane supports made it difficult to achieve a stress-free, aberration-free mounting of the membrane. Images from the optical testing show that the mirror is still being slightly pinched by the mounting arrangement of the membrane tension ring.

To measure the tip-tilt dynamic range of the mirror, I used an optical arrangement similar in design to the adaptive optics layout, as shown in Figure 3.9. Light from a HeNe laser illuminated pinhole was passed through an aperture mask to produce an f/30 beam and 42 mm beam diameter on the membrane mirror, and then focused onto the wavefront sensor CCD by a lens and folding mirror. Tilt voltages were applied to the membrane mirror boundary actuators, and the resulting displacement of the spot on the CCD was observed. The measured tip-tilt was ±20 arcsec for a maximum signal voltage of ±50 volts, confirming the simulation result. The tip-tilt response of the mirror
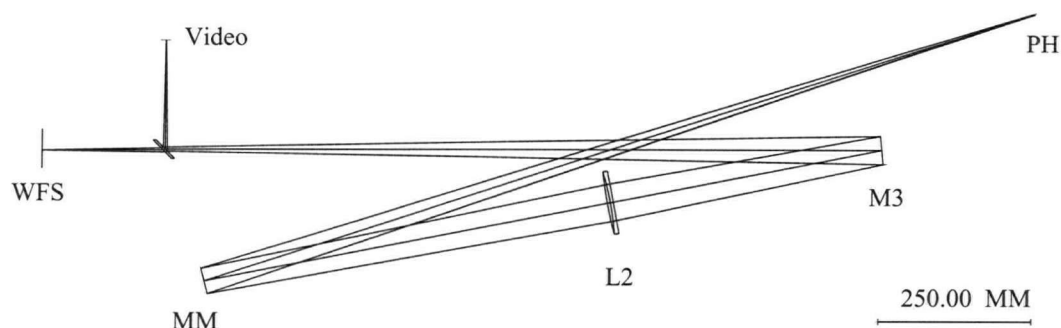
Figure 3.9: Optical arrangement used to determine tip-tilt dynamic range and step response time.
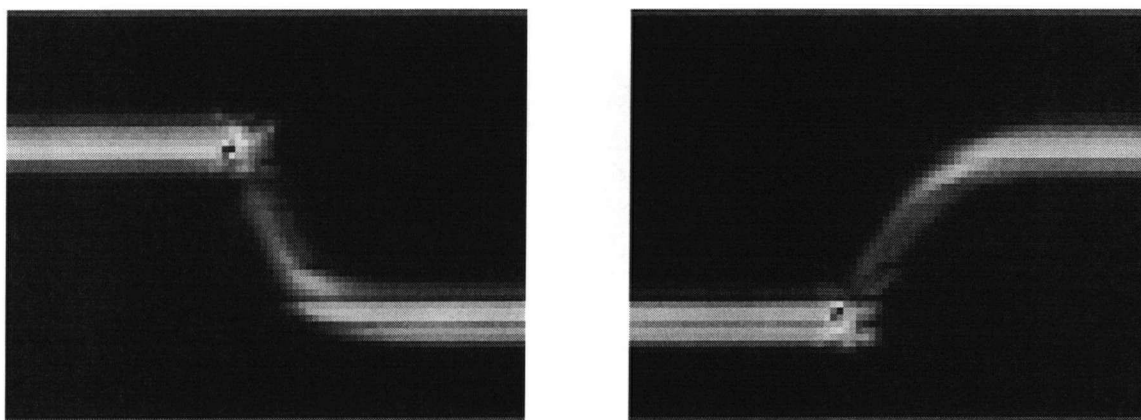

Figure 3.10: CCD streak mode images illustrating the membrane mirror tip-tilt step response. The applied tilt was ±20 arcsec and response time was approximately 10 ms. Each row of the CCD is read out in 1.25 ms.

is especially encouraging as it confirms the possibility of performing all the wavefront correction with a single adaptive mirror.

Dynamic measurements of the mirror response time were made using the same optical arrangement, with the CCD operating in a streak mode. That is, a tilt of ±20 arcsec was applied to the mirror actuators while reading out the CCD. The resulting streak image (Figure 3.10) shows the step response of the mirror for a ±50 volt signal. The response

appears to be predominantly first-order with a 10 ms rise time, or an equivalent small signal mechanical bandwidth of approximately 35 Hz. There is no appreciable overshoot and the mirror appears to be well-behaved during the transition.

Chapter 4

Optical design and system integration

4.1 Optical design.

The CHRISP optical system is designed for the coudé path of the DAO 1.2-m telescope. Figure 4.1 shows the optical layout of the system, as designed by J.Pazder [42]. In normal operation, the incoming f/145 coudé beam would be changed to f/30 by achromat L1 [f=2.0 m] and brought to a focus 2.0 meters away at the spectrograph slit. With the adaptive optics in place, L1 produces a 43 mm diameter image of the primary on the deformable mirror. Achromat L2 [f=1.0 m] reconfigures the beam to f/30 for the spectrograph. The flat folding mirrors (all $\lambda/10$) fit the system into the available space.

Each of the optical components is mounted so that its height, orientation and position can be manipulated. Figure 4.2 shows a photograph of the system set up at the telescope. Mirrors M1 and M3, and lens L2 are fastened to one large aluminum plate. Mirror M2 is positioned on an optical rail clamped to the support block for L2. The deformable mirror and beamsplitter are fastened to plates supported by a pier near the slit. All of the components are referenced to the "vibration isolated" floor of the telescope slit room. At the start of each session at the telescope, the position and orientation of the components must be set up and carefully aligned. All of the components are (nominally) in the same plane.

For a wavelength range of 800 to 900 nm, the design puts 50% of the light in 0.27 arcsec, and 80% in 0.4 arcsec [42]. The beam sizes on the various components are shown in Table 4.1 for three different sizes of field of view.
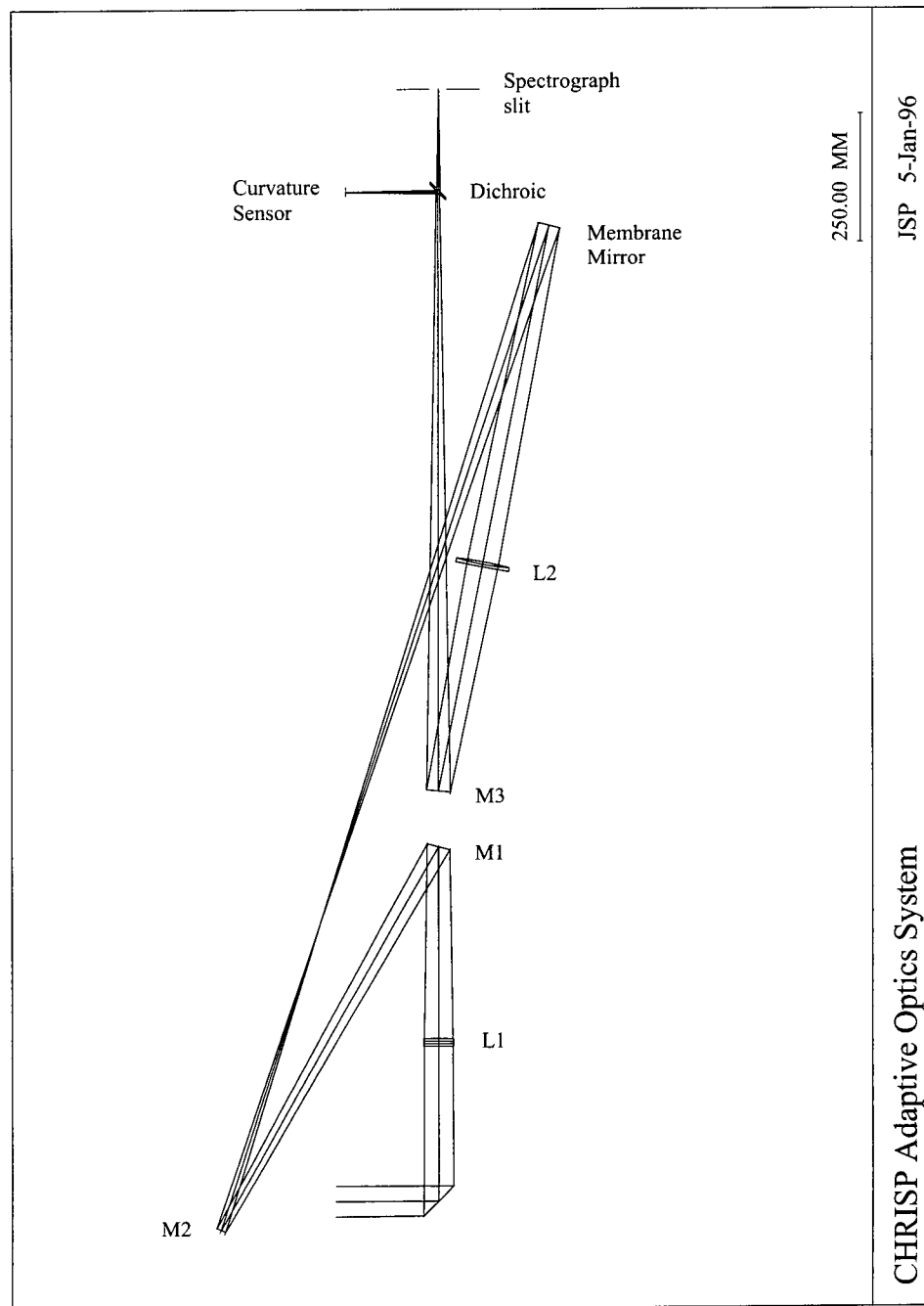
Figure 4.1: The layout of the optical components for the CHRISP system adds three flat steering mirrors (M1–M3), a lens (L2), and the deformable mirror to the optical path. A dichroic beamsplitter directs the beam to the wavefront sensor.
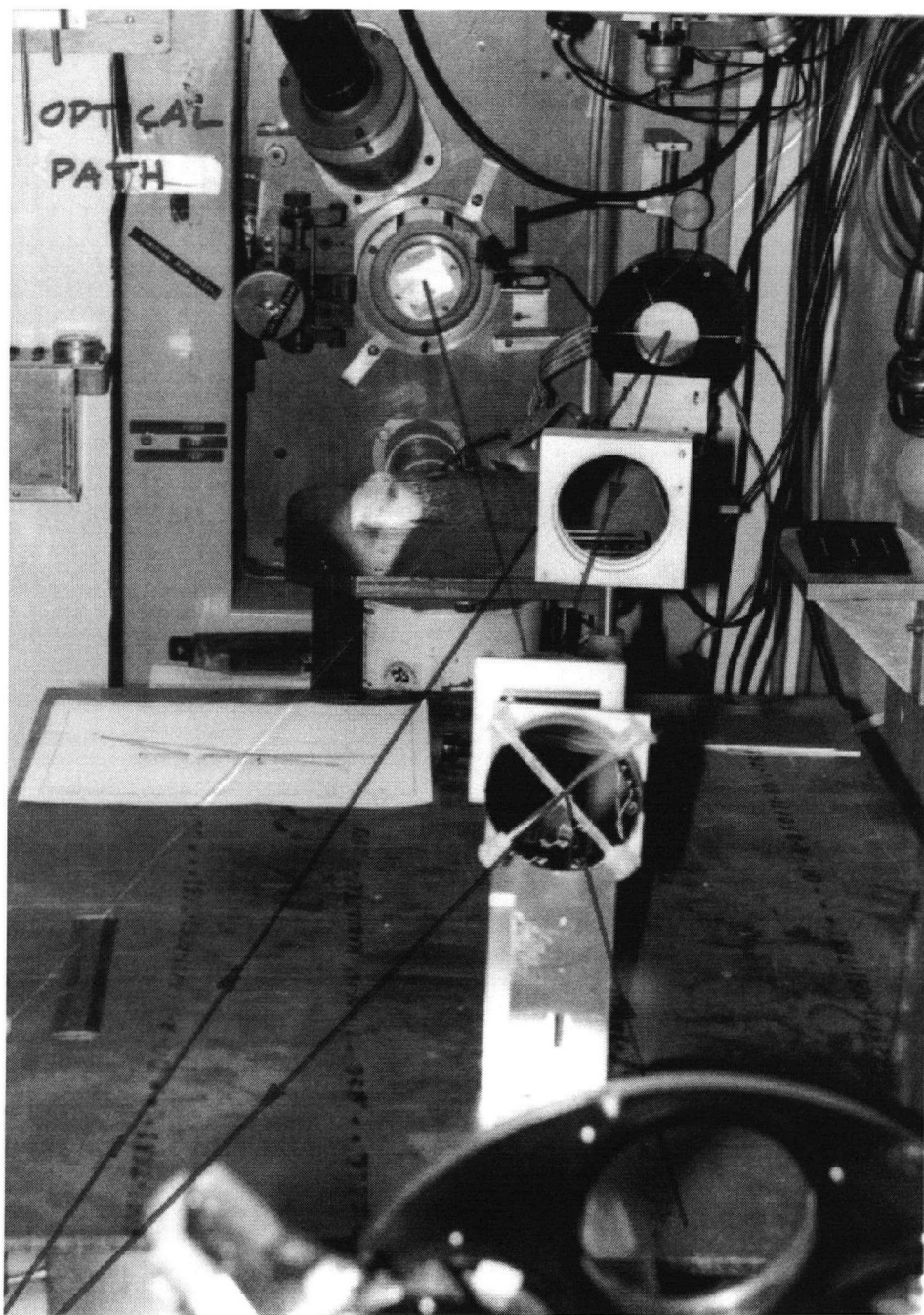
Figure 4.2: Photograph of the optical system set up in the telescope slit room. The optical path is marked on the photograph. The spectrograph slit is 2 meters from the lens turret. Mirror M2 is out of sight at the bottom-left edge of the frame.

Table 4.1: Beam size on optical components.

Component	Beam size (mm)		
	±0 arcsec	±10 arcsec	±30 arcsec
Lens L1	56	65	83
Mirror M1	46	54	71
Mirror M2	19	25	36
DM	43	43	43
Lens L2	62	64	67
Mirror M3	47	49	54
Focus	-	4	11

The simplicity of the single image curvature sensor is apparent in the layout. Only a dichroic beamsplitter is necessary to divert the beam. Wavefront sensing is done in the visible, while the near infrared is fed to the spectrograph. The wavefront sensor is mounted on a three-axis translation stage to acquire the guide star. The wavefront sensor operates at a fixed distance from the best focus.

The deformable mirror provides both tip-tilt and higher order correction. The tip-tilt dynamic range of the membrane mirror is more than ±30 arcsec, which translates to ±2.1 arcsec on the sky. Note that the plate scale is .08 arcsec/pixel, so the wavefront sensor field of view is only 5 arcsec × 5 arcsec.

With minimal changes, a beam rotator could be placed at the intermediate focus. It was not included in the original testbed configuration.

4.2 Control system.

The CHRISP control system exploits the fact that the wavefront sensor provides a curvature signal, while the membrane mirror surface curvature varies with applied voltage. The simplified servo-control system maps zones of the sensor directly to electrodes
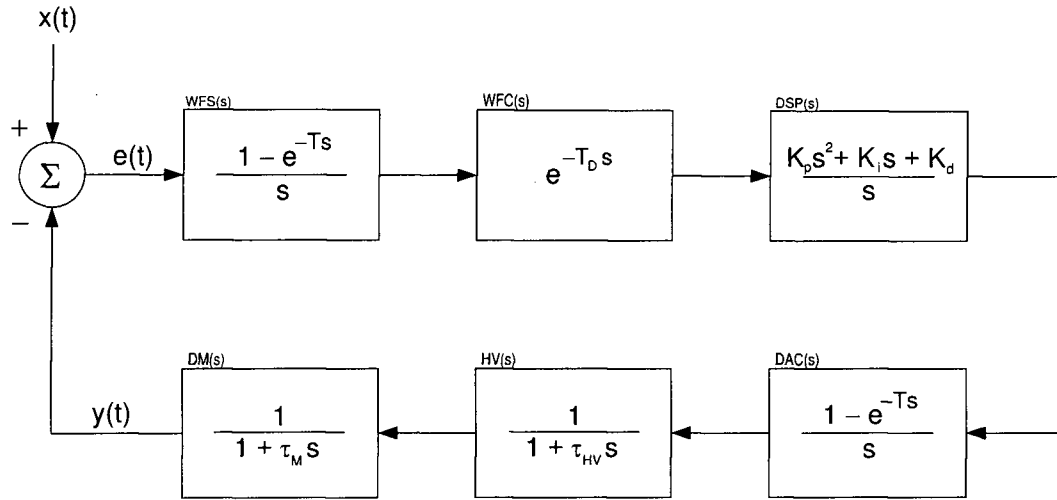
x(t)

$$\frac{1 - e^{-Ts}}{s}$$

WFS(s)

$$e^{-T_D s}$$

WFC(s)

$$\frac{K_p s^2 + K_i s + K_d}{s}$$

DSP(s)

e(t)

$+$

$-$

Σ

y(t)

$$\frac{1}{1 + \tau_M s}$$

DM(s)

$$\frac{1}{1 + \tau_{HV} s}$$

HV(s)

$$\frac{1 - e^{-Ts}}{s}$$

DAC(s)

Figure 4.3: The control system consists of the wavefront sensor, a delay, the DSP compensator, a digital-to- analog converter, a high voltage amplifier, and the membrane mirror. Atmospheric disturbances are represented by $x(t)$, the conjugate mirror shape by $y(t)$ and the optical error signal by $e(t)$.

of the deformable mirror. The signal processing and digital filtering for the AO control system is provided by the CCD controller digital signal processor. The DSP uses the idle time between CCD readouts to extract the curvature signal and provide feedback signals to the membrane mirror in real time. Both the wavefront sensor and the membrane mirror are constructed in such a way that the number of zones can be dynamically varied.

During each readout of the CCD, the guide star image is sampled according to the subaperture pattern. While the next sample is being collected, the DSP computes the curvature for each subaperture. The DSP acts as a digital controller combining the current curvature signals with previous stored results. Finally, the filtered signals are scaled and offset to suit the 8-bit D/A converters and actuator amplifiers which drive the membrane mirror. The wavefront tilt and curvature correction occurs 20 μs after the CCD readout.

The components which make up the adaptive optics control loop are shown in the block diagram of Figure 4.3. The control loop involves the integrating wavefront sensor, CCD readout dead time, the DSP compensator, the zero–order hold effect of the DAC, and the low-pass filter effect of the membrane mirror.

For a CCD with integration time T, the detector accumulates photons and integrates the wavefront perturbations which are evolving at the same time, so

$$w(t) = \int_{t-T}^{t} \phi(t)dt = \int_{t}^{\infty} \phi(t)dt - \int_{t-T}^{\infty} \phi(t)dt \tag{4.1}$$

describes the wavefront sensor. Since the Laplace transform of an integrator is $1/s$ and that of a time lag is $e^{-\tau s}$, then

$$WFS(s) = \frac{1 - e^{-Ts}}{s} \tag{4.2}$$

represents the transfer function of the sensor[43] for integration time T.

The readout of the CCD and computation of the curvature by the DSP is a simple time delay, giving

$$WFC(s) = e^{-T_D s} \tag{4.3}$$

as the transfer function of the dead time T_D.

The digital to analog converter is synchronized to the integration time of the wavefront sensor and operates as a zero-order hold

$$DAC(s) = \frac{1 - e^{-Ts}}{s} \tag{4.4}$$

with a well known transfer function [44].

As previously described, the deformable mirror exhibits a predominantly first-order step response with characteristic rise time τ_M, so

$$DM(s) = \frac{1}{1 + \tau_M s} = \frac{a}{s + a} \tag{4.5}$$

is the mirror transfer function, where $a = 1/\tau_M$. A similar transfer function describes the high voltage amplifiers. But, $\tau_{HV} \ll \tau_M$ which allows the amplifier transfer function to be approximated as $HV(s) = 1$.

Note that in this control loop, the difference signal is generated optically, as the distorted wavefront is conjugated by the membrane mirror to give the error signal, $e(t)$. The error signal is then measured directly by the wavefront sensor. Both of these are somewhat unusual features. In a more conventional control system, the output of the system would be measured and electronically subtracted from a reference signal to generate the error signal.

The control loop has the equivalent of two zero-order holds, a low-pass filter , and dead time – all of which contribute to determining its response. Excluding the DSP compensator, the open-loop transfer function can be estimated in the s-domain as

$$G(s) = \frac{(1 - e^{-Ts})^2}{s^2} \frac{K}{s + a} e^{-T_D s} \tag{4.6}$$

or in the z-domain as

$$G(z) = (1 - z^{-1})^2 \mathcal{Z} \left[\frac{K e^{-T_D s}}{s^2(s + a)} \right] \tag{4.7}$$

where K is the collected gain of the loop components. An expanded expression for the z-transform $G(z)$ is given in Appendix G.

For the initial loop testing, the DSP was programmed as a PID (proportional-integral-derivative) controller. The PID controller is relatively simple to implement, and its tuning reveals some of the loop properties.

The transfer function of the PID controller is described by

$$G_{PID}(s) = \frac{K_d s^2 + K_p s + K_i}{s} \tag{4.8}$$

or

$$G_{PID}(z) = z^{-1} \left[K_p(z - 1) + \frac{1}{2} K_i T(z + 1) + \frac{K_d}{T}(z - 1)^2 \right] \tag{4.9}$$

where K_p, K_i, and K_d are the coefficients of the controller for the proportional, integral and differential terms.

The difference equation used to implement the PID controller is written using a backward difference formula

$$u_k = u_{k-1} + K_p(e_k - e_{k-1}) + \frac{1}{2}K_iT(e_k + e_{k-1}) + \frac{K_d}{T}(e_k - 2e_{k-1} + e_{k-2}) \qquad (4.10)$$

with error signal e_k and output signal u_k at time kT.

A simulation of the overall open-loop frequency response and the closed-loop step response are show in Figure 4.4. With nominal values for $K_p = 100$, $K_iT = 90$ and $K_d/T = 40$ the loop is stable with a gain margin of 20 dB and phase margin of 60 degrees. The closed loop step response is expected to have a 4 sample rise time, with less than 10% overshoot.

4.3 User interface software.

Development of the CHRISP system involved a substantial software component. The software includes a user interface, CCD controller routines, and the overall control system code. The host platform is a SUN Sparcstation. As described previously, the digital signal processor is a Motorola DSP56002.

The graphical user interface to the adaptive optics system was based on existing routines [45] using the XView toolkit. Adding the adaptive optics functions involved rewriting some of the code, and augmenting it with several new modules.

The prototype system operates in two modes: (1) an interactive test mode for setup and testing of the deformable mirror and wavefront sensor, and (2) a closed loop mode in which the control loop is synchronized to the CCD frame rate.

In the interactive test mode, the user is able to read out and display CCD images, and to set the membrane mirror actuator voltages. In the lab, the CCD test capabilities
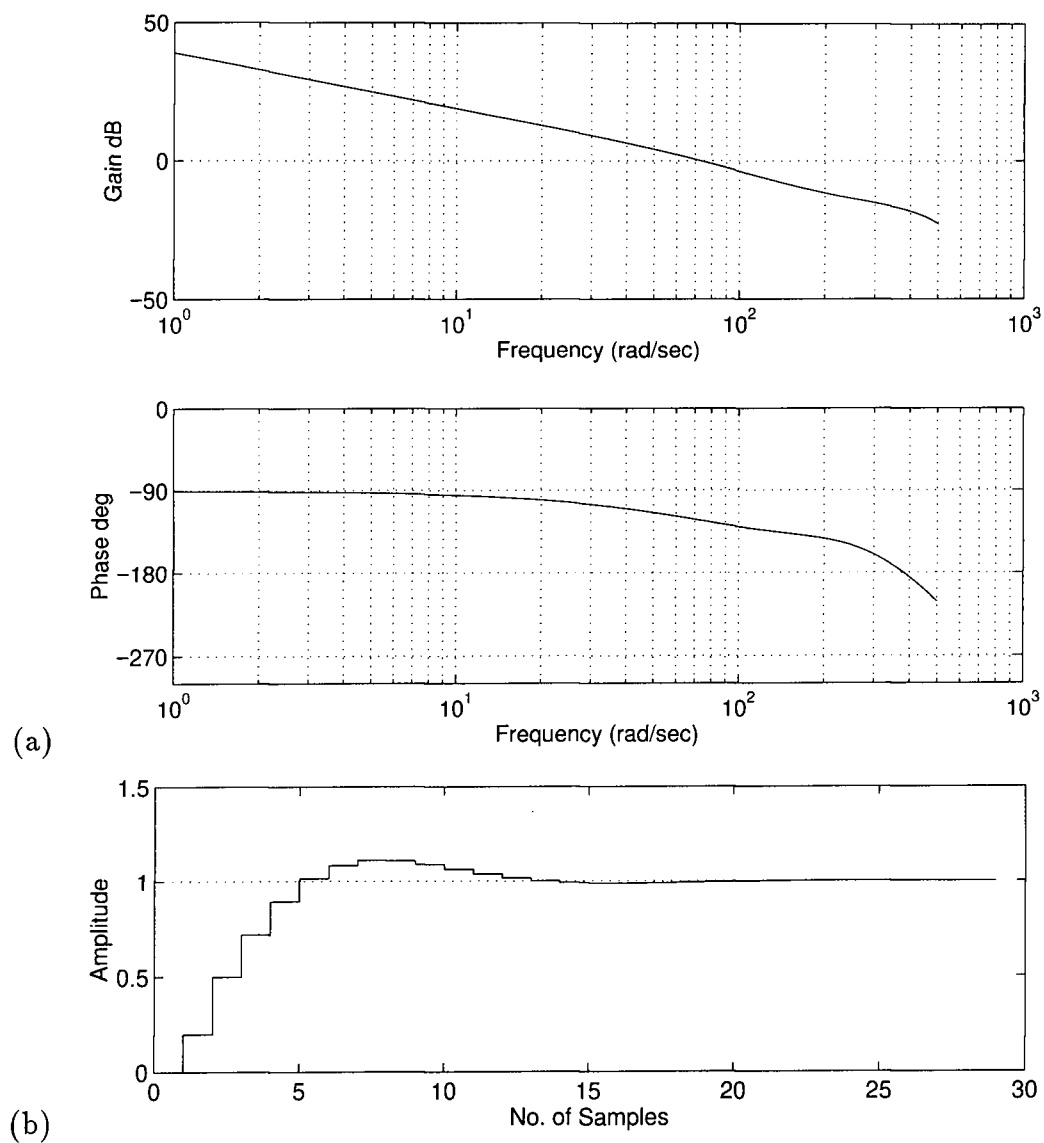
Figure 4.4: (a) The open loop frequency response and (b) closed loop step response simulations are shown. The gain margin is 20 dB, and the phase margin is 60 degrees.

were useful for experimenting with software settable parameters, and for characterizing the CCD noise, dark current and so on. The membrane mirror test capabilities were useful to explore nulling out the membrane aberrations, and for characterizing the tip-tilt dynamic range and step response. At the telescope, the interactive mode is necessary to acquire and center the guide star on the wavefront sensor CCD. It was also useful in acquiring sequences of short exposures to determine the seeing characteristics of the site.

The DSP software is structured in three parts: (1) a collection of routines to operate the CCD and collect the image data (2) a collection of routines to extract the curvature data from the images, process it and drive the membrane mirror (3) service routines to receive parameter values from the Sparc host and to pass back image data from the DSP when required.

Software selectable parameters include the binning, clock timing, and exposure times. Subaperture patterns are selected by a configuration file loaded into the DSP on-chip memory. A DSP service routine periodically checks for new instructions and parameters from the Sparc host.

In operation, command words are sent to the DSP via the serial interface, which interprets them and executes the specified operations on a frame by frame basis. Data is returned to the host computer via a fast SBUS serial interface and may be viewed on-screen. Depending on the operating mode, control may be returned to the host after each complete series of operations.

At the telescope, the CCD is operated in a mode that displays the image on the workstation, essential for acquiring the guide star. When the guide star is acquired, the system is switched to the adaptive optics mode and runs autonomously. For diagnostic purposes, it is also possible to interrupt the control loop to read back the current state of the sensor, the stored bias frame, and the actuator voltages.

Chapter 5

Prototype test results

5.1 Optical bench curvature sensing.

With a simple optical system involving a short focal length lens and a pinhole illuminated by a broadband "white" light source, we have recorded some single, before and after focus images on a small 64×64 pixel CCD. The location of the pinhole on-axis and less than a meter from the lens introduces a strong spherical aberration into the system.

As shown in Figure 5.1, the experimental set-up consisted of a pinhole light source, a 55 mm F/1.4 Nikkor copy lens, a fast shutter, and a TEK64 CCD and controller. An intervening layer of diffuser (3M tape) ensured even illumination of the pinhole. All components were mounted on an optical rail at a common height. Micropositioners were used to align the three elements, and defocus the image to the proper size. Tip-tilt and other lower order aberrations were removed by fine tuning, leaving mostly spherical aberration present in the test images.

With only spherical aberration present, the wavefront can be described by $w = A_s(r/R)^4$, so that $\nabla^2 w$ within the aperture will be a paraboloid. Following a derivation by Hickson [46], from purely geometric considerations the peak spherical aberration generated in the experimental arrangement is described by

$$A_s = \frac{(u - F)R^4}{8u^2 F^2} \tag{5.1}$$

which is expected to produce a curvature signal of

$$\frac{\Delta I}{I_0} = \frac{16 A_s f(f - \ell)}{\ell R^2} (\frac{r}{R})^2 \tag{5.2}$$

WFS   L1   100.00 MM   PH

Figure 5.1: Laboratory bench top optical setup used to generate spherical aberration and measure curvature from a single image.

within the aperture. The parameters are the distance u from the source to the lens, the distance f from the lens to the focus, the focal length F and radius R of the lens, and the extra-focal distance ℓ of the detector. A positive result corresponds to the after-focus position. A derivation of this result is in Appendix F.

Using the optical configuration described, we obtained some high signal-to-noise ratio images. Each test image involved a 50 ms exposure with CCD readout at the normal rate, followed by the usual CCD bias removal and flat fielding process. A fast flush of the detector preceded the exposure to simulate continuous operation. After computing the mean intensity I_0 over the aperture, the curvature map was extracted from $I(r)$ and I_0 on a pixel by pixel basis.

Figure 5.2(a) shows a 64x64 pixel inside-focus image generated with this arrangement. A cross-section of the curvature map and a low order polynomial fit to the curvature signal appear in Figure 5.2(b). With an $F = 55$ mm $F/1.4$ lens, a pinhole located at $u = 650$ mm produced a 1.44 mm diameter image on the CCD. In this case, the expected spherical aberration was $A_s = -8.6\mu$m. Within the experimental error, the measured curvature signal agrees with the predicted $\Delta I/I_0 \simeq -0.6(r/R)^2$. There is a higher order term proportional to $(r/R)^4$ present in the curvature signal that does not match the expected geometric value. Perhaps the compound Nikkor lens was not well compensated for this term.
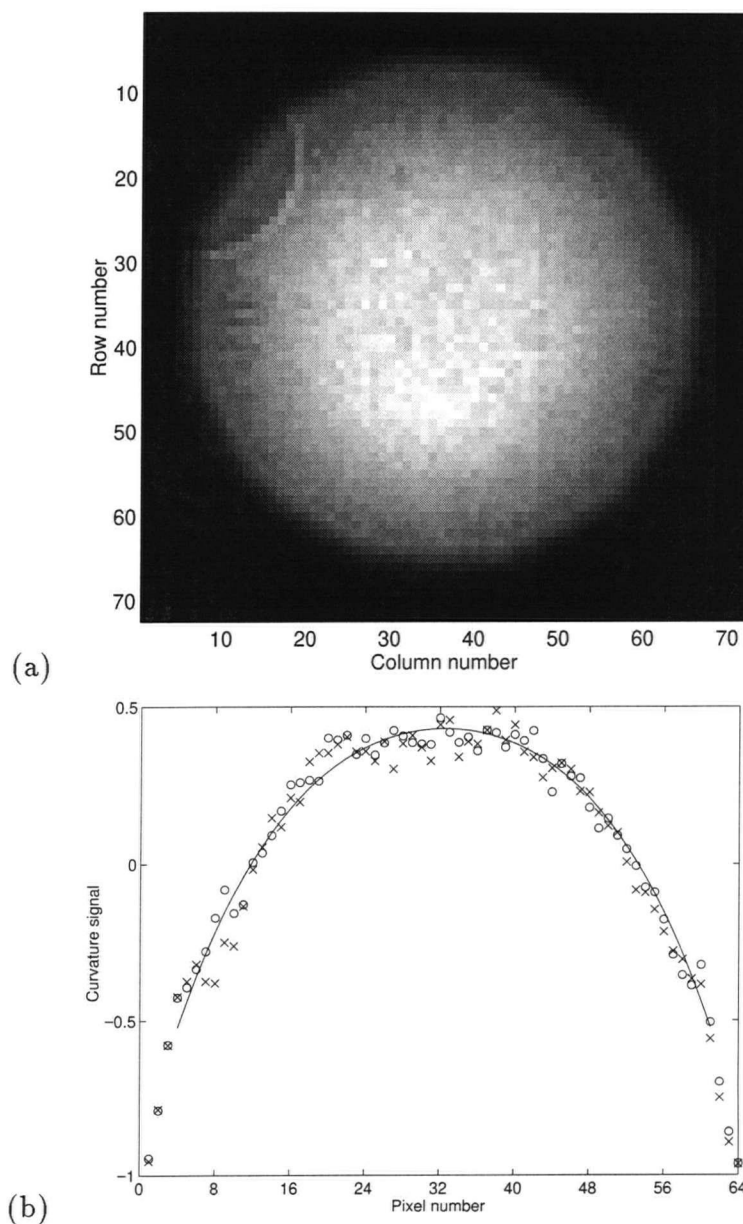
Figure 5.2: (a) Inside-focus CCD image and (b) sample cross-sections. A white light illuminated pinhole is re-imaged onto the 64×64 CCD with spherical aberration. Vertical cross-sections of the extracted 64×64 curvature map are shown with a parabolic fit to the $\Delta I/I_0$ curvature signal. The feature at 10 o'clock is a defect in the lens.

5.2 On-telescope wavefront sensing.

Using the wavefront sensor strictly as a seeing monitor, we obtained the results indicated in Figures 5.3 and 5.4. Each sequence shows the evolving centroid position, where each pixel represents 0.35 arcsec. Traces for both the x and y components of the centroid position are shown. The centroid position was computed by post-processing the images. Figure 5.3 is an expanded view of one of the sequences of centroid positions shown in Figure 5.4.

Aside from the apparent random motion on both large and small scales, there does appear to be some regular low frequency motion in many of the sequences on a 0.4, 0.8, or 1.6 second scale, which might indicate telescope resonances excited by guiding or wind shake. The sequences are not long enough for a Fourier transform to provide any useful frequency resolution.

Figure 5.5 shows a sequence of images of Arcturus, where each image is a 5 ms exposure in the R-filter [λ=700 nm], followed by a 20 ms delay. The sequence evolves columnwise, and shows not only the motion of the image centroids, but also the shape changes which occur in the image on a 25 ms timescale. These images also demonstrate the fast frame rates possible with the wavefront sensor.

The x and y components of the tip-tilt motions were 0.2 arcsec rms. The combined tip-tilt of 0.28 arcsec suggests an $r_0 = 10$ cm, using

$$\alpha_{rms} = \frac{0.42\lambda}{r_\lambda^{5/6} D^{1/6}} \tag{5.3}$$

where α_{rms} is the rms image motion. This is equivalent to 1.0 arcsec images in the absence of any dome seeing effects. For comparison, when the 64 frames in a typical sequence are co-added, the estimated FWHM of the image gives an $r_0 \simeq 6$ cm. The local seeing must be significant.

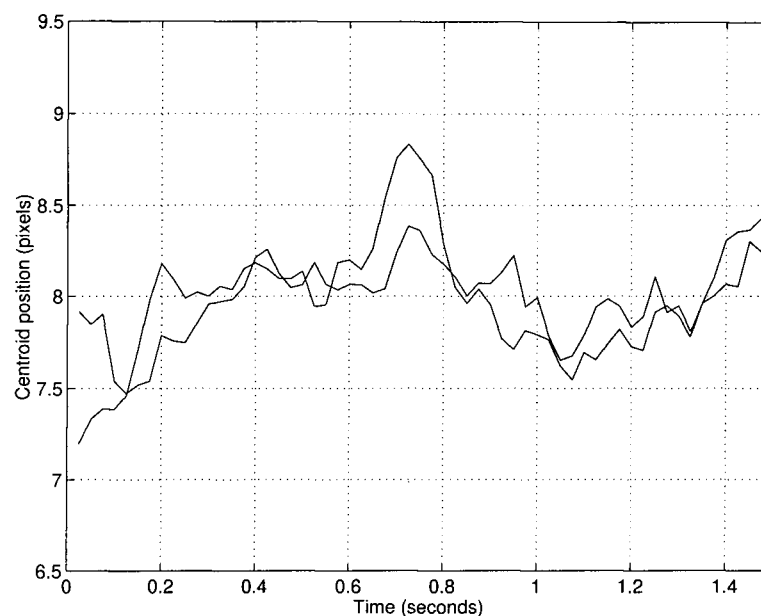Acquiring the guide star is one of the most challenging aspects of operating the

Figure 5.3: Image motion in R filter. Each exposure was 5 ms followed by a 20 ms delay to create this sequence. Each pixel represents 0.35 arcsec on the sky. The two traces show the x and y components of the centroid motion.

prototype. The wavefront sensor CCD has a field of view of only 5 arcsec × 5 arcsec, which makes locating the guide star a frustrating task.

5.3 On-telescope optical tests.

During each telescope run, the adaptive optics system was assembled in the slit room of the DAO 1.2-m telescope. The optical components were fastened to pre-positioned locations on the aluminum plates, then rotated and translated into their final positions. These were measured carefully to closely correspond to the optical design.

To align the system, we back projected a laser from the spectrograph slit to the secondary mirror mounting bolt and centered the beam on all the components using
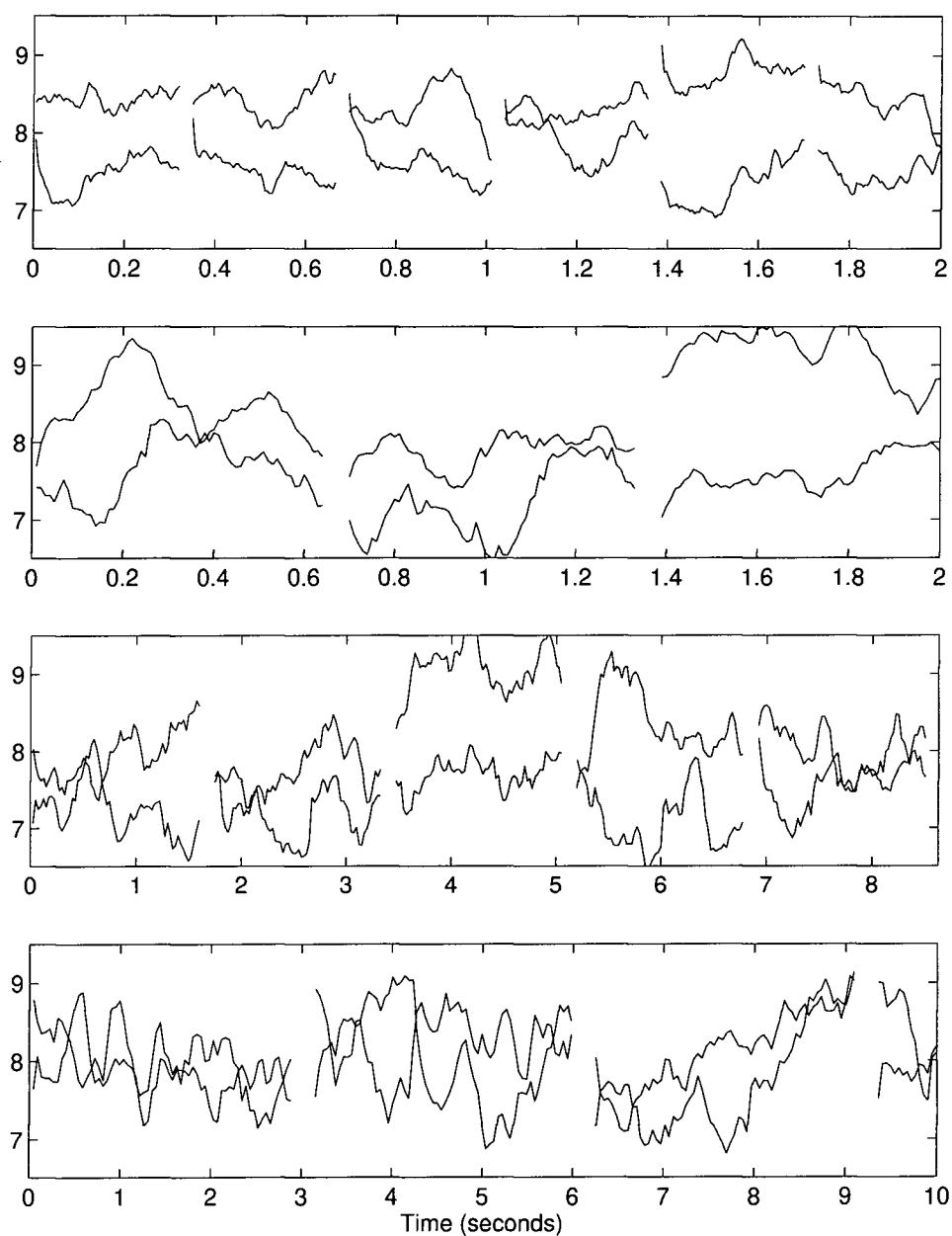
Figure 5.4: Centroid positions from image sequences at DAO 1.2-m telescope. Each exposure was 5 ms followed by 0, 5, 20 or 40 ms delay (from top to bottom). The guide star was Arcturus observed in the R-filter with 4x4 binning for 0.35 arcsec per pixel.
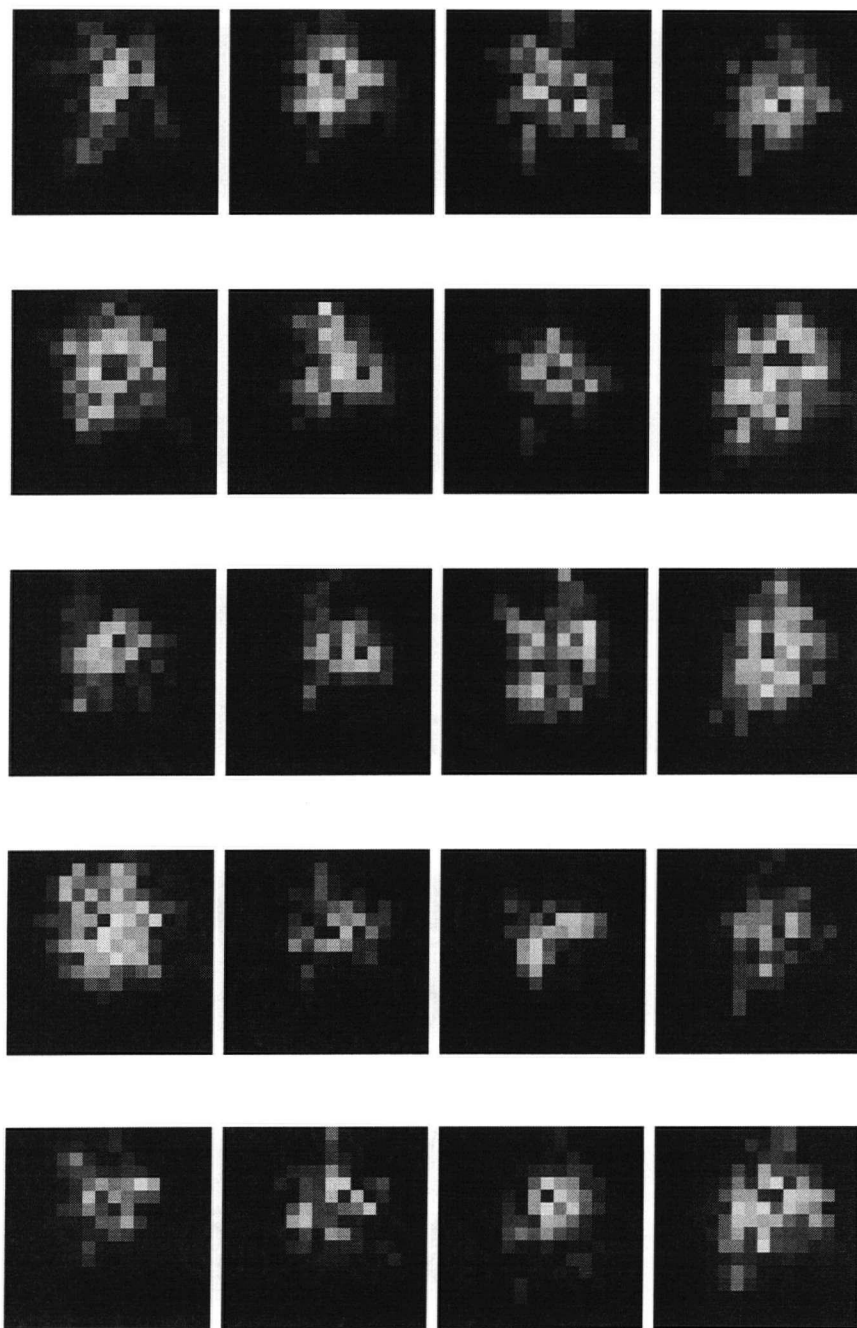
Figure 5.5: Guide star images. An evolving sequence (columnwise) of 16x16 pixel images of Arcturus in the R-filter demonstrating the rapid imaging capability of the wavefront sensor. Exposures are 5ms separated by 20 ms delay.

cross-hair targets. Other than lens L2, the components were not overly sensitive to tip-tilt changes. The simplicity of the optical design eased the alignment process, which proved repeatable over several dates at DAO.

Once the proper tip-tilt and centering of L2 was accomplished, the system was star-tested without correction. Using a behind-the-slit viewer to observe a bright star, it was possible to bring the complete system to a "best focus" and observe speckles in the image to confirm that the optical design was sound and that the system was seeing limited (even with the membrane mirror aberration).

5.4 Optical bench membrane mirror aberration removal.

With the system in its interactive mode, it is possible to adjust the individual actuator voltages to remove some of the membrane mirror aberration. The goal of this exercise was to produce a round, evenly illuminated and defocused image of the pinhole. Figure 5.6 shows the before-focus images with no adjustment, and with the mirror actuators adjusted to minimize the mirror aberration(s). The image sizes are different due to a slight amount of defocus. Without adjustment, the membrane mirror produces a delta shaped image, likely indicating some pinching of the membrane tension ring. With the actuators active, the image is improved but the mirror is still not able to completely cancel its own aberrations.

5.5 Optical bench closed loop tests.

On the optical table, the system was tested in a variety of closed-loop modes, with mixed success. The residual aberration of the membrane mirror and limited dynamic range for self-correction made a number of possible tests of the loop response impractical.

On the optical bench, the arrangement of Figure 3.9 was used, again with a laser
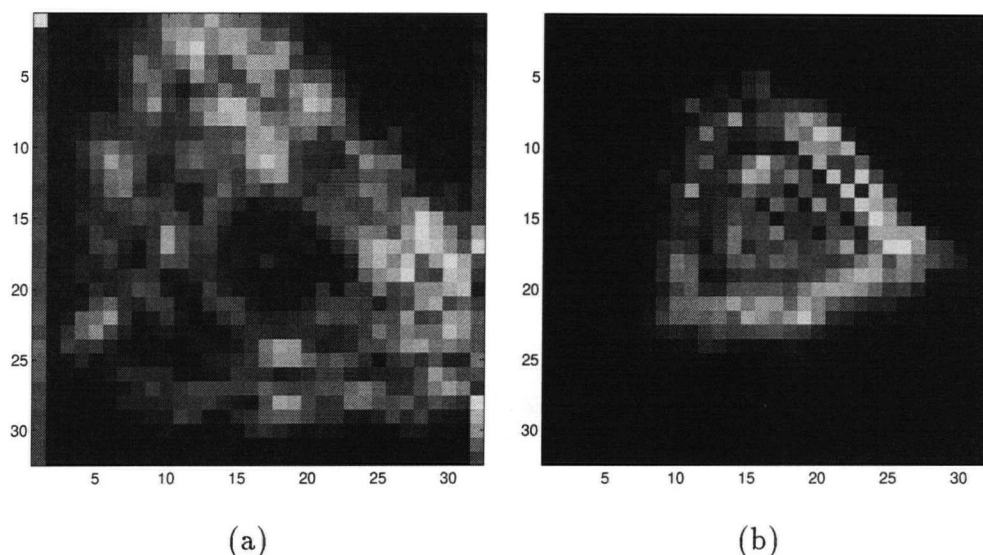
(a)   (b)

Figure 5.6: The artificial guide star as seen by the wavefront sensor on the optical bench (a) uncorrected, and (b) with correction to minimize the mirror aberration. The two images are different sizes since the amount of defocus is slightly different.

illuminated pinhole as the source. The beam was passed through an aperture mask to produce the proper f-ratio and beam diameter on the membrane mirror. A video camera was mounted at the focus to monitor the results of the closed-loop tests. In addition, the output voltage of the amplifier driving the central electrode was probed with a digital storage oscilloscope to monitor the loop step response.

The laser illuminating the pinhole had a chronic malfunction which would cause it to have periodic bursts of flickering intensity followed by "normal" stable operation. During the periods of laser instability, the control loop would lose lock and the control voltages would become thoroughly randomized. While this was very annoying, it did provide a useful tool to diagnose the ability of the loop to return to its set-point.

In the simplest case, the central subapertures of the wavefront sensor and the central actuators of the membrane mirror were operated as one large element. Provided the optical system was well aligned, the control loop was stable with a controlled step response,
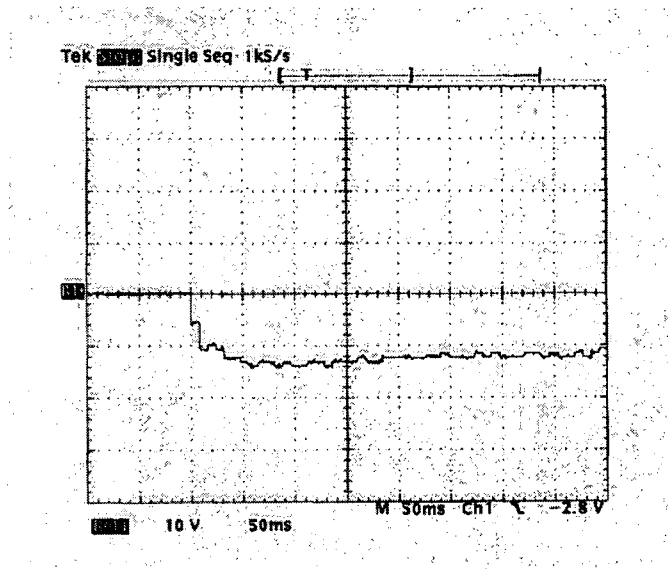
Figure 5.7: Closed loop step response of AO control loop.

as shown in Figure 5.7. In this case, the rise time was about 20 ms, with less than 20%
overshoot. Even as the laser malfunctioned and randomized the control voltage, the loop
would immediately return to the setpoint when the laser re-stabilized.

The rise time and degree of overshoot in the step response were controllable by adjust-
ing the PID controller parameters. For instance, by increasing the proportional gain the
loop would exhibit large overshoots or be driven into oscillation. There was a wide range
of parameters which produced a stable, well-behaved control loop, generally involving all
three terms of the PID controller.

With the seven central electrodes operating simultaneously, the alignment of the
optical system became more critical. Each sensor-electrode pair operated independently,
and with the same controller parameters as the others. For the well-aligned tests, the
loop was again stable with a step response similar to Figure 5.7. With sufficient optical
mis-alignment(s), the control loop would be unable to find a stable operating point.

When thoroughly randomized, the control loop often had poor response as adjacent sensor-mirror zones had some degree of cross-coupling and would interact with one another. The mirror would eventually settle to the previous stable operating point, but the settling time could be much, much longer. The interaction matrix between the sensor and mirror zones obviously has some non-diagonal terms, which were not accounted for in the control loop.

In a final test, the one central electrode was operated with the twelve boundary electrodes. The control loop was able to find a stable operating point for the central actuator, but most of the boundary actuators were driven to the limits of their control range. The boundary actuators did not have the dynamic range to correct for the distorted image shape produced by the aberrated mirror.

Chapter 6

Summary and Conclusions

6.1 Summary.

The guiding principle behind the design of the CHRISP system was to reduce the complexity at every possible point. To achieve this, the system was designed and built using single image curvature sensing with a CCD wavefront sensor, a single deformable mirror for both tip-tilt and low order correction, and a simple, easily aligned optical layout.

The prototype wavefront sensor has demonstrated that a CCD based curvature sensor is a practical, technically viable device. In fact, the analysis has shown that it can be competitive with an APD based sensor provided that it is optimized for the task with a high quality detector. A small format, low-noise, high quantum efficiency, frame transfer CCD with a DSP based controller would make a near-ideal versatile wavefront sensor.

In operation, superpixel binning for the curvature sensor readout made fast frame rates and low-noise readout compatible. The curvature signal was extracted efficiently and quickly, without flat fielding. The DSP-based design for the CCD controller meant that code for the entire system could be made very compact and efficient. The DSP also had the advantage of acting as the digital compensator in the adaptive optics control loop.

The deformable membrane mirror prototyped for these experiments was inexpensive and relatively simple to construct. Its testbed performance indicated that substantial tip-tilt and low order Zernike correction could be obtained from a single device. The size

of the device, ease of use, stability, aperture size, actuation range and time response all proved to be appropriate for adaptive optics use. The simplified high voltage amplifier electronics eased the task of building many parallel drivers.

Properties of the membrane mirror such as curvature or deflection voltage sensitivity and dynamic range could be changed by adjusting the bias voltage or membrane to electrode spacing. These properties could also be estimated with good results by numerical simulation. From evaluating the prototype, I discovered the principal limitations to be the dynamic response time, and the membrane support system.

Various parts of the CHRISP system have undergone operational tests at the DAO 1.2 meter telescope. The prototype wavefront sensor has been used on a number of nights to perform seeing measurements. The basic optical system, including the membrane mirror, has been set up and aligned at the telescope successfully several times. Even with the membrane aberration, the images through the system were seeing limited.

Single image curvature sensing has been demonstrated in the lab on an optical bench, both in detecting a known aberration in an optical system and in limited closed-loop operation of the adaptive optics system. The simplicity of the approach is appealing and recommends itself.

6.2 Conclusions.

As a proof-of-concept, the CHRISP experiment has demonstrated the viability of the CCD curvature sensor, and the potential of the deformable membrane mirror. The sensor is capable of 500 frames per second, with $10e^-$ read noise. The mirror is capable of both tip-tilt and low order correction, with a 10 ms step response. The closed-loop zonal control system is stable (in limited testing). The overall design of the system demonstrates that these components can be integrated into a simple, low-order adaptive

optics system. The total hardware cost for the system was US$20K, which is at least an order of magnitude smaller than competing systems.

The CHRISP experiment was intended to show that even at mediocre sites, adaptive optics can improve the seeing to make small telescopes more effective and scientifically productive. On a good night at the DAO site with $D/r_0 = 6$, the CHRISP system would be expected to achieve Strehl ratio improvements of a factor of 10, and images with diffraction cores of 0.3 arcsec limited by the overall optical performance of the system. A full scale experimental test on the telescope is still in the future.

The main limitation to the system is the uncorrectable optical aberration due to the mounting scheme for the membrane.

Future work on the system must include a redesign of the mirror to include a zero-force mount which avoids pinching or bending the membrane tension ring. Closed-loop testing of the boundary actuators, and on-telescope testing could follow.

References

[1] J.Hardy,"Adaptive Optics," Scientific American, 60–65 (1994).

[2] J.Beckers, "Adaptive optics for astronomy: Principles, performance and applications," ARAA 31, 13–62 (1993).

[3] H.Babcock, "The possibility of compensating astronomical seeing," PASP 65, 229–236 (1953).

[4] F.Roddier, J.Anuskiewicz, J.E.Graves, M.J.Northcott, C.Roddier, "Adaptive optics at the University of Hawaii I: Current performance at the telescope," SPIE 2201 Adaptive Optics in Astronomy, 2–9 (1994).

[5] S.McArthur, F.Rigaut, R.Arsenault, "Adaptive optics bonnette," CFHT Bulletin 35, 11–13 (1996).

[6] G.Rousset, J.Beuzit, N.Hubin, E.Gendron, P.Y.Madec, C.Boyer, J.P.Gaffard, J.C.Richard, M.Vittot, P.Gigan, P.Lena, "Performance and results of the COME-ON+ adaptive optics system at the ESO 3.6 meter telescope," SPIE 2201 Adaptive Optics in Astronomy 1088–1098 (1994).

[7] F.Roddier, "Curvature sensing and compensation: a new concept in adaptive optics," Applied Optics 27, 1223–1225 (1988).

[8] F.Roddier, M.Northcott and J.Graves, "A simple low-order adaptive optics system for near-infrared applications," PASP 103, 131–149 (1991).

[9] R.Arsenault, D.Salmon, J.Kerr, F.Rigaut, D,Crampton, W.Grundman,"PUEO: The Canada-France-Hawaii telescope adaptive optics system 1: System description," SPIE 2201 Adaptive Optics in Astronomy 833–842 (1994).

[10] D.L.Fried, "Optical resolution through a randomly inhomogeneous medium for very long and very short exposures," JOSA 56, 1372–1379 (1966).

[11] J.Y.Wang and J.K.Markey, "Modal compensation of atmospheric turbulence phase distortion," JOSA 68, 78–86 (1978).

[12] R.J.Noll, "Zernike polynomials and atmospheric turbulence," JOSA 66, 207–211 (1976).

[13] F.Roddier, "Status of astronomical adaptive optics developments," in *High Resolution Imaging by Interferometry II*, J.M.Beckers and F.Merkle eds, 571–586 (1992).

[14] N.Roddier, "Atmospheric wavefront simulation and Zernike polynomials," SPIE 1237 Amplitude and Intensity Spatial Interferometry, 668–679 (1990).

[15] R.Racine,"The telescope point-spread function," PASP 108, 699–705 (1996).

[16] G.A.H.Walker, A.R.Walker, R.Racine, J.M.Fletcher, R.D.McClure, "Direct Imaging of Faint Stellar Companions," PASP 106, 356–362 (1994).

[17] F.Roddier, "Curvature Sensing: a Diffraction Theory," NOAO R&D Note 87-3 (1987).

[18] F.Roddier, C.Roddier, N.Roddier, "Curvature sensing: a new wavefront sensing method," SPIE 976 Statistical Optics, 203–209 (1988).

[19] P.Hickson, "Wavefront curvature sensing from a single defocused image," JOSA 11 1667–1673 (1994).

[20] P.Hickson and G.Burley, "Single image wavefront curvature sensing," SPIE 2201 Adaptive Optics in Astronomy, 549–554 (1994).

[21] R.Centamore and A.Wirth, "High bias membrane mirror," SPIE 1543 Active and Adaptive Optical Components, 128–132 (1991).

[22] H.Takami and M.Iye, "Membrane deformable mirror for SUBARU adaptive optics," SPIE 2201 Adaptive Optics in Astronomy, 762-767 (1994).

[23] G.Burley and J.R.Stilburn, "Membrane mirror and driver electronics," NRC IP division invention disclosure (1994).

[24] G.S.Burley, G.A.H.Walker, J.R.Stilburn, and R.Murowinski, "Versatile wavefront sensor," NATO ASI *Adaptive Optics for Astronomy*, Cargese (1993).

[25] R.Reiss, "Array Controller Electronics (ACE) ESO's next generation of CCD controllers for the VLT," SPIE 2198 Instrumentation in Astronomy VIII, 895–906 (1994).

[26] P.E.Doherty, P.Sutcliffe, G.R.Sims,"High performance dual speed, multi-port CCD camera," SPIE 1656 High-Resolution Sensors and Hybrid Systems, 315–326 (1992).

[27] R.Johnson,"UBC detector control system," UBC internal report (1988).

[28] P.Chen and J.Novello, "A general purpose CCD controller," PASP 101, 940–946 (1989).

[29] S.D.Gillam, P.E.Johnson, M.Smith " A simple visual Cassegrain CCD camera for the Wyoming Infrared Observatory," PASP 104, 279–284 (1992).

[30] R.W.Leach, "Design of a CCD controller optimized for mosaics," PASP 100, 1287–1295 (1988).

[31] I.McLean, *Electronic and Computer Aided Astronomy*, Wiley (1989).

[32] Marlow Industries, *Thermoelectric cooler selection guide* (1990).

[33] W.Petrick,"Generalized approach to cooling charge-coupled devices using thermo-electric coolers," Optical Engineering 26, 965–971 (1987).

[34] J.Stilburn, private communication (1995).

[35] Motorola, *DSP56000 Digital Signal Processor Family Manual* (1992).

[36] Burr-Brown, *Linear Products* (1994).

[37] Analog Devices, *Design-In Reference Manual* (1994).

[38] J.Janesick, K.Klaasen, T.Elliot, "CCD charge collection efficiency and the photon transfer technique," SPIE 570 Solid State Imaging Arrays, 7–19 (1985).

[39] R.Grosso and M.Yellin, "The membrane mirror as an adaptive optical element," JOSA 67, 399–406 (1977).

[40] F.Forbes, F.Roddier, G.Poczulp, C.Pinches, G.Sweeny and R.Dueck, "Segmented bimorph deformable mirror," J. Physics E:Scientific Instrument 22, 402–405 (1989).

[41] B.Carnahan, H.Luther, and J.Wilkes, *Applied Numerical Methods*, 482–485, Wiley (1969).

[42] J.S.Pazder, private communication (1994).

[43] M.Demerle, P.Y.Madec, G.Rousset, "Servo-loop analysis for adaptive optics," in *Adaptive Optics for Astronomy*, NATO ASI Series 423, 73–88 (1992).

[44] R.Jacquot,*Modern Digital Control Systems*, Marcel Dekker (1981).

[45] R.Johnson, private communication (1992).

[46] P.Hickson, private communication (1994).

[47] J. Beckers, "Interpretation of out-of-focus star images in terms of wavefront curvature," JOSA 11, 425–427 (1994).

[48] G.A.H.Walker, *Astronomical Observations*, Cambridge University Press (1987).

[49] J.R.Stilburn, "A quadrant detector for guidance image stabilization systems," PASP 104, 955–957 (1992).

Appendix A

Zernike polynomials

The Zernike polynomials are useful for describing optical systems, as the low order terms correspond to familiar aberrations such as tilt, focus, astigmatism and so on [12]. In polar coordinates, they are described as a product of angular functions and radial polynomials. Each is normalized so that the rms value of the polynomial over the unit disk is 1.

$$Z_{evenj} = \sqrt{n+1} R_n^m(r) \sqrt{2} \cos(m\theta) \tag{A.1}$$
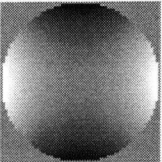
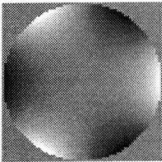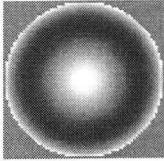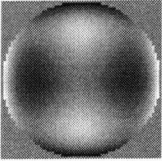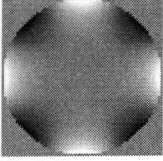$$Z_{oddj} = \sqrt{n+1} R_n^m(r) \sqrt{2} \sin(m\theta)$$
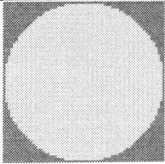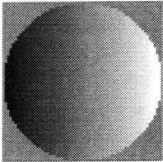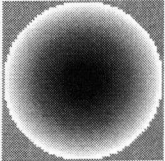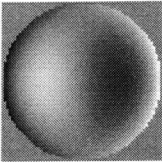
$$Z_{m=0} = \sqrt{n+1} R_n^0(r)$$

where

$$R_n^m(r) = \sum_{s=0}^{(n-m)/2} \frac{(-1)^s (n-s)!}{s![\frac{1}{2}(n+m)-s]![\frac{1}{2}(n-m)-s]!} r^{n-2s} \tag{A.2}$$

The index n is the radial degree, and the index m is the azimuthal order. The ordering j is arbitrary. Table A.1 shows the mathematical expression and appearance of the first 15 Zernike polynomials.

Table A.1: Zernike Polynomials.

Radial degree	Azimuthal frequency				
	0	1	2	3	4
0	$z1 = 1$				
1		$z2 = 2r\cos(\theta)$ $z3 = 2r\sin(\theta)$ Tilts (lateral position)			
2	$z4 = \sqrt{3}(2r^2 - 1)$ Defocus		$z5 = \sqrt{6}r^2\sin(2\theta)$ $z6 = \sqrt{6}r^2\cos(2\theta)$ Astigmatism (3rd order)		
3		$z7 = \sqrt{8}(3r^3 - 2r)\sin(\theta)$ $z8 = \sqrt{8}(3r^3 - 2r)\cos(\theta)$ Coma (3rd order)		$z9 = \sqrt{8}r^3\sin(3\theta)$ $z10 = \sqrt{8}r^3\cos(3\theta)$	
4	$z11 = \sqrt{5}(6r^4 - 6r^2 - 1)$ Spherical (3rd order)		$z12 = \sqrt{10}(4r^4 - r^2)\cos(2\theta)$ $z13 = \sqrt{10}(4r^4 - r^2)\sin(2\theta)$		$z14 = \sqrt{10}r^4\cos(4\theta)$ $z15 = \sqrt{10}r^4\sin(4\theta)$

Appendix B

Geometric optics and curvature sensing

Following the geometric optics description originally set forth by Beckers [47], the out-of-focus image intensity distribution can be interpreted in terms of the wavefront curvature.
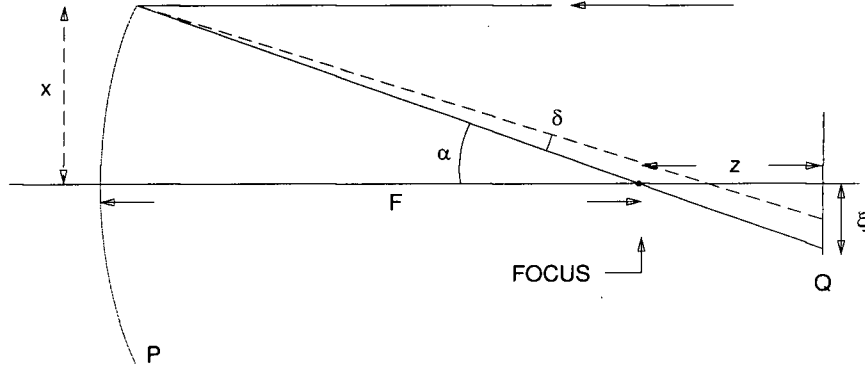

Figure B.1: Geometric optics interpretation of curvature sensing.

In the figure, for perfect optics the ray coming from the pupil P at a distance x from the axis intersects Q at

$$\xi(x) = \frac{xz}{F} \tag{B.1}$$

where F is the telescope focal length and z is the defocus distance. When the optics are distorted by $\Omega(x)$, the ray deviates by an angle $\delta(x)$, so that

$$\delta(x) = 2\frac{d\Omega(x)}{dx} \tag{B.2}$$

and it intersects Q at

$$\xi(x) \approx \frac{xz}{F} + \delta(x)(F + z) \tag{B.3}$$

using the small angle approximation.

The intensity in the out-of-focus image is proportional to

$$I \sim \left| \frac{d\xi(x)}{dx} \right| = \left| \frac{z}{F} + (F + z)\frac{d\delta(x)}{dx} \right| = \left| \frac{z}{F} + 2(F + z)\frac{d^2\Omega(x)}{dx^2} \right| \tag{B.4}$$

so the last term relates the spatial intensity variations of the out-of-focus image to the curvature of the wavefront. A similar explanation can be given for the two-dimensional case.

Appendix C

Calculating the guide star magnitude

For a detector affected by read noise [48], the signal-to-noise ratio is given by

$$\text{SNR} = \frac{nq}{(nq + \sigma^2 m)^{1/2}} \tag{C.1}$$

where the various parameters are defined in Table C.1, with associated values. Rearranging the equation and applying the quadratic formula

$$(nq)^2 - \text{SNR}^2(nq) - \text{SNR}^2\sigma^2 m = 0 \tag{C.2}$$

$$nq = \frac{1}{2} \cdot \text{SNR}^2 \left\{ 1 + \left[1 + \frac{4\sigma^2 m}{\text{SNR}^2} \right]^{1/2} \right\} \tag{C.3}$$

or

$$n = \dot{n}T = \frac{\text{SNR}^2}{2q} \left\{ 1 + \left[1 + \frac{4\sigma^2 m}{\text{SNR}^2} \right]^{1/2} \right\} \tag{C.4}$$

where T is the integration (or the sampling rate is $f_s = 1/T$). The arrival rate of photons at the detector (per subaperture) $\dot{n}$ is given by

$$\dot{n} = \frac{\pi \epsilon D^2}{4a} \dot{n}_0 10^{-m^*/2.5} \tag{C.5}$$

so that combining equations C.4, and C.5 gives an expression

$$m^* = -2.5 \log \left\{ \frac{4 a f_S}{\pi \epsilon D^2} \frac{n}{\dot{n}_0} \right\} \tag{C.6}$$

that can be used to estimate the guide star magnitude for the adaptive optics system. Equation C.6 relates the guide star magnitude obtainable to a given set of detector characteristics, telescope characteristics and sampling rate.

Table C.1: Guide star calculation parameter values

Symbol	Definition	Value
n_c	order of correction	1 2 3 4
a	number of subapertures	4 7 13 19
q	detector quantum efficiency	70 %
σ	rms read noise	2.5 electrons
m	number of pixels (per subaperture)	8
SNR	signal-to-noise ratio	5
D	telescope diameter	1.2m
$\dot{n}_0$	zero mag photon flux [500 to 900 nm]	2.5×10^{10} photons $s^{-1}m^{-2}$
ϵ	atmosphere/optics efficiency	100 %
f_0	sampling rate constant	200

Appendix D

Comparison of APD and CCD detectors

High quantum efficiency, low noise CCD detectors have become an attractive alternative to APD based sensors. Table D.1 illustrates reasonable parameters for the competing technologies.

Table D.1: APD and CCD comparison

	QE	Noise	Optical BW
APD	.35	none	500 to 900 nm
CCD	.80	< 5	500 to 900 nm

The performance of CCD and APD detectors can be compared for various CCD read noise levels. The number of photons per subaperture is determined from

$$n = \frac{\text{SNR}^2}{2q} \left\{ 1 + \left[1 + \frac{4\sigma^2 m}{\text{SNR}^2} \right]^{1/2} \right\} \tag{D.1}$$

where SNR is the signal to noise ratio, q is the quantum efficiency, σ is the rms read noise in e^-, and m is the number of pixels per subaperture for the CCD.

In Figure 1.5, the plot shows the number of incoming photons required by CCD and APD single image curvature sensors, and a CFHT style APD differential curvature sensor. As suggested by HRCam results, a value of SNR = 5 is used for the limiting signal-to-noise [49]. Other parameters used for the comparison are shown in the figure. Under these conditions, the single image CCD sensor outperforms the single image APD

sensor for read noise levels of 2.5e$^-$ or less and the APD differential sensor for read noise levels of 6e$^-$ or less.

Consider the intersection point of the curves at a read noise of 2.5e$^-$. For the two detectors, we have the following:

APD   For 70 incoming photons and quantum efficiency of .35
Signal = 70 * 0.35 = 25 counts
Noise = $\sqrt{25}$ = 5
SNR = 5

CCD   For 70 incoming photons and quantum efficiency of .70
Signal = 70 * 0.7 = 50 counts
Shot noise = $\sqrt{50}$ = 7.1
Read noise = $\sqrt{(2.5)^2(8)}$ = 7.1
SNR = 50 / $\sqrt{(7.1)^2 + (7.1)^2}$ = 5

Note that the requirement for CCD read noise of less than 2.5e$^-$ and quantum efficiency of 80% are within the reach of available technology (1995).

Equation D.1 allows CCD and APD detectors to be compared for different levels of CCD read noise, assuming the quantum efficiencies and signal-to-noise ratio are known. Equating $n_{APD} = n_{CCD}$ yields an expression for the CCD read noise which would give equivalent performance to a noise-less APD

$$\sigma = \frac{\text{SNR}}{m^{1/2}} \cdot \left[\frac{q_{CCD}^2}{q_{APD}^2} - \frac{q_{CCD}}{q_{APD}} \right]^{1/2} \tag{D.2}$$

which depends only on the ratio of quantum efficiencies, the signal-to-noise ratio, and the number of pixels read.

Figure D.1 displays the equivalence points for a range of limiting SNR values. Only at low values of SNR is the read noise requirement beyond the limit of available CCD performance (in 1996).
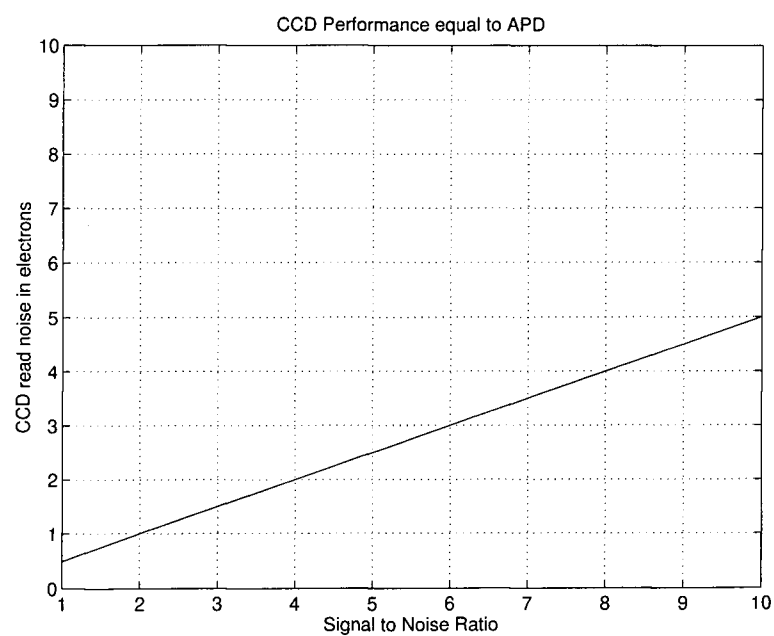
Figure D.1: The performance of CCD vs APD detectors as a function of SNR.

Appendix E

Derivation of the MM equations

Consider a circularly symmetric membrane mirror with a support ring of radius r_f, an actuated area of radius r_a, and a central actuator pad of radius r_p. For an electrostatically actuated membrane, the behaviour of the membrane surface is described by

$$\nabla^2 z = \frac{\epsilon_0}{T\ell_0^2}(V^2 - V_B^2) \tag{E.1}$$

with actuator voltage V, bias voltage V_B, membrane tension T, and spacing ℓ_0.

In cylindrical polar coordinates, $\nabla^2 z = a$ can be directly integrated as follows:

$$\frac{1}{r}\frac{\partial}{\partial r}\left(r\frac{\partial z}{\partial r}\right) = a \tag{E.2}$$

$$\frac{\partial z}{\partial r} = \frac{1}{2}ar + \frac{b}{r} \tag{E.3}$$

$$z(r) = \frac{1}{4}ar^2 + b\ln r + c \tag{E.4}$$

Allowing for different values of the constants a, b, c in the three zones, we note that at the edge of the membrane $z(r_f) = 0$, in the non-actuated area $a_3 = 0$, and in the center of the membrane $\frac{\partial z}{\partial r}\big|_{z=0} = 0$ (ie. $b_1 = 0$). Also, both $z(r)$ and $\frac{\partial z}{\partial r}$ must be continuous across the zone boundaries.

For $0 < r < r_p$
$$z(r) = \frac{1}{4}a_1 r^2 + c_1 \tag{E.5}$$

$$\frac{\partial z}{\partial r} = \frac{1}{2}a_1 r \tag{E.6}$$

For $r_p < r < r_a$
$$z(r) = \frac{1}{4}a_2 r^2 + b_2 \ln r + c_2 \tag{E.7}$$

$$\frac{\partial z}{\partial r} = \frac{1}{2}a_2 r + \frac{b_2}{r} \tag{E.8}$$

For $r_a < r < r_f$
$$z(r) = b_3 \ln r + c_3 \tag{E.9}$$

$$\frac{\partial z}{\partial r} = \frac{b_3}{r} \tag{E.10}$$

At the edge of the membrane, $z(r_f) = 0$

$$z(r_f) = b_3 \ln r_f + c_3 = 0 \tag{E.11}$$

$$c_3 = -b_3 \ln r_f \tag{E.12}$$

At the interface $r = r_p$, using (E.6) and (E.8)

$$\frac{\partial z}{\partial r}\Big|_{z=r_p} = \frac{1}{2}a_1 r_p = \frac{1}{2}a_2 r_p + \frac{b_2}{r_p} \tag{E.13}$$

$$b_2 = \frac{1}{2}(a_1 - a_2)r_p{}^2 \tag{E.14}$$

From the previous equations (E.5) and (E.7), then (E.14)

$$z(r_p) = \frac{1}{4}a_1 r_p{}^2 + c_1 = \frac{1}{4}a_2 r_p{}^2 + b_2 \ln r_p + c_2 \tag{E.15}$$

$$c_2 - c_1 = \frac{1}{4}(a_1 - a_2)r_p{}^2 - \frac{1}{2}(a_1 - a_2)r_p{}^2 \ln r_p \tag{E.16}$$

At the interface $r = r_a$, using (E.8) and (E.10)

$$\frac{\partial z}{\partial r}\Big|_{z=r_a} = \frac{1}{2}a_2 r_a + \frac{b_2}{r_a} = \frac{b_3}{r_a} \tag{E.17}$$

$$b_3 = \frac{1}{2}a_2 r_a{}^2 + \frac{1}{2}(a_1 - a_2)r_p{}^2 \tag{E.18}$$

And, from equations (E.7) and (E.9) and (E.12)

$$z(r_a) = \frac{1}{4}a_2 r_a{}^2 + b_2 \ln r_a + c_2 = b_3 \ln\left(\frac{r_a}{r_f}\right) \tag{E.19}$$

$\vdots$

$$\left[\frac{1}{2}a_2 r_a + \frac{1}{2}(a_1 - a_2)r_p{}^2\right]\ln(\frac{r_a}{r_f}) = \frac{1}{4}a_2 r_a{}^2 + \frac{1}{2}(a_1 - a_2)r_p{}^2 \ln r_a + c_2 \tag{E.20}$$

$$c_2 = -\frac{1}{4}a_2 r_a{}^2[1 - 2\ln(\frac{r_a}{r_f})] - \frac{1}{2}(a_1 - a_2)r_p{}^2 \ln r_f \tag{E.21}$$

Then, from (E.16) and (E.21)

$$c_1 = c_2 - \frac{1}{4}(a_1 - a_2)r_p{}^2[1 - 2\ln r_p] \tag{E.22}$$

$$c_1 = -\frac{1}{4}a_2 r_a{}^2[1 - 2\ln(\frac{r_a}{r_f})] - \frac{1}{4}(a_1 - a_2)r_p{}^2[1 - 2\ln(\frac{r_p}{r_f})] \tag{E.23}$$

Substituting for all b, c values gives the following results.

$$z(r) = \begin{cases} \frac{1}{4}a_1 r^2 - \frac{1}{4}a_2 r_a{}^2[1 - 2\ln(\frac{r_a}{r_f})] - \frac{1}{4}(a_1 - a_2)r_p{}^2[1 - 2\ln(\frac{r_p}{r_f})] & r < r_p \\[2mm] \frac{1}{4}a_2 r^2 + \frac{1}{2}(a_1 - a_2)r_p{}^2 \ln(\frac{r}{r_f}) - \frac{1}{4}a_2 r_a{}^2[1 - 2\ln(\frac{r_a}{r_f})] & r_p < r < r_a \\[2mm] \left[\frac{1}{2}(a_1 - a_2)r_p{}^2 + \frac{1}{2}a_2 r_a{}^2\right]\ln(\frac{r}{r_f}) & r_a < r < r_f \end{cases} \tag{E.24}$$

Consider an asymmetrically biased membrane ($V_B = 0$), with signal voltage $V = V_0 + \Delta V$ on the central actuator, and bias voltage V_0 applied to the rest of the actuated area. The value for a in the two zones is given by

$$a_1 = \frac{\epsilon_0}{T\ell_0{}^2}V^2 \tag{E.25}$$

$$a_2 = \frac{\epsilon_0}{T\ell_0{}^2}V_0{}^2 \tag{E.26}$$

Equation (E.24) then becomes

$$z(r) = \begin{cases} \frac{\epsilon_0}{4T\ell_0{}^2}\left\{V^2 r^2 - V_0{}^2 r_a{}^2[1 - 2\ln(\frac{r_a}{r_f})] - (V^2 - V_0{}^2)r_p{}^2[1 - 2\ln(\frac{r_p}{r_f})]\right\} \\[2mm] \frac{\epsilon_0}{4T\ell_0{}^2}\left\{V_0{}^2 r^2 + 2(V^2 - V_0{}^2)r_p{}^2 \ln(\frac{r}{r_f}) - V_0{}^2 r_a{}^2[1 - 2\ln(\frac{r_a}{r_f})]\right\} \\[2mm] \frac{\epsilon_0}{2T\ell_0{}^2}\left\{(V^2 - V_0{}^2)r_p{}^2 + V_0{}^2 r_a{}^2\right\}\ln(\frac{r}{r_f}) \end{cases} \tag{E.27}$$

To determine the static shape of the membrane, let $V = V_0$ in (E.27) then

$$z_s(r) = \begin{cases} \frac{\epsilon_0 V_0{}^2}{4T\ell_0{}^2} \cdot \left\{r^2 - r_a{}^2[1 - 2\ln(\frac{r_a}{r_f})]\right\} & 0 < r < r_a \\[2mm] \frac{\epsilon_0 V_0{}^2}{2T\ell_0{}^2}r_a{}^2 \ln(\frac{r}{r_f}) & r_a < r < r_f \end{cases} \tag{E.28}$$

Setting $r = 0$ in (E.28), the magnitude of the peak static deflection is given by

$$z_s = \frac{\epsilon_0 V_0{}^2}{4T\ell_0{}^2} r_a{}^2 [1 - 2\ln(\frac{r_a}{r_f})] \tag{E.29}$$

The magnitude of the deflection of the centre of the membrane is determined by setting $r = 0$ in (E.27)

$$z_p = \frac{\epsilon_0}{4T\ell_0{}^2} \left\{ (V^2 - V_0{}^2) r_p{}^2 [1 - 2\ln(\frac{r_p}{r_f})] + V_0{}^2 r_a{}^2 [1 - 2\ln(\frac{r_a}{r_f})] \right\} \tag{E.30}$$

and, for signal voltage $V = V_0 + \Delta V$,

$$z_p = \frac{\epsilon_0}{4T\ell_0{}^2} \left\{ 2V_0 \Delta V r_p{}^2 [1 - 2\ln(\frac{r_p}{r_f})] + V_0{}^2 r_a{}^2 [1 - 2\ln(\frac{r_a}{r_f})] \right\} \tag{E.31}$$

Subtracting off the static shape of the mirror gives the dimple deflection due to the signal voltage

$$\Delta z_p = \frac{\epsilon_0}{4T\ell_0{}^2} \left\{ 2V_0 \Delta V r_p{}^2 [1 - 2\ln(\frac{r_p}{r_f})] \right\} \tag{E.32}$$

or

$$\frac{\Delta z_p}{\Delta V} = \frac{\epsilon_0 V_0}{2T\ell_0{}^2} r_p{}^2 [1 - 2\ln(\frac{r_p}{r_f})] \tag{E.33}$$

which describes the deflection sensitivity for the central actuator.

Appendix F

Spherical aberration generation

A controlled amount of spherical aberration may be generated with a simple optical setup involving an on-axis pinhole and an optical element such as a telescope objective lens or parabolic mirror designed to focus parallel light to an aberration-free point.
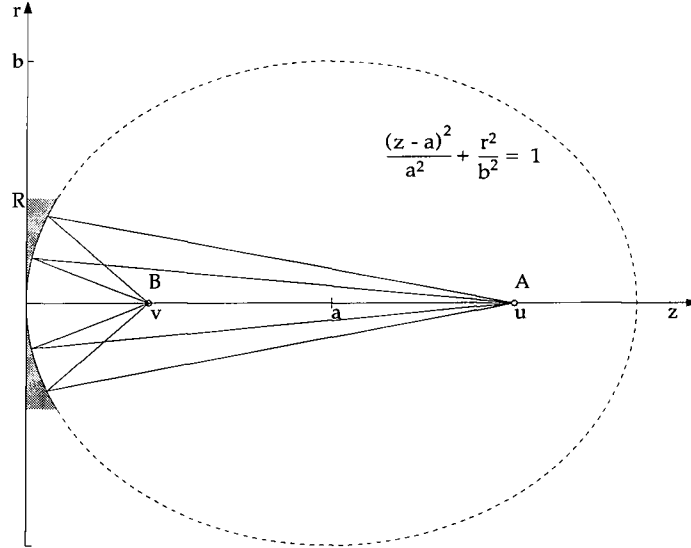

Figure F.1: On-axis elliptical optical arrangement. An elliptical element images an on-axis pinhole A located at $z = u$ to image B located at $z = v$.

Consider a reflecting optical element which images a uniformly illuminated pinhole source located on-axis, as shown in Figure F.1. For a perfectly formed image, the element would have an elliptical shape described by

$$\frac{(z-a)^2}{a^2} + \frac{r^2}{b^2} = 1 \tag{F.1}$$

$$z = a \pm a \cdot \left[1 - \frac{r^2}{b^2}\right]^{\frac{1}{2}} \tag{F.2}$$

with the pinhole and image at the two foci [46].

Selecting the negative solution and applying the binomial theorem yields

$$z = a \cdot \left[\frac{r^2}{2b^2} + \frac{r^4}{8b^4} + \cdots\right] \tag{F.3}$$

If the reflector is parabolic rather than elliptic, then the first term describes the parabola $[z = r^2/4F]$ with focal length $F = b^2/2a$, while the second term specifies a Δz that corresponds to an optical path length increase. This shows up as primary spherical aberration

$$SA = 2\Delta z = \frac{ar^4}{4b^4} = \frac{r^4}{16aF^2} \tag{F.4}$$

Combining the geometric relation $2a = u + v$ with the Gaussian formula $1/u + 1/v = 1/F$ leads to

$$SA = \frac{(u - F)R^4}{8u^2F^2}(\frac{r}{R})^4 \tag{F.5}$$

where the peak spherical aberration A_s is given by

$$A_s = \frac{(u - F)R^4}{8u^2F^2} \tag{F.6}$$

Alternatively, a dimensionless ϵ can be defined as $v = (1 + \epsilon)F$ so that $u = v/\epsilon$ and

$$A_s = \frac{\epsilon R^4}{8(1 + \epsilon)^2 F^3} \tag{F.7}$$

One application of the spherical aberration test pattern produced involves the testing or calibration of wavefront sensors for adaptive optics. In this instance, the curvature wavefront sensor which is described by

$$\frac{\Delta I}{I_0}(r) = \frac{s}{\beta}\left[P \cdot \nabla^2 z(r) - \delta(r - R) \cdot \frac{\partial}{\partial r}z(r)\right] \tag{F.8}$$

where the wavefront curvature $\nabla^2 z(r)$ within the pupil P is derived from an out-of-focus intensity distribution $I(r) = \Delta I + I_0$. The parameters are the distance $s = v \pm \ell$ of the detector from the optical element, the defocus distance ℓ, and a demagnification factor $\beta = \ell/v$.

For the spherical aberration test pattern where $z = A_s(r/R)^4$,

$$\nabla^2 z = \frac{1}{r}\frac{\partial}{\partial r} r \frac{\partial}{\partial r} [A_s(\frac{r}{R})^4] = \frac{16A_s}{R^2} \cdot (\frac{r}{R})^2 \tag{F.9}$$

and the response of the curvature sensor within the aperture will be given by

$$\frac{\Delta I}{I_0} = \frac{16A_s s}{R^2 \beta} \cdot (\frac{r}{R})^2 \tag{F.10}$$

provided the $\delta(r - R)$ edge term is neglected. In this arrangement, $\beta = d/D$ is also the ratio of the image size on the CCD to the pupil size.

Appendix G

Z-transform of the adaptive optics system

The transfer function $G(z)$ of a system with two cascaded zero-order hold functions and a time delay is given by the expression

$$G(z) = (1 - z^{-1})^2 \mathcal{Z} \left[\frac{e^{-T_D s}}{s^2(s + a)} \right] \tag{G.1}$$

where T_D is the dead time. We will extend the Laplace transform pair $F(s)$ and $f(t)$

$$F(s) = \frac{1}{s^2(s + a)} \tag{G.2}$$

$$f(t) = \frac{1}{a^2} \left[e^{-at} + at - 1 \right] \tag{G.3}$$

to include the delay so that $e^{-T_D s} F(s)$ has the transform

$$f(t - T_D)u(t - T_D) = \frac{1}{a^2} \left[e^{-a(t-T_D)} + a(t - T_D) - 1 \right] u(t - T_D) \tag{G.4}$$

where $u(t)$ is the step function.

Directly taking the z-transform in Equation G.1 gives the expression

$$G(z) = (1 - z^{-1})^2 \sum_{k=0}^{\infty} \frac{1}{a^2} \left[e^{-a(kT-T_D)} + a(kT - T_D) - 1 \right] u(kT - T_D) z^{-k} \tag{G.5}$$

and working through stages of mathematical manipulation

$$G(z) = \frac{(1 - z^{-1})^2}{a^2} \left\{ [e^{-a(T-T_D)} + a(T - T_D) - 1]z^{-1} \right. \tag{G.6}$$

$$+ \ [e^{-a(2T-T_D)} + a(2T - T_D) - 1]z^{-2}$$

$$+ \ [e^{-a(3T-T_D)} + a(3T - T_D) - 1]z^{-3} + \ldots \right\}$$

$$G(z) = \frac{(1-z^{-1})^2}{a^2} \left\{ [e^{-a(T-T_D)}z^{-1} + e^{-a(2T-T_D)}z^{-2} + e^{-a(3T-T_D)}z^{-3} + \ldots] \right. \quad (G.7)$$

$$+ \quad aT[z^{-1} + 2z^{-2} + 3z^{-3} + \ldots] - aT_D[z^{-1} + z^{-2} + z^{-3} + \ldots]$$

$$- \quad [z^{-1} + z^{-2} + z^{-3} + \ldots] \Big\}$$

$$G(z) = \frac{(1-z^{-1})^2}{a^2} \left[e^{-a(T-T_D)}z^{-1} \sum_{k=0}^{\infty} e^{-akT}z^{-k} \right. \qquad (G.8)$$

$$+ \quad aT \sum_{k=0}^{\infty} kz^{-k} - (1+aT_D)z^{-1} \sum_{k=0}^{\infty} z^{-k} \right]$$

$$G(z) = \frac{(1-z^{-1})^2}{a^2} \left[\frac{e^{-a(T-T_D)}z^{-1}}{1 - e^{-aT}z^{-1}} + \frac{aTz^{-1}}{(1-z^{-1})^2} - \frac{(1+aT_D)z^{-1}}{(1-z^{-1})} \right] \qquad (G.9)$$

$$G(z) = \frac{(1-z^{-1})^2}{a^2} \left[\frac{e^{-a(T-T_D)}}{z - e^{-aT}} + \frac{aTz}{(z-1)^2} - \frac{(1+aT_D)}{(z-1)} \right] \qquad (G.10)$$

$$G(z) = \frac{(1-z^{-1})^2}{a^2} \left[\frac{aTz}{(z-1)^2} \right. \qquad (G.11)$$

$$- \quad \frac{z[(1+aT_D) - e^{-a(T-T_D)}] - [(1+aT_D)e^{-aT} - e^{-a(T-T_D)}]}{(z-1)(z-e^{-aT})} \right]$$

we finally arrive at the expression for $G(z)$

$$G(z) = \frac{z^2[e^{-a(T-T_D)} + a(T-T_D) - 1]}{a^2z^2(z-e^{-aT})} + \frac{e^{-a(T-T_D)} - (1+aT_D)e^{-aT}}{a^2z^2(z-e^{-aT})} \qquad (G.12)$$

$$+ \quad \frac{z[(1+aT_D) - e^{-aT}[a(T-T_D) - 1] - 2e^{-a(T-T_D)}]}{a^2z^2(z-e^{-aT})}$$

Equation G.12 simplifies for the two limiting cases. For $T_D = 0$, it becomes

$$G(z) = \frac{z[e^{-aT} + aT - 1] - (1+aT)e^{-aT} + 1}{a^2z(z-e^{-aT})} \qquad (G.13)$$

and for $T_D = T$, it simplifies to

$$G(z) = \frac{z[e^{-aT} + aT - 1] - (1+aT)e^{-aT} + 1}{a^2z^2(z-e^{-aT})} \qquad (G.14)$$